

# FLORIDA STATE UNIVERSITY

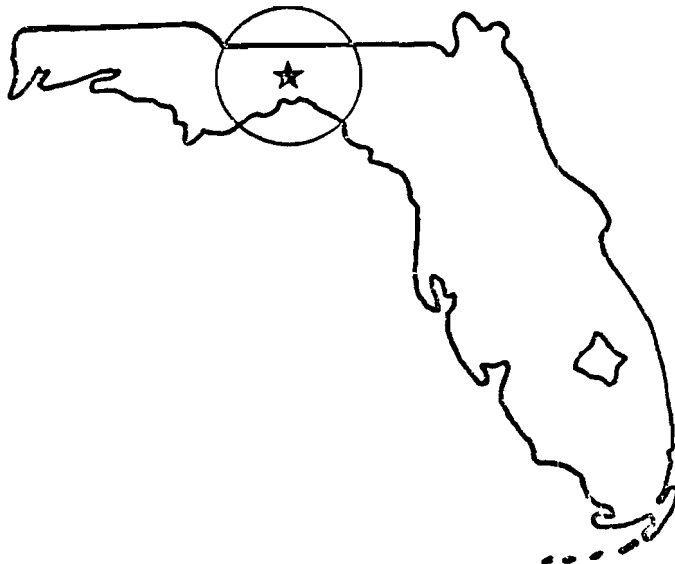
HIGH ENERGY PHYSICS LABORATORY Tallahassee, Florida 32306

OBSERVATION OF DOUBLE PHI MESON PRODUCTION  
IN 400 GEV/C PROTON-NUCLEON INTERACTIONS

by

TOM FOREST DAVENPORT III

December 1984



LIBOFFCE  
FERMILAB  
THESIS

THE FLORIDA STATE UNIVERSITY  
COLLEGE OF ARTS AND SCIENCES

OBSERVATION OF DOUBLE PHI MESON PRODUCTION  
IN 400 GEV/C PROTON-NUCLEON INTERACTIONS

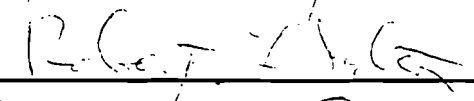
by

TOM FOREST DAVENPORT III


A Dissertation submitted to the  
Department of Physics  
in partial fulfillment of the  
requirements for the degree of  
Doctor of Philosophy

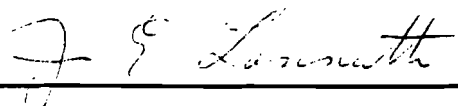
Approved:

  
\_\_\_\_\_  
Professor Directing Dissertation

  
\_\_\_\_\_  
Robert L. Gluck

  
\_\_\_\_\_  
J. D. Kinnel

  
\_\_\_\_\_  
W. N. Shelton

  
\_\_\_\_\_  
J. E. Lammuth

December, 1984

HA01797

FERMILAB  
LIBRARY

OBSERVATION OF DOUBLE  $\Phi$  MESON PRODUCTION  
IN 400 GEV/C PROTON-NUCLEON INTERACTIONS

(Publication No. \_\_\_\_\_)

Tom Forest Davenport III, Ph.D.  
The Florida State University, 1984

Major Professor: John R. Albright, Ph.D.

The production of pairs of  $\phi$  mesons has been observed in 400 GeV/c proton-nucleon interactions at the Fermilab Multiparticle Spectrometer in the inclusive reaction  $p N \rightarrow \phi\phi + X$ , where each  $\phi$  decays to a  $K^+K^-$  pair.

A fast (200ns), high-level trigger processor was used on-line to selectively trigger on events containing two pairs of oppositely charged kaons having low invariant masses. The experimental apparatus and trigger processor are described.

From a sample of 120,000 reconstructed events having at least 2  $K^+$  and 2  $K^-$  tracks in the momentum range  $5.8 < p < 23.0$  GeV/c, the  $K^+K^-K^+K^-$ ,  $\phi K^+K^-$  and  $\phi\phi$  invariant mass spectra are presented. A total of 1503 events are identified as being consistent with  $\phi\phi$  production.

After background subtraction and acceptance

corrections, the total cross sections per nucleon for  $\phi\phi$   
 and  $\phi K+K^-$  production at 400 GeV/c are found to be  
 $\sigma_T(pN \rightarrow \phi\phi + X) = 0.87 \pm 0.27 \mu b$  and  $\sigma_T(pN \rightarrow \phi K + K^- + X) =$   
 $23.6 \pm 2.7 \mu b$ . An upper limit on the cross section  
 times branching ratio for  $\eta_c$  production at 400 GeV/c is  
 established to be  $\sigma_T(pN \rightarrow \eta_c + X) \cdot BR(\eta_c \rightarrow \phi\phi) \leq 30 \text{ nb}$ .

## ACKNOWLEDGMENTS

Experimental high-energy physics today is a collaborative effort and E623 is no exception. This dissertation could not have been written if it were not for the fact that many people worked together to make E623 a success. Among those people, I would especially like to thank Dr. Dan Green and Dr. Howard Fenker of Fermilab for their incomparable contributions to E623 and for the encouragement and support they gave me while I was working on it.

I would also like to thank Sten Hansen and Rich Cantal from the the Fermilab MPS group who struggled to keep the MPS running and also struggled to teach me something about electronics and detectors.

I would like to thank Dr. J. H. Goldman for all his work on E623 and for all the suggestions and assistance he gave me during the processing and analysis of the data. In addition, I would like to thank all the other E623 collaborators from University of Arizona, Fermilab, Florida State University, Notre Dame University, Tufts University, Vanderbilt University and Virginia Polytechnic Institute.

Finally, I would like to express my gratitude to Dr. John R. Albright for serving as my thesis advisor at Florida State and for always being willing to help me answer my many questions about high-energy physics and I would like to thank Dr. J. Lannutti, Dr. D. Kimel, Dr. N. Shelton and Dr. R. Fulton for serving on my committee.

## TABLE OF CONTENTS

ABSTRACT .....	ii
ACKNOWLEDGEMENTS .....	iv
LIST OF FIGURES .....	vii
LIST OF TABLES .....	x
CHAPTER I : INTRODUCTION .....	1
CHAPTER II : THEORETICAL PRELIMINARIES .....	3
CHAPTER III: EXPERIMENTAL DETAILS .....	21
CHAPTER IV : DATA PROCESSING .....	49
CHAPTER V : DATA PRESENTATION AND DISCUSSION ....	63
CHAPTER VI : SUMMARY AND CONCLUSIONS .....	102
APPENDIX : CERENKOV RADIATION .....	107
REFERENCES .....	112



## LIST OF FIGURES

Figure	Page
II.1 - Quantum numbers of u, d and s quarks.	4
II.2 - Pseudoscalar and vector meson nonets.	6
II.3 - a) OZI forbidden decay. b) OZI allowed decay.	10
II.4 - a) OZI allowed decay of $\phi$ into $K+K^-$ . b) OZI forbidden decay of $\phi$ into $\rho\pi$ .	10
II.5 - QCD interpretation of OZI forbidden decay via gluons and example of $J/\psi$ decay.	10
II.6 - Energy level diagram for charmonium states.	12
II.7 - Schematic diagram of $\eta_c$ production in hadronic interactions by two gluon fusion	15
II.8 - Total inclusive cross section for $\eta_c$ production in proton-proton interactions using the model of Einhorn and Ellis. The curves represent different gluon distribution functions in the protons.	16
II.9 - Allowed values of $J^{PC}$ for $q\bar{q}$ mesons.	18
II.10 - Allowed values of $J^{PC}$ for $\phi\phi$ system.	20
III.1 - Layout of the FNAL MPS for E623.	23
III.2 - Diagram of typical MWPC for E623.	25
III.3 - Diagram of typical drift chamber for E623.	25
III.4 - Map of $C_A$ mirrors, looking downstream.	32
III.5 - Map of $C_B$ mirrors, looking downstream.	33
III.6 - Map of SC scintillator segments, looking downstream.	34

III.7 - Layout of MPS showing trigger chamber locations. Tic marks indicate active areas for triggering purposes.	38
III.8 - Schematic diagram of Fast-Or MWPC chamber preamplifier.	39
III.9 - Schematic diagram of drift chamber amplifier/discriminator designed for E623.	40
III.10 - Schematic diagram of window discriminator designed for E623.	41
III.11 - E623 trigger logic diagram.	43
IV.1 - Orientation of coordinate system used in E623.	51
IV.2 - Expected number of photoelectrons for a pion in counter $C_B$ versus momentum.	56
IV.3 - Typical spectrum for a $C_B$ ADC channel.	58
V.1 - $K+K^-$ invariant mass spectrum from E623.	64
V.2 - $K+K^-$ invariant mass, cut on other $\phi$ ( $\pm 6$ MeV wide).	66
V.3 - $K+K-K+K^-$ invariant mass spectrum.	67
V.4 - $\phi K+K^-$ invariant mass spectrum.	68
V.5 - $\phi\phi$ invariant mass spectrum.	70
V.6 - a) Scatter plot of $M(K+K^-)_1$ versus $M(K+K^-)_2$ b) After $K+K-K+K^-$ background subtraction c) After $\phi K+K^-$ background subtraction.	72
V.7 - $\phi\phi$ background spectrum.	73
V.8 - $\phi\phi$ invariant mass spectrum with background superimposed (cross hatched area).	74
V.9 - Feynman $x$ ( $x_F$ ) distribution for all $K+K-K+K^-$ combinations.	78
V.10 - Monte Carlo generated acceptance versus $x_F$ for $M(\phi\phi) = M(\eta_c)$ .	80

V.11 - Monte Carlo generated acceptance versus $\phi\phi$ invariant mass for $x_F = -.1, 0., .1$ .	81
V.12 - E623 estimated mass resolution versus $K+K-K+K-$ invariant mass.	83
V.13 - $\phi\phi$ invariant mass spectrum and acceptance for 100 GeV/c data [Dau 81].	90
V.14 - $\phi\phi$ invariant mass spectrum, background subtracted spectrum and acceptance for 175 GeV/c data [Dau 81].	91
V.15 - $\phi\phi$ invariant mass spectrum a) 1981 100 GeV/c data b) 1982 100 GeV/c data [Bai 83].	92
V.16 - a) $\phi\phi$ invariant mass spectrum b) Background subtracted spectrum c) Residuals from fit to background subtracted spectrum [Boo 84].	94
V.17 - $\phi\phi$ invariant mass spectrum corrected for acceptance [Lin 83].	97
V.18 - Partial wave decomposition of $\phi\phi$ spectrum [Lin 83].	97
V.19 - $\phi\phi$ total cross section versus $s$ , using model of Li and Liu. Data points from E623 and ACCMOR are shown.	100
V.20 - Experimental upper limits for $\eta_c$ cross section and theoretical predictions using model of Einhorn and Ellis with gluon distribution functions of Duke and Owens.	101
A.1 - Huygens construction of angle of Cerenkov radiation $\theta_c$ .	108
A.2 - Construction for determining distribution of photons in Cerenkov cone.	108
A.3 - Construction for determining the weight of a strip of width, $a$ , in a Cerenkov cone.	108

## LIST OF TABLES

Table	Page
III.1 : E623 Wire Chambers .....	24
III.2 : Cerenkov Counter Parameters for E623 .....	31
IV.1 : $C_B$ ADC Values for Particle Identification Algorithm .....	59
IV.2 : Particle ID Types from $C_B$ Analysis .....	62
V.1 : Beam and Target Information .....	76
V.2 : Numbers Used for Acceptance and Cross Section Calculation .....	87
V.3 : Summary of Cross Sections and Upper Limits for Inclusive $\phi\phi$ Production .....	95
V.4 : BNL/CCNY $g_T$ States (from [Hit 84]) .....	98

## Chapter I

### INTRODUCTION

In this dissertation, results are presented from Fermilab Experiment 623, a study of double  $\phi$  meson production in proton-nucleon interactions. The reaction studied was

$$\begin{array}{l} p N \rightarrow \phi\phi + X \\ \quad \quad \quad \swarrow \quad \searrow \\ \quad \quad \quad K+K- \\ \quad \quad \quad K+K- \end{array}$$

at an incident beam momentum of 400 GeV/c.

The purpose of the experiment was to look for new states decaying into a pair of  $\phi$  mesons. In particular, it was designed to look for central production of heavy states containing hidden strangeness, quark model exotics, massive bound states of gluons (glueballs) and the pseudoscalar member of the charmonium family, the  $\eta_c$ . The reasons for performing the experiment and for using the  $\phi\phi$  decay mode will be discussed in more detail in Chapter II.

The data were collected during May and June of 1982 by the E623 collaboration at the Fermilab Multiparticle Spectrometer. The experiment used a very fast (200ns) high-level trigger processor to look for events

containing two pairs of oppositely charged kaons having low invariant masses consistent with the mass of the  $\phi$  meson. Nearly four million triggers were recorded during the experimental run. The spectrometer system and the trigger and trigger processor will be described in Chapter III.

In Chapter IV the off-line processing programs are described including pattern recognition, track fitting and particle identification.

The experimental data from E623 are presented in Chapter V along with results from previous experiments concerning  $\phi\phi$  production. The acceptance calculation is described and cross sections for  $\phi\phi$  and  $\phi K+K^-$  are calculated along with an upper limit for  $\eta_c$  production. The total inclusive cross section for  $\phi\phi$  production at 400 GeV/c is measured to be  $0.87 \pm 0.27 \mu\text{b}$  and for  $\phi K+K^-$  the cross section is  $23.6 \pm 2.7 \mu\text{b}$ . An upper limit of 30 nb is given for  $\eta_c$  production times branching ratio into  $\phi\phi$  at 400 GeV/c. No evidence for production of new resonances is seen.

In Chapter 6, a summary of the results and conclusions from E623 is given along with an analysis of the relative successes and failures of the experiment and suggestions on how the experiment could have been improved.

## Chapter II

### THEORETICAL PRELIMINARIES

Since the time of the early Greeks, humans have sought to understand their world by assuming that all objects are composed of a small number of simpler, elemental ones. First attempts included earth, air, fire and water and the nuclear shell model [May 49].

In 1961 Gell-Mann and Ne'eman [Gel 61] introduced the eight-fold way of  $SU(3)$  as a classification system for the known hadron spectrum. Its success in bringing order to the hadronic "zoo" and the prediction and subsequent discovery of the  $\Omega^-$  particle [Bar 64] was convincing evidence for some underlying pattern in nature.

The quark model, proposed independently by Gell-Mann and Zweig in 1964 ([Gel 64a],[Zwe 64]), conjectured that this pattern was due to the composite nature of the hadrons. In the basic quark model all hadrons are composed of either a quark-antiquark pair (mesons) or three quarks (baryons). The quarks come in three flavors  $u$ (up),  $d$ (down) and  $s$ (strange) and have spin  $1/2$  and baryon number  $1/3$  (Figure II.1). They also carry an

Quantum Numbers of Quarks

	<u>Q</u>	<u>I<sub>3</sub></u>	<u>B</u>	<u>S</u>
u	2/3	+1/2	1/3	0
d	-1/3	-1/2	1/3	0
s	-1/3	0	1/3	-1

Fig. II.1 - Quantum numbers of u, d and s quarks.



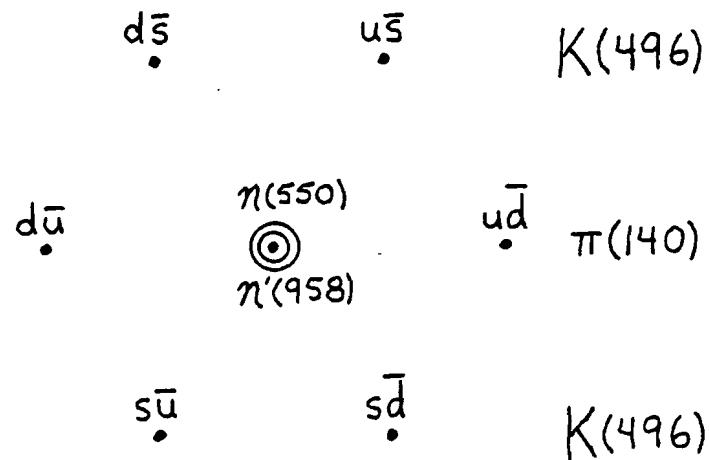
additional quantum number known as color, having three possible values, which is necessary if the quarks are to obey Fermi-Dirac statistics [Gre 64].

In the three quark-antiquark model, mesons are grouped into nonets (a singlet along with an octet) with each member of the nonet having the same spin and parity. The pseudoscalar and vector nonets are shown in Figure II.2. The  $\phi$  meson is an isoscalar member of the vector ( $J^P=1^-$ ) nonet having  $C$  (charge conjugation) = +1 and quark content  $s\bar{s}$ .

Another quark,  $c$ (charm), was proposed by Bjorken and Glashow in 1964 [Bjo 64] and later, in 1970, by Glashow, Iliopoulos and Maiani (GIM)[Gla 70]. The GIM theory used the charmed quark to cancel the predicted but unobserved strangeness-changing weak neutral currents. Their prediction of a new class of heavy charmed particles was brilliantly confirmed in 1974 with the discovery of the  $J/\psi$  ([Aug 74],[Aub 74]), a meson interpreted as a  $c\bar{c}$  bound state. In 1977, evidence for a fifth quark,  $b$ (bottom), was seen at Fermilab [Her 77] and it is now believed that at least six quark flavors exist but the sixth quark,  $t$ (top), has yet to be observed [Qui 83].

The  $SU(3)$  symmetry of Gell-Mann and Ne'eman is a flavor symmetry corresponding to the three light quark

Pseudoscalar Nonet ( $J^P = 0^-$ )



Vector Nonet ( $J^P = 1^-$ )

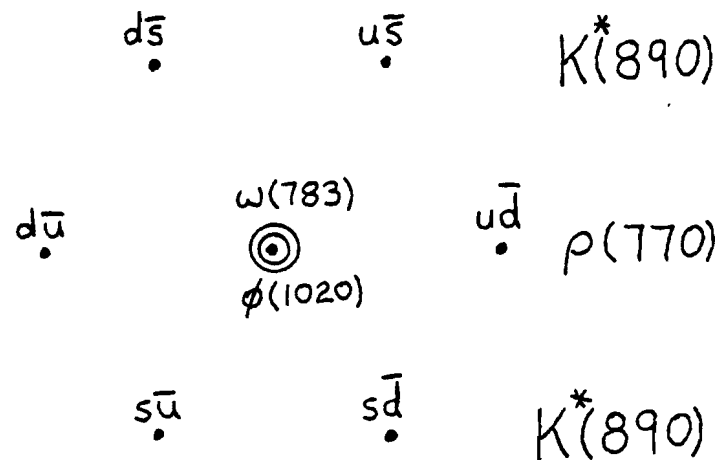


Fig. II.2 - Pseudoscalar and vector meson nonets.

flavors  $u$ ,  $d$ , and  $s$ . This symmetry is not exact however, and it is thought that the symmetry-breaking effects are due to the small mass differences between the quark flavors. These effects are much larger for the  $c$  and  $b$  quarks since  $m_c \approx 1.5$  GeV and  $m_b \approx 5$  GeV, while the light quark masses are on the order of several hundred MeV [Qui 83].

In 1954, Yang and Mills [Yan 54] tried to construct a theory of strong interactions, based on the approximate isospin invariance between protons and neutrons, by requiring that the theory be invariant under local  $SU(2)$  isospin rotations. The theory predicted that the strong force should be due to the exchange of three types of massless vector bosons and hence be of infinite range as in electrodynamics. As the nuclear force was known to be of short range and thought to be due to the exchange of massive bosons, the theory could not be accepted as correct.

The basic idea of Yang and Mills was extended by Nambu [Nam 66] and Fritzsch, Gell-Mann and Leutwyler [Fri 73] to the gauge group  $SU(3)$ . This was not the old  $SU(3)$  flavor symmetry but a dynamical theory based on an exact color symmetry. This local gauge field theory of strong interactions between quarks has become known as quantum chromodynamics (QCD).

In QCD a color octet of massless gluons is responsible for mediating the interactions between colored quarks. Since the gluons themselves carry a color charge, they can couple to other gluons as well as to quarks. Because of this property some have speculated that massive color-singlet bound states consisting only of gluons could exist in addition to the mesons and baryons. These states are called glueballs or gluonia.

### Glueballs

Color singlet glueballs can be formed from either two or three gluons, although the idea of counting gluons is not exact since gluons couple to other gluons and can emit and reabsorb each other. However, the idea of two or three gluons as a glueball is useful in practice for the predictions of masses and quantum numbers. Though the exact masses of glueball states cannot be predicted theoretically, the basic level orderings and approximate masses are predicted by several models and are in rough agreement [Sha 84].

The  $J^{PC}$  for the lowest lying two-gluon glueball state is expected to be  $0^{++}$  and the mass is predicted to be around 800 MeV with a large width, making this state rather difficult to see experimentally since it is expected to mix with nearby  $q\bar{q}$  states [Rob 77]. For the

lowest three-gluon glueball the  $J^{PC}$  is  $0^{-+}$  with a mass in the range 1.0-1.5 GeV. Masses for glueballs with other  $J^{PC}$  are expected to be in the range 1.2-3.0 GeV.

Typical widths for glueball states are conventionally expected to be between typical hadronic widths ( $\approx 100$  MeV) and widths for OZI violating decays ( $\approx 1$  MeV). The OZI rule will be described below. Glueball widths would then be expected to be between 10 and 50 MeV [Rob 77]. Other authors have claimed however, that glueball widths could be anywhere in the range 1-200 MeV [Hit 83]. Thus the width of a new state is not expected to be a very reliable indication of whether it is a glueball.

The OZI (Okubo, Zweig, Iizuka) rule ([Oku 63], [Zwe 64], [Iiz 66]) states that amplitudes for decays corresponding to disconnected quark-line diagrams, like Figure II.3a, are suppressed relative to those for connected ones like Figure II.3b. This rule was invented primarily to explain why the decay mode of the  $\phi$  into  $\rho\pi$  is suppressed relative to that into  $K\bar{K}$ . If the  $\phi$  is entirely  $s\bar{s}$  then the decay into  $K\bar{K}$  will be allowed by the OZI rule (Figure II.4a) and the decay into  $\rho\pi$  will be suppressed (Figure II.4b) even though it would normally be favored due to phase space considerations. In the language of QCD, the OZI rule

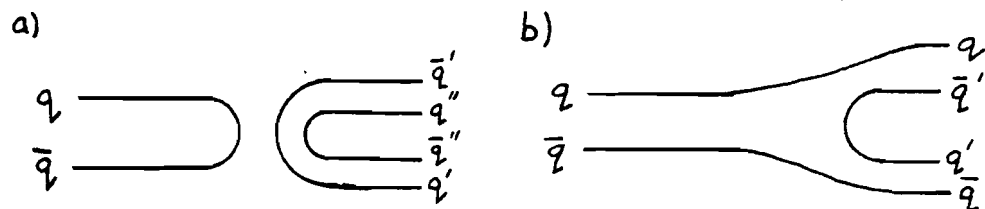


Fig. II.3 - a) OZI forbidden decay. b) OZI allowed decay.

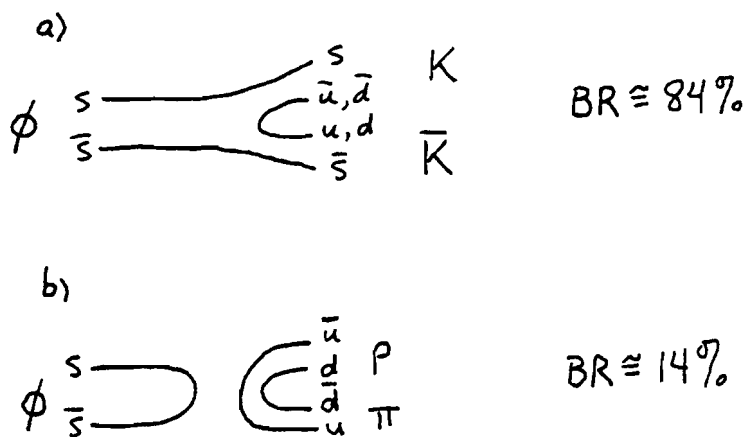


Fig. II.4 - a) OZI allowed decay of  $\phi$  into  $K+K^-$ .  
b) OZI forbidden decay of  $\phi$  into  $\pi\pi$ .

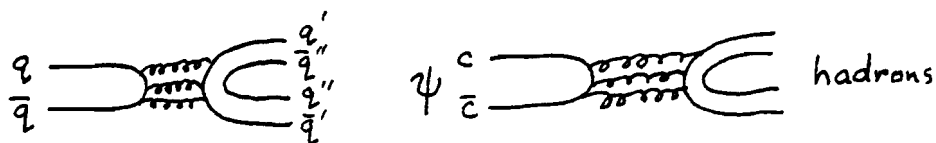


Fig. II.5 - QCD interpretation of OZI forbidden decay via gluons and example of  $J/\psi$  decay.

would be expressed by saying that amplitudes for diagrams requiring exchanges of gluons (Figure II.5) are suppressed relative to those for connected diagrams requiring no gluon exchanges.

The decay modes of glueballs have been predicted to be one possible method of distinguishing them from standard quark model states. Since glueballs are flavorless (no quark content), they should be expected to decay in a flavor symmetric manner [Rob 77], implying that decays into strange particles should be just as likely as those into non-strange particles, up to phase space considerations. This argument is also in dispute and there are reasons to believe that  $s\bar{s}$  states in glueball decay may be more likely than  $u\bar{u}$  or  $d\bar{d}$  [Hit 83]. Hitlin also observes that no state presented as a glueball candidate, thus far, has been observed to decay in a flavor symmetric manner.

#### The $\eta_c$

The  $\eta_c(2980)$  is the lowest lying member of the charmonium family of mesons, i.e.  $c\bar{c}$  bound states (Figure II.6) [Qui 83]. Its quantum numbers are predicted to be  $J^{PC} = 0^{-+}$  and this has been recently confirmed at SPEAR [Bal 84]. Since it is a pseudoscalar it cannot be probed directly in  $e^+e^-$  annihilation, but must be observed, at  $e^+e^-$  machines, by looking at

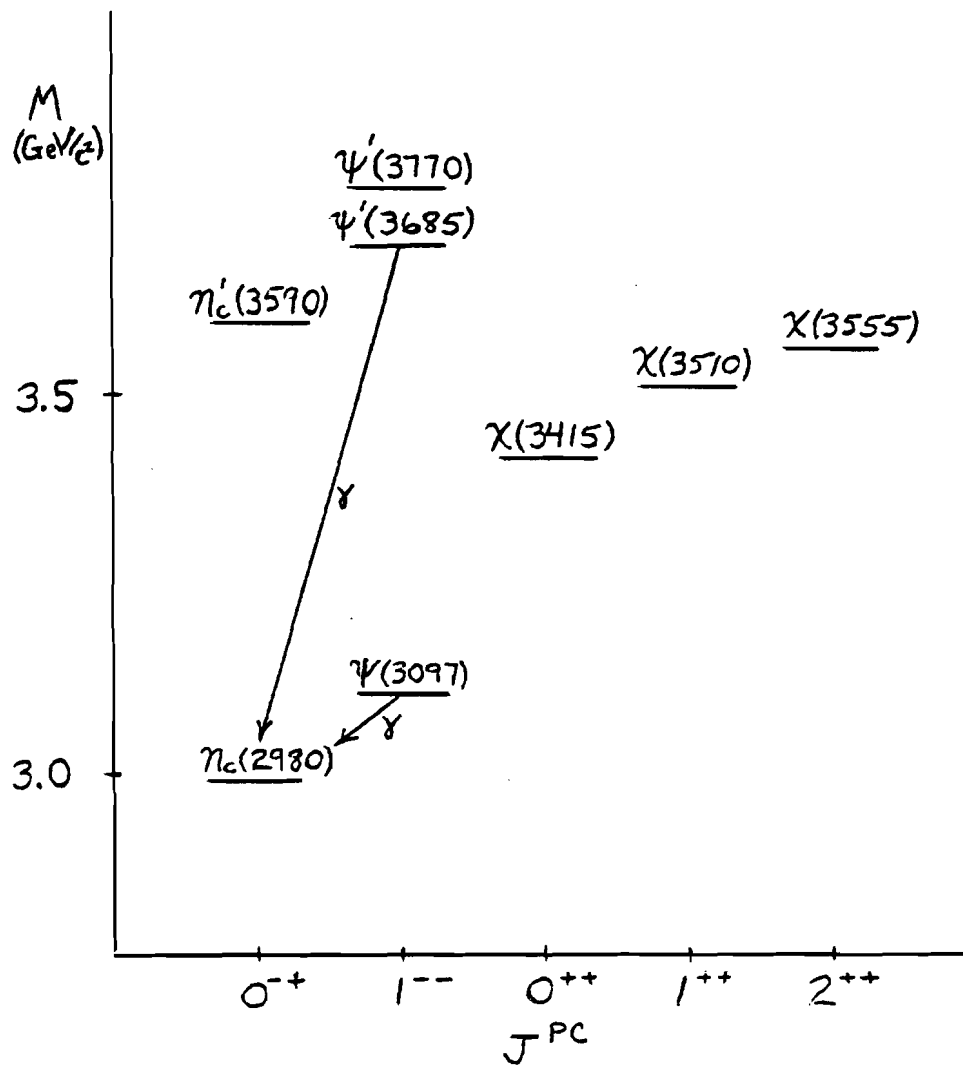


Fig. II.6 - Energy level diagram for charmonium states.



radiative decays of more massive,  $J^{PC} = 1^{--}$ , charmonium states. The  $\eta_c$  has thus far not been observed in hadronic production experiments.

The  $\phi\phi$  decay channel has been suggested as a favorable place to look for the  $\eta_c$  [Lip 77a] and measure its spin and parity. Since the  $\eta_c$  has  $C=+1$ , it can decay to  $\phi\phi$  and the branching ratio into  $\phi\phi$  is relatively large (0.8%)[Bal 84].

The angular distributions for the  $\eta_c$  decay into  $\phi\phi$  are expected to be isotropic in the  $\eta_c$  rest frame. However, one expects to see a  $\sin^2\theta$  distribution for the polar angle of the  $K^+$  with respect to the direction of the  $\phi$  transformed into the  $\phi$  rest frame (helicity frame), and a  $1-\cos(2\gamma)$  distribution for the angle,  $\gamma$ , between the normals to the decay planes formed by the  $K^+K^-$  pairs from the  $\phi$  decays [Cha 78]. This has also been confirmed recently [Bal 84].

There are several estimates of the cross section for  $\eta_c$  production in hadronic reactions. The parameterization of Bourquin and Gaillard [Bou 76] gives the total inclusive cross section for hadron production in nucleon-nucleon interactions as

$$\sigma_{\text{tot}} = A \times 0.45 \times 10^{-20} \times y_{\text{max}}^2 \times e^{-5.13/y_{\text{max}}^{0.38}} \frac{m}{(m+2)^{12.3}}$$

where  $m$  is the mass of the particle produced,  $y_{\max}$  is the maximum rapidity of the particle in the center of momentum system,

$$y_{\max} = \ln[(E_{\max}^* + p_{\max}^*)/m] \approx \ln[\sqrt{s}/m] ,$$

and  $A$  is the suppression factor;  $A \approx 1$  for OZI allowed processes and is less than one for OZI suppressed processes, e.g.  $\Psi$  production where  $A \approx 1/30$ .

For  $\eta_c$  production at 400 GeV/c, this gives a total inclusive cross section

$$\sigma_T(pp \rightarrow \eta_c + X) \approx 0.5 \mu b .$$

It has been suggested [Afe 80b] that  $\eta_c$  production in nucleon-nucleon interactions takes place primarily through two-gluon annihilation (Fig. II.7). The cross section for this process is given by Einhorn and Ellis [Ein 75] as

$$\sigma_T(pp \rightarrow \eta_c + X) = \frac{8\pi^2 \Gamma}{64M^3} \tau \int_{\tau}^1 (1/x) F^A(x) F^B(\tau/x) dx$$

where  $F^A$  and  $F^B$  are the gluon distributions in the hadrons,  $M$  and  $\Gamma$  are the mass and width of the  $\eta_c$ , and  $\tau = M^2/s$ . Figure II.8 shows the cross section as a function of  $s$  for several gluon distributions. The form used for the gluon distribution is

$$F(x) = ((n+1)/2x)(1-x)^n ,$$

where the value of  $n$  depends on the model that is used.

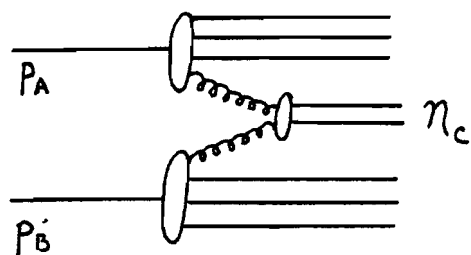


Fig. II.7 - Schematic diagram of  $\eta_c$  production in hadronic interactions by two gluon fusion

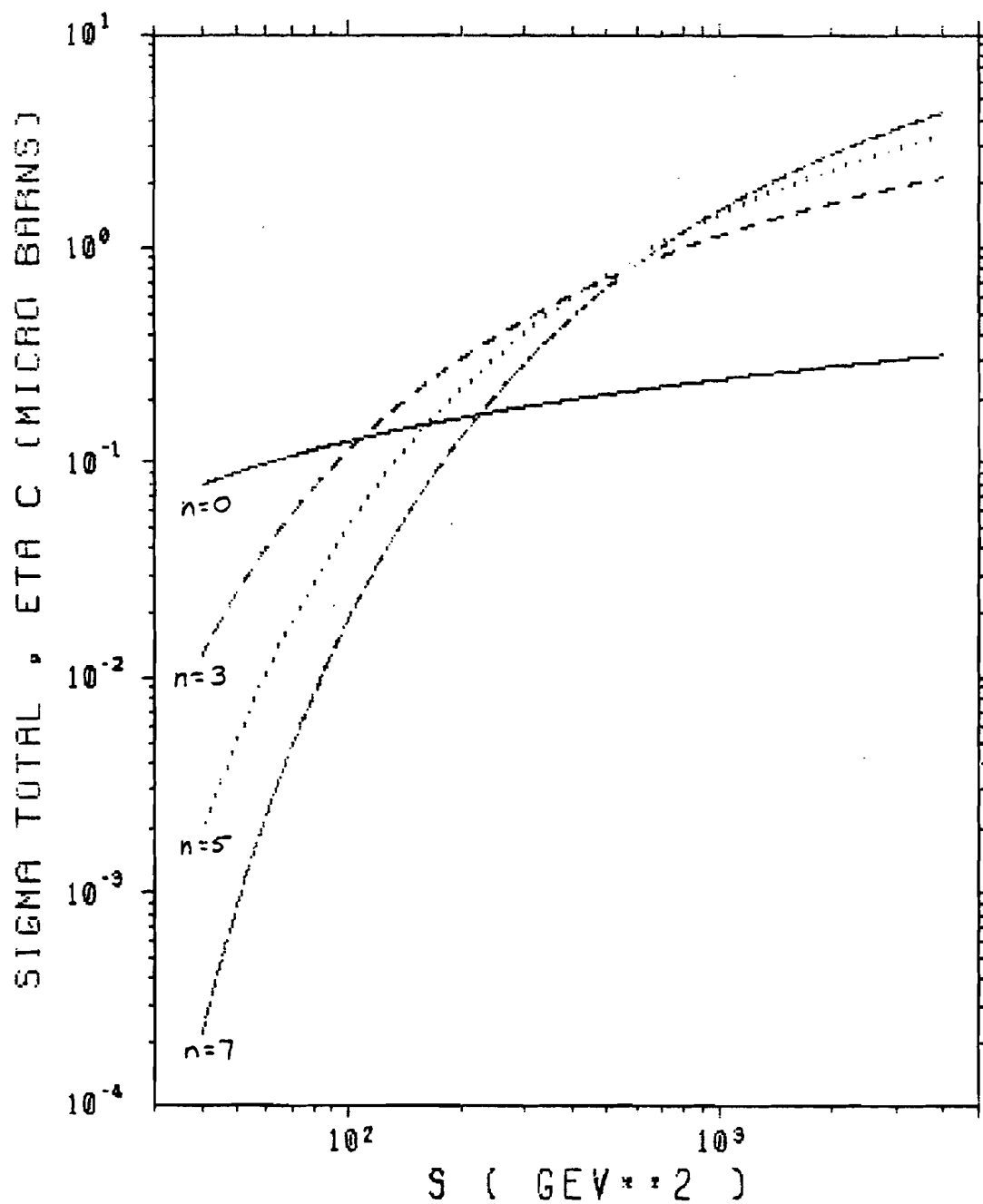


Fig. II.8 - Total inclusive cross section for  $\eta_c$  production in proton-proton interactions using the model of Einhorn and Ellis. The curves represent different gluon distribution functions in the protons.

For nucleons, the values of  $n$  used were 0, 3, 5 and 7 corresponding to the following four cases: 1) a distribution based on equipartition of momentum, 2) a distribution based on the assumption that gluons behave like valence quarks, 3) a distribution based on the Brodsky-Farrar rules [Bro 73], and 4) a distribution resembling that of the  $q\bar{q}$  sea.

Using the above assumptions, the total inclusive  $\eta_c$  cross section at 400 GeV/c is in the range

$$\sigma_T(pp \rightarrow \eta_c + X) \approx 0.2 - 1.0 \mu b.$$

#### Exotics and The $\phi\phi$ System

In the non-relativistic quark model, mesons are  $q\bar{q}$  bound states with orbital angular momentum  $\vec{L}$  and total spin  $\vec{S}$  ( $S=0,1$ ). Since fermions and antifermions have opposite intrinsic parities, the parity of the bound state is  $P=(-1)^{L+1}$ . Under the charge conjugation operator

$$C|q\bar{q}\rangle = |\bar{q}q\rangle = (-1)^{L+S}|q\bar{q}\rangle,$$

giving  $C=(-1)^{L+S}$ . Using this information, the allowed  $J^{PC}$  states for  $q\bar{q}$  systems can be constructed as shown in Figure II.9.

It is seen that states having  $J^{PC} = 0^{--}, 0^{+-}, 1^{-+}, 2^{+-}, 3^{-+}$ , etc. are not allowed. States with these quantum numbers are called quark model exotics. So far, all meson states that have been observed have quantum

# Allowed Quantum Numbers for $q\bar{q}$ Mesons

$$S = 0 \text{ or } 1$$

$$P = (-1)^{L+1}$$

$$C = (-1)^{L+S}$$

$L$	$J^{PC} (S=0)$	$J^{PC} (S=1)$
0	$0^{-+}$	$1^{--}$
1	$1^{+-}$	$0^{++}$ $1^{++}$ $2^{++}$
2	$2^{-+}$	$1^{--}$ $2^{--}$ $3^{--}$

Fig. II.9 - Allowed values of  $J^{PC}$  for  $q\bar{q}$  mesons.

numbers consistent with quark model predictions.

Lipkin [Lip 77b] gives several reasons why the  $\phi\phi$  system might be a good place to look for exotics, as well as glueballs and the  $\eta_c$ . First, since inclusive kaon cross sections in nucleon-nucleon reactions are much lower than pion cross sections, background problems should be less severe. Secondly, the narrow width of the  $\phi$  ( $\Gamma \approx 4$  MeV) and large branching ratio into  $K+K^-$  (50%) should also help reduce background problems. Finally, the low Q-value for  $\phi \rightarrow K+K^-$  (32 MeV) tends to give a small opening angle between the kaons in the laboratory, leading to good geometrical acceptance and the possibility of simple pattern for triggering purposes.

Since the  $\phi$  has  $J^{PC} = 1^{--}$ , a  $\phi\phi$  system will have  $P = (-1)^L$ , where  $L$  is the relative orbital angular momentum, and the allowed values for the total spin,  $S$ , will be 0, 1 or 2. Because the  $\phi\phi$  system must be symmetric under simultaneous interchange of all coordinates (Pauli principle),  $L+S$  must be even and  $C = +1$ . Figure II.10 show the lowest allowed  $J^{PC}$  states for a  $\phi\phi$  system and it is seen that any  $J^{PC}$  combination with  $C = +1$  can be constructed, including some that are exotic.

Quantum Numbers for a  $\phi\phi$  System

$$J^{PC}(\phi) = 1^{--}$$

For a  $\phi\phi$  system

$$S = 0, 1 \text{ or } 2$$

$$P = (-1)^L$$

$$C = (-1)^{L+S} = +1$$

$$L + S = \text{even}$$

<u>L</u>	<u>S</u>	<u><math>J^{PC}</math></u>
0	0	$0^{++}$
	2	$2^{++}$
1	1	$0^{-+} (\eta_c)$
		$1^{-+} (\text{exotic})$
		$2^{-+}$
2	0	$2^{++}$
	2	$0^{++}$
		$1^{++}$
		$2^{++}$
		$3^{++}$
		$4^{++}$
3	1	$2^{-+}$
		$3^{-+} (\text{exotic})$
		$4^{-+}$

Fig. II.10 - Allowed values of  $J^{PC}$  for  $\phi\phi$  system.



## Chapter III

### EXPERIMENTAL DETAILS

The experiment was performed at the Multiparticle Spectrometer(MPS) at the Fermi National Accelerator Laboratory(FNAL) during May and June of 1982.

The MPS is located at the end of the M6West beam line and is approximately 1850 feet downstream of the MWest production target. A beam of 400 GeV/c protons extracted from the main ring at FNAL was directed onto the production target in order to produce beams of secondary particles or, as in our case, to reduce the intensity of the primary beam. Diffracted protons were collimated and transported down the M6W beam line to the MPS. This gave us essentially a pure proton beam at the accelerator energy but with a much lower intensity. The repetition rate of the beam was approximately 13 seconds with each pulse lasting one second. There were about  $2 \times 10^6$  protons on target in each pulse.

#### The MPS

The MPS is a large, open-geometry spectrometer system designed to look at systems of charged particles in the forward direction. For E623 the MPS consisted of

the following: 8 small multiwire proportional chambers(MWPCs) for beam tracking, a segmented scintillator target, 25 planes of MWPCs for tracking of secondary charged particles, a 2'x4'x4' superconducting magnet for momentum analysis, 2 multicell gas Cerenkov counters for particle identification, a scintillator hodoscope, 8 planes of 5.5'x11' drift chambers also used for tracking, and several small scintillator paddles used for triggering. The basic configuration can be seen in Fig. III.1. Table III.1 gives the dimensions and locations of the MWPCs and drift chambers. The use and operation of the above devices will now be described.

The multiwire proportional chamber is one of the most common types of charged particle detectors used in high energy physics today. It basically consists of three planes of wires inside a gas-filled box (Fig. III.2). The two outer planes of wires, the cathode planes, are placed at a large negative voltage. The inner plane of wires is the sense plane or anode plane and is at ground potential. When a charged particle passes through the chamber it ionizes the gas along the path of the particle. The electrons released by the ionization are repelled from the cathode planes and are accelerated towards the nearest sense wire. The

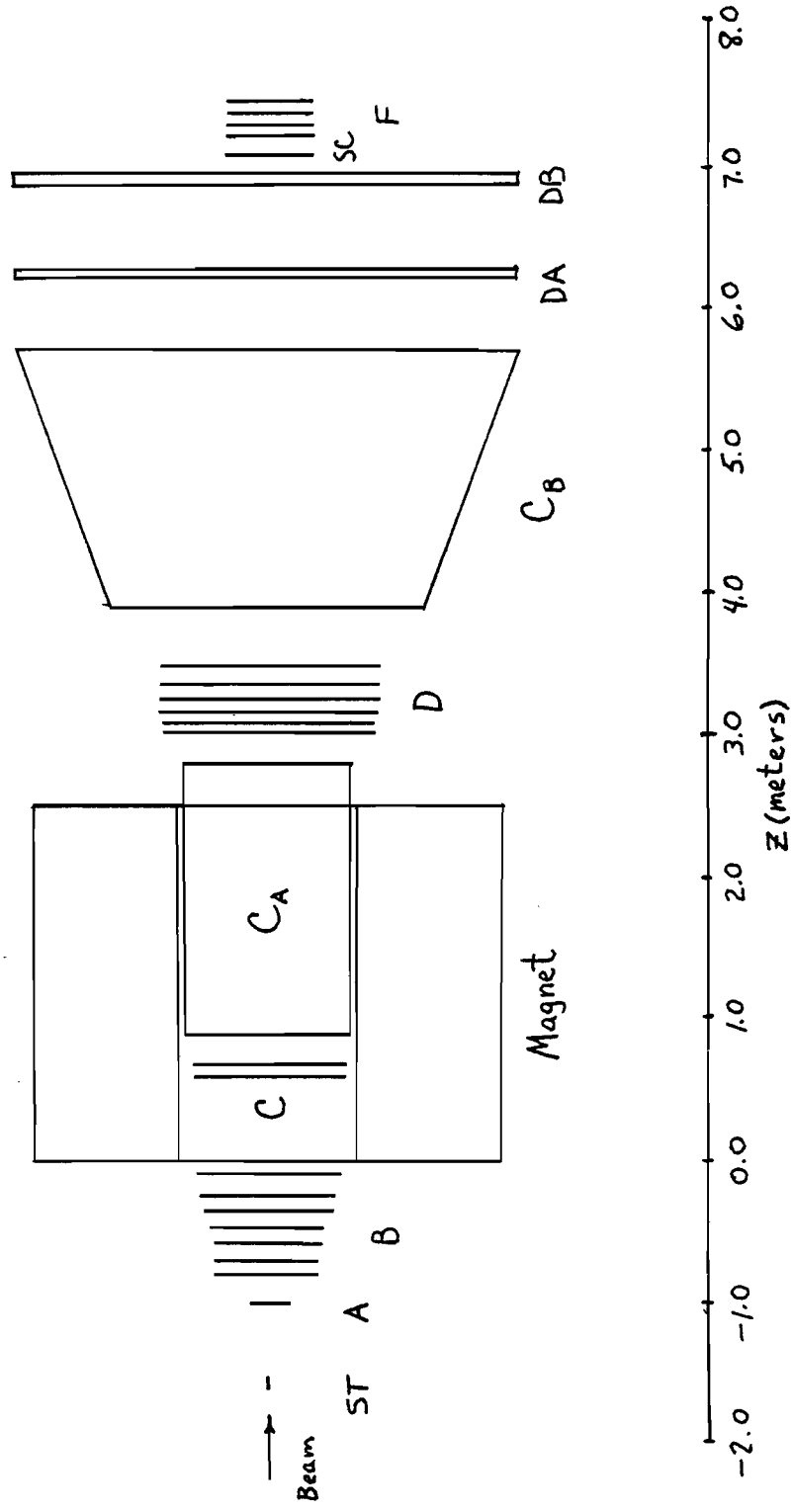


Fig. III.1.1 - Layout of the FNAL MPS for E623.

TABLE III.1  
E623 WIRE CHAMBERS

Name	Spacing	# of Wires	Z-position	Angle
BA1 X	2mm	64	-33.236m	0°
Y	2	64	-33.252	90
BA2 X	2	64	-21.182	0
Y	2	64	-21.197	90
BA3 V	2	64	-21.043	135
BB2 X	2	32	-2.185	0
BB1 X	1	32	-1.880	0
Y	1	32	-1.873	90
A X1	1mm	256	-1.054m	0°
X2	1	256	-1.048	0
Y1	1	256	-1.043	90
Y2	1	256	-1.037	90
U	1	256	-0.968	45
V	1	256	-0.963	135
B X1	2mm	384	-0.813m	0°
Y1	2	192	-0.720	90
X2	2	384	-0.572	0
Y2	2	192	-0.478	90
X3	2	448	-0.362	0
Y3	2	256	-0.283	90
U	2	448	-0.081	27
C X	2mm	512	+0.600m	0°
Y	2	320	0.676	90
D X1	2mm	800	3.001m	0°
Y1	3	320	3.088	90
U	2	864	3.177	15
V	2	864	3.298	165
Y2	3	320	3.386	90
X2	2	800	3.475	0
DA U	.72"	192	6.198m	17°
V	.72	192	6.217	163
X1	.75	176	6.236	0
X2	.75	176	6.255	0
DB U	.72"	192	6.910m	17°
V	.72	192	6.929	163
X1	.75	176	6.948	0
X2	.75	176	6.967	0
F X	2mm	320	7.211m	0°
Y	2	320	7.291	90
U	2	320	7.374	45
V	2	320	7.455	135

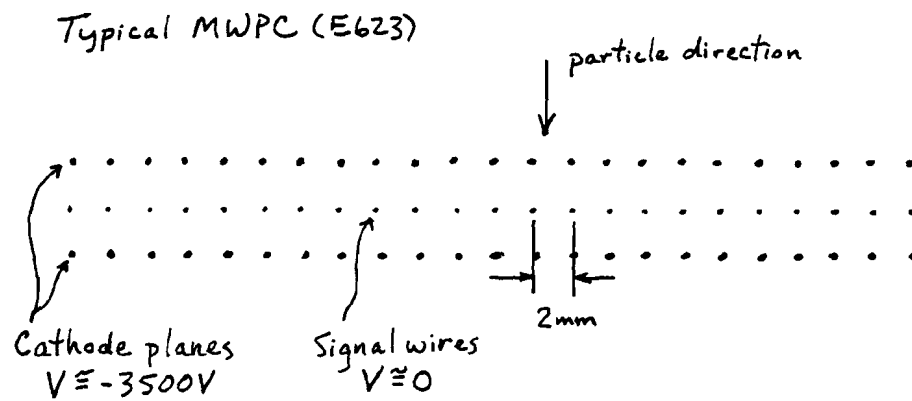


Fig. III.2 - Diagram of typical MWPC for E623.

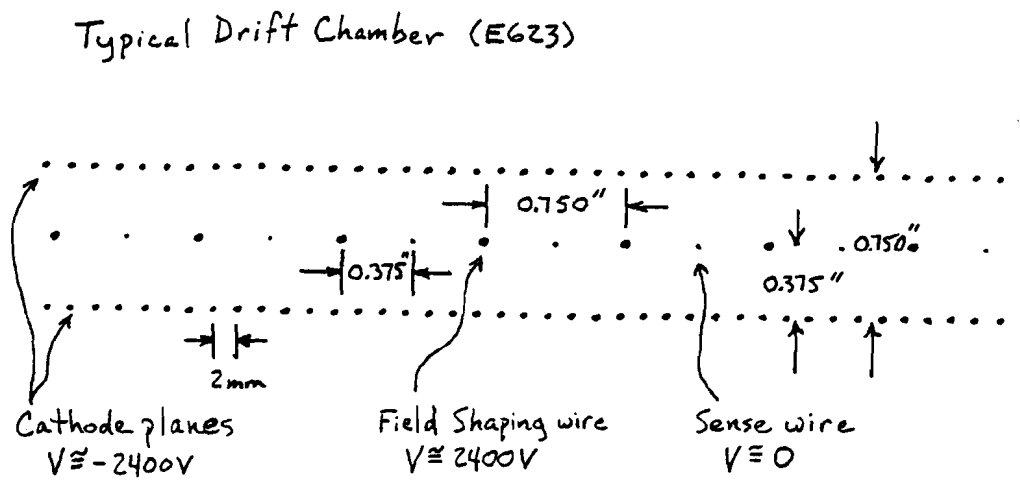


Fig. III.3 - Diagram of typical drift chamber for E623.

accelerated electrons ionize other molecules, releasing more electrons and creating an avalanche of electrons that eventually hit the wire creating a small current pulse. The current pulse is then amplified, converted to a voltage pulse and sent to the readout electronics. It is clear that the uncertainty in the position of the particle at the sense plane is equal to  $\pm 1/2$  the wire spacing in the direction perpendicular to the wires and in the wire plane. This nominally gives an error,  $\sigma$ , of  $(\text{wire spacing}/\sqrt{12})$  but in practice, the actual error is on the order of  $(\text{wire spacing}/\sqrt{6})$ . There is no information about the position of the particle along the direction of the wires. In order to get information about the position of the particle in both  $x$  and  $y$ , one must have pairs of planes in the  $x$  and  $y$  directions. However, since there are usually several particles passing through the chamber at the same time, one must also have some planes whose wires are tilted with respect to  $x$  and  $y$  in order to remove ambiguities in tracking. These are usually called  $u$  or  $v$  planes.

Drift chambers work on the same principle as MWPCs but the spacing between sense wires is usually much larger for a comparably sized chamber (Fig. III.3). Also, between every sense wire there is a field shaping wire. The field shaping wires are also at negative high

voltage. The purpose of the field shaping wires is to try to make the time required for the first electrons to arrive at the sense wire a linear function of the distance from the wire. Experimentally, the time to distance function was mapped out using the data and was fitted to a linear term plus some small correction terms. By measuring the time one can then find out how far the particle was from the wire. One cannot tell, however, on which side of the wire the particle passed. This is called the left-right ambiguity and can only be resolved by using additional information from other drift planes or MWPCs. The resolution of a drift chamber will depend on the gas mixture used, the precision with which the chamber was constructed and the resolution time of the electronics. Using a 50% Ar/Ethane mixture, the resolution of the drift planes in our system ranged from about 280 microns to 600 microns. For both MWPCs and drift chambers the maximum rates that can be achieved are on the order of  $10^6$  events/sec due to the time required for the ions to be collected. For the E623 drift chambers, the maximum drift time was about 720ns corresponding to the time required for an electron to drift across a half-cell ( $3/8''$ ). This gives a typical drift velocity of  $13\mu/\text{ns}$ .

The MWPCs in E623 were grouped into 8 stations

where, in general, each station consisted of several sense planes. For example the A station consisted of two x planes, two y planes, a u plane and a v plane. Three of the stations, BA1, BA2 and BB, were upstream of the target and were used for tracking the incident beam particles. Stations A and B were located between the target and the magnet, station C was inside the magnet aperture and stations D and F were downstream of the magnet. Signals from the wires were amplified by chamber-mounted preamplifiers with outputs connected to a set of shift registers. The shift registers received the signals from the wires in parallel and when given a TAKE\_DATA signal from the on-line computer, latched the inputs and began to shift the data out serially to be recorded.

The drift chamber planes were grouped into two stations, DA and DB, of four planes each and were located downstream of the magnet between MWPC stations D and F. Signals from the drift sense wires were amplified and discriminated at the chamber and then sent to a set of TDCs (Time to Digital Converters). A signal at the TDC will start a clock for that channel. At some later time, defined by a delayed signal from the incident beam particle, all channels were given a common stop signal. Taking into account particle travel time,



cable delays, amplifier delays, etc. we can compute the drift time for each wire and thus find the distance of the particle from the wire. Due to the fact that we used the common stop mode for the TDCs, if there were two tracks in a single cell, we would detect the last one to drift to the sense wire.

The target for the experiment consisted of 20 1.25"x1.25"x0.25" scintillator segments, each wrapped in 14 mils of aluminum tape and connected by plastic light pipes to photomultiplier tubes. The segments were tightly packed so that the total length of the target was approximately 5 inches. The amount of material in the target corresponded to 0.20 inelastic interactions/beam particle (20% target). The purpose of the scintillator target was to help reduce multiple scattering effects relative to a thinner but more dense material. The pulse height information from the phototubes gave an indication of the location of the primary interaction in the target and also that of secondary interactions if any occurred. This information was not used during the actual data taking however.

The Cerenkov counters  $C_A$  and  $C_B$  were perhaps the most important part of E623 since their function was to identify which particles were kaons. The type of

Cerenkov counters used in our experiment are known as multicell threshold Cerenkov counters. Each cell in the counter is basically independent so that particles traversing different cells can be identified separately. In a threshold counter, particles of a given mass will give light if their momentum exceeds  $mc/(n^2-1)^{0.5}$  GeV/c, where  $m$  is the mass of the particle in GeV/c<sup>2</sup> and  $n$  is the index of refraction of the gas in the counter. The relevant parameters for the Cerenkov counters in E623 can be seen in Table III.2. Figures III.4 and III.5 show the mirror sizes and arrangements for  $C_A$  and  $C_B$ . Since  $C_A$  was inside the magnetic field it was not used for particle identification but only as a high multiplicity veto.  $C_B$  was located just downstream of the D station. For our purposes, particles in the momentum range 5.8 to 23.0 GeV/c giving no light in  $C_B$  were defined to be kaons. On-line and off-line kaon definitions will be discussed in more detail later.

The scintillator hodoscope, SC (Fig. III.6), was located just downstream of drift station DB and was designed to shadow the central region of  $C_B$ . It was primarily used by the trigger processor to give better separation of pions and kaons in the forward direction, where the charged multiplicity was higher.

#### The Trigger and Trigger Processor

TABLE III.2

Cerenkov Counter Parameters for E623

Counter C<sub>A</sub>

40 cells

N<sub>2</sub> gas at 1 atmosphere

Index of refraction = 1.0003

Pion threshold = 5.69 GeV/c

Kaon threshold = 20.15 GeV/c

Proton threshold = 38.3 GeV/c

Mirror plane location -- z = 2.667m

Upstream window location -- z = 0.887m

Counter C<sub>B</sub>

30 cells

N<sub>2</sub> gas at 1 atmosphere

Mirror plane location -- z = 5.649m

Upstream window location -- z = 3.935m

$C_A$

44	43	42	41	40	39	38	37	36	35	34
33	32	31	30	29	28	27	26	25	24	23
22	21	20	19	18	17	16	15	14	13	12
11	10	9	8	7	6	5	4	3	2	1

Fig. III.4 - Map of  $C_A$  mirrors, looking downstream.

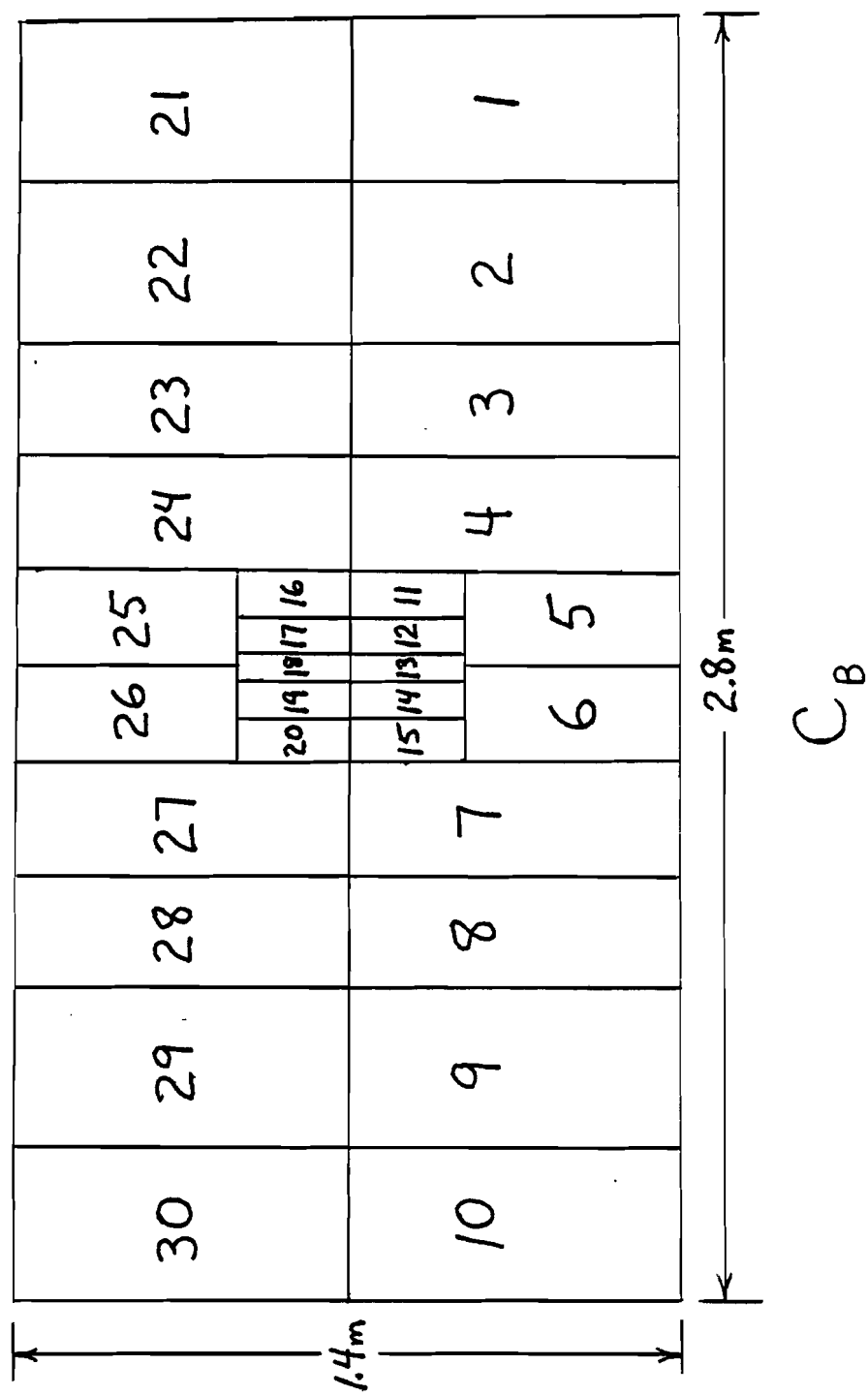


**Fig. III.5 - Map of  $C_B$  mirrors, looking downstream.**

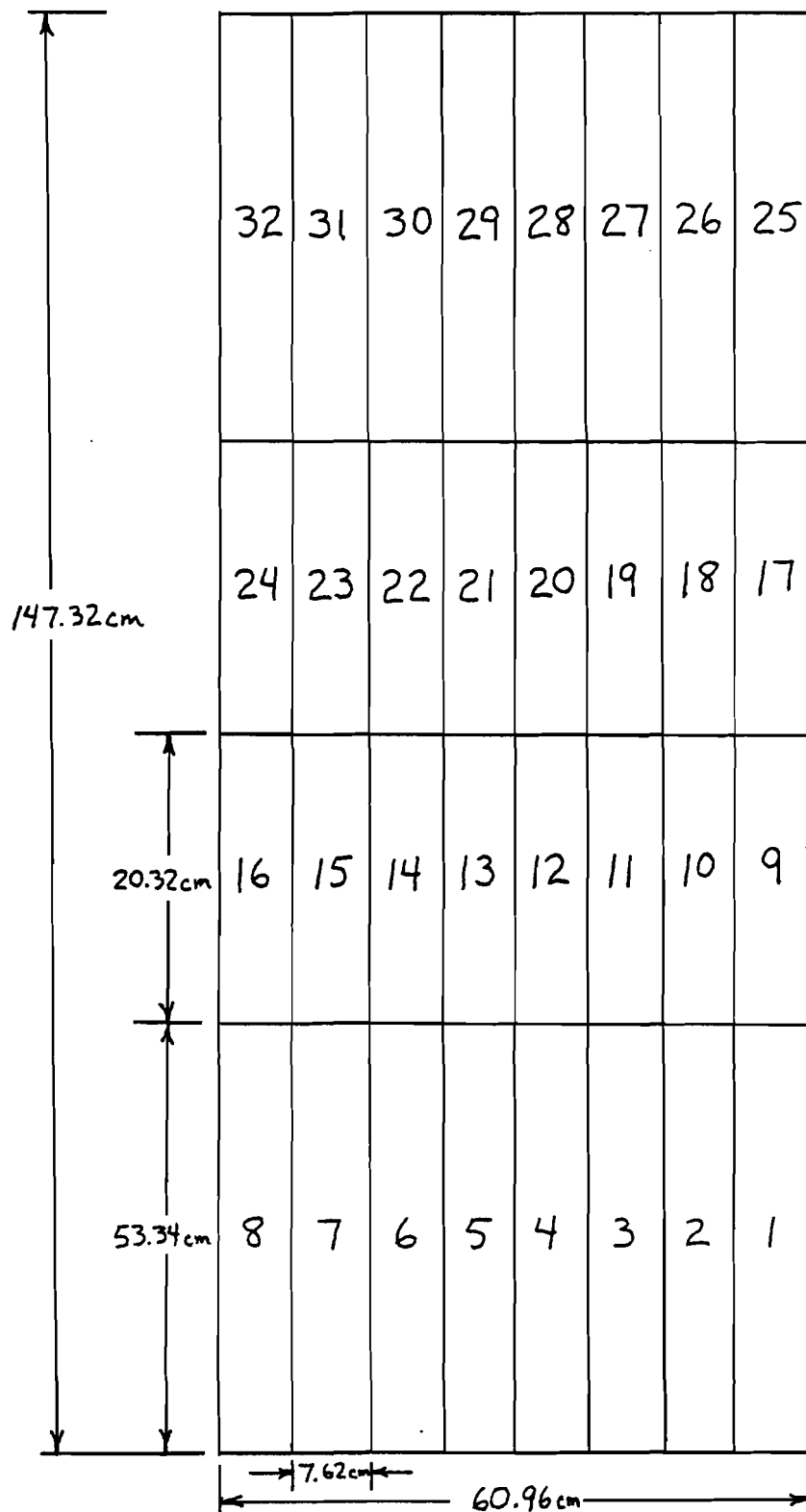


Fig. III.6 - Map of SC scintillator segments, looking downstream.

In order to look at processes with very small cross sections some method of distinguishing candidate events on-line must exist. The trigger in E623 performed this function by allowing only those events satisfying a set of predetermined conditions to be accepted and stored for later analysis.

The reaction that we are interested in is

$$p N \longrightarrow \phi \phi + X$$

where each  $\phi$  decays into a  $K^+K^-$  pair. Thus each event must have at least two  $K^+$  tracks and two  $K^-$  tracks in order to be considered and in addition, each  $K^+K^-$  pair must have low invariant mass. There are also the general requirements that the interaction take place in the target, the charged multiplicity not be too great, and the event not be too close in time to the previous event.

A good beam track was identified by using signals from three small scintillator counters, SA, SB and SC, located directly in front of the target. Counter SC was used to veto on wide angle beam tracks and had a hole in the center for the beam to pass through. The condition for accepting a beam particle was given by

$$BM = SA \cdot SB \cdot \overline{SC} \cdot BMGT$$

where BMGT was a signal from the accelerator that was on only during beam pulses.

An interaction in the target was defined in two ways. The first used DEDX, a scintillator counter directly behind the target that gave a signal proportional to the number of charged tracks passing through it. This allowed a threshold requirement to be used. The second method used 1X1, a 1" by 1" scintillator counter located downstream of the magnet between drift stations DA and DB and directly in the path of the beam. The absence of a signal from 1X1 was then used to indicate that an interaction had occurred. The definition of an interacting beam particle was then

$$IB = BM \cdot DEDX \cdot \overline{1X1} .$$

Within 50 ns of receiving an interacting beam signal, another signal, E (enable), was formed by requiring the number of cells having light in  $C_B$  to be less than five and the pulse height in DEDX be less than fifteen, in units corresponding to that given by a single minimum ionizing particle, so that

$$E = IB \cdot \overline{C_B > 5} \cdot \overline{DEDX > 15} .$$

The enable signal was used as a gate for the trigger processor. Given an enable pulse, the inputs to trigger processor and window discriminators were latched. If there was no enable the event was immediately discarded in order to reduce dead time.

The inputs to the trigger processor and window



discriminators consisted of signals from  $C_A$ ,  $C_B$  and SC along with signals from wire chamber planes CX, DX1, and DBX2. Figure III.7 shows the locations and active areas of the trigger chambers and detectors. The wire chamber signals were logically ORed at the the chamber by FNAL designed electronics (see Figs. III.8 and III.9) in order to form 32 element hodoscopes from each plane. The FNAL designed window discriminators (see Fig. III.10) produced a signal if the multiplicity  $N$  was between the limits,  $N=(NL,NH)$  defined as  $NL \leq N \leq NH$ .

The outputs from the window discriminators were used to form another gate, EG (event gate), defined by

$$EG = E \cdot CX(4,9) \cdot DX1(4,9) \cdot DBX2(4,10) \cdot \overline{CA} > 8 \cdot \overline{CB} > 6 \cdot \overline{SC} > 7 .$$

In addition, since events were preferentially selected in which  $C_B$  is inefficient, the multiplicities in  $C_A$  and  $C_B$  were required to agree within two.

The trigger processor used the signals from the wire chamber hodoscopes to identify candidate kaon tracks. A track was defined as a coincidental hit in all three elements of a predefined road through CX, DX1 and DBX2. A target point plus these three points provided redundant four point tracking. Each road was uniquely identified by its x-z (magnet bend plane) production angle  $\theta$  and momentum  $P$ . A satisfied road having no light in any  $C_B$  cells overlapping this road

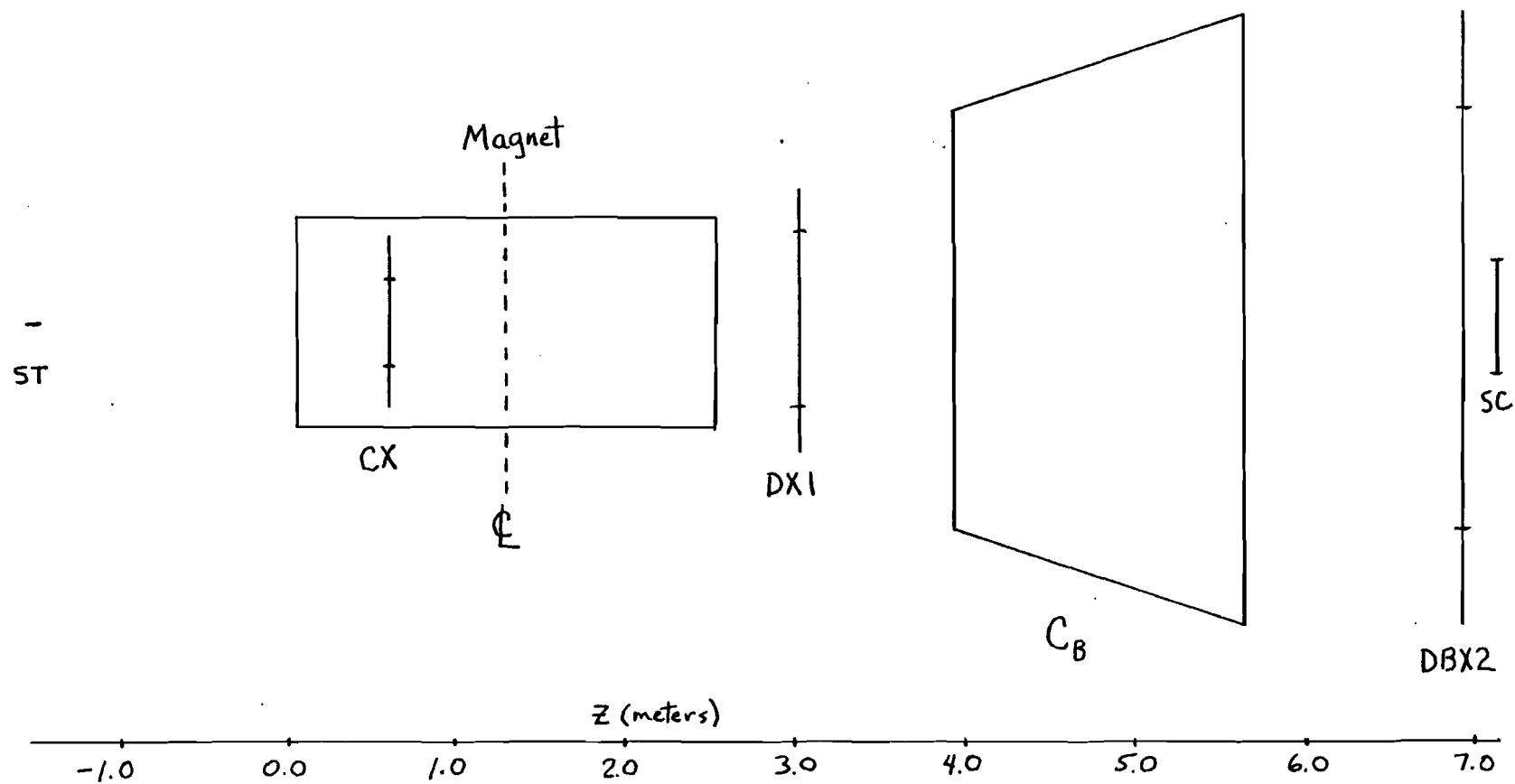


Fig. III.7 - Layout of MPS showing trigger chamber locations. Tic marks indicate active areas for triggering purposes.

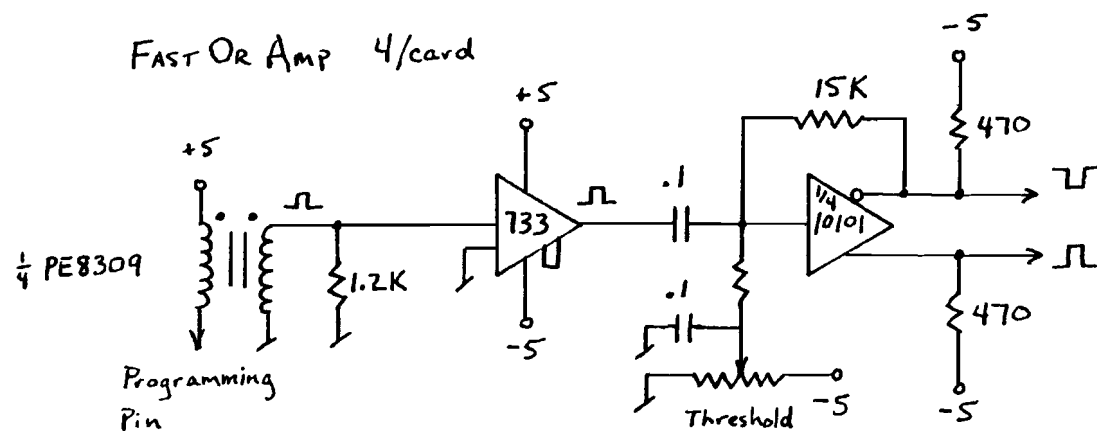
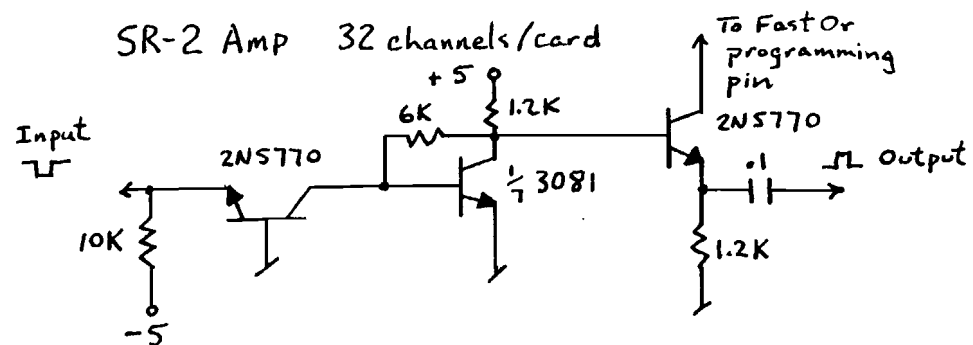
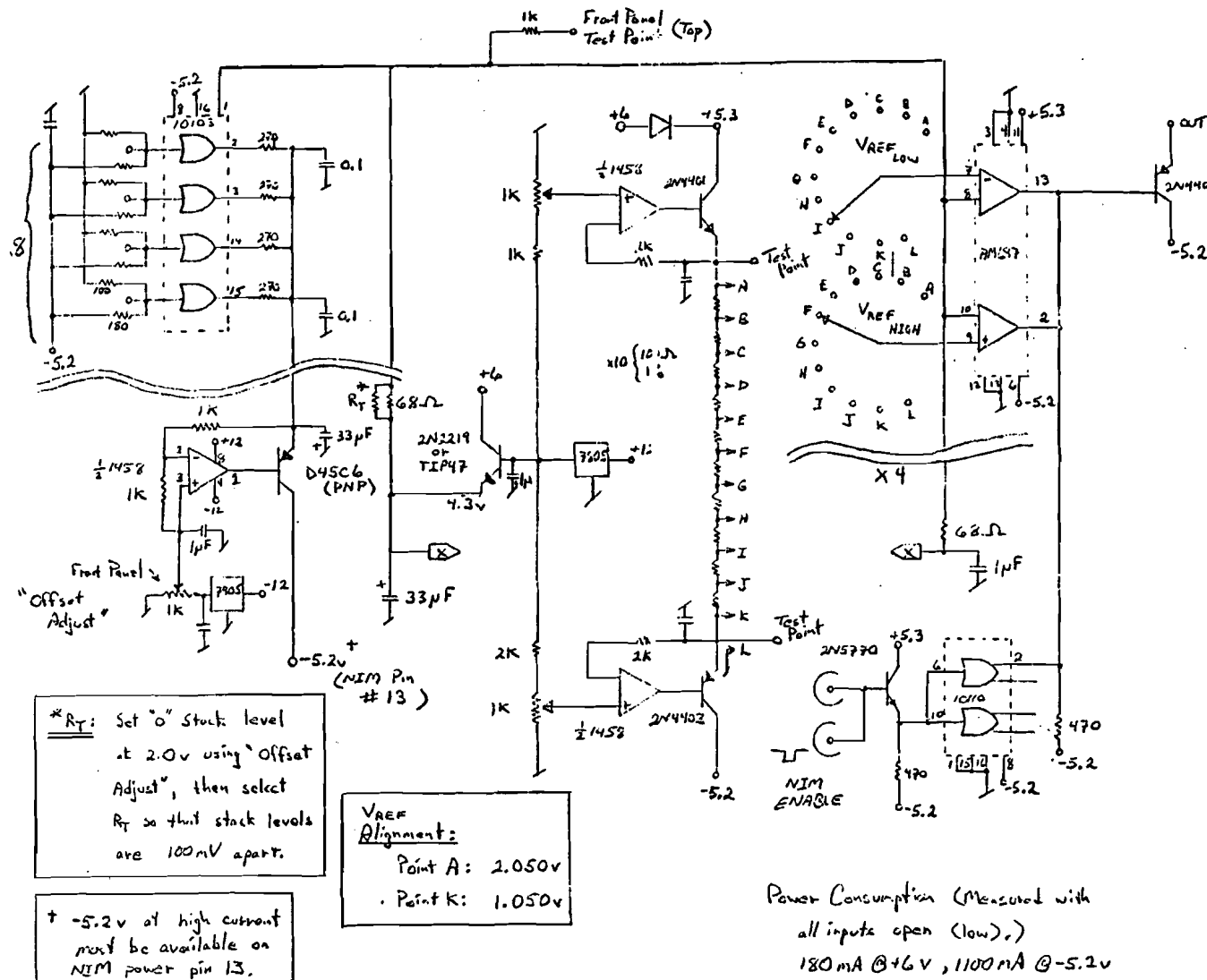


Fig. III.8 - Schematic diagram of Fast-Or MWPC chamber preamplifier.



Fig. III.10 - Schematic diagram of window discriminator designed for E623.



was defined to be a kaon. The scintillator hodoscope SC was also used for tracks in the central region of  $C_B$  where there was a high particle density. This allowed kaon candidates to be identified if a non-kaon(pion) track shared the same road but went through a different cell in  $C_B$ . The momentum range of identified kaons for the trigger processor was between about 6 and 22 GeV/c due to geometrical factors and the gas mixture used in  $C_B$ . If several tracks of the same charge shared the same production angle only the highest momentum track was reported to the higher level trigger processor logic.

The high level logic of the trigger processor used the momenta and production angles of the kaon tracks to compute the effective mass of selected  $K^+K^-$  pairs. For the  $\phi\phi$  trigger the desired bias was two pairs with small opening angles between the  $K^+$  and  $K^-$  in each pair and a large opening angle between the pairs to emphasize high  $\phi\phi$  effective masses. This was accomplished by choosing the pair of positive kaon tracks,  $K^+_L$  and  $K^+_R$ , having the most positive and most negative production angle respectively. The same was done for negative tracks  $K^-_L$  and  $K^-_R$ . The effective masses of the pairs  $K^+_L K^-_L$  and  $K^+_R K^-_R$  were then calculated from a memory look-up table using the approximation

$$M_{K+K-}^2 \cong P_+ P_- (\theta_+ - \theta_-)^2 .$$

If this was less than a Monte Carlo determined cut of  $(1.02 \text{ GeV}/c)^2$ , then the pair was accepted as a  $\phi$  candidate and the ML or MR flag was enabled. For  $\phi\phi$  triggers the requirement was

$$\phi\phi = EG \cdot K+(2,4) \cdot K-(2,4) \cdot ML \cdot MR .$$

The overall logic diagram for the E623 trigger is shown as Figure III.11. A more extensive discussion of the trigger and especially the trigger processor system and electronics can be found in the paper by Fenker et al. [Fen 82].

# E623 TRIGGER LOGIC

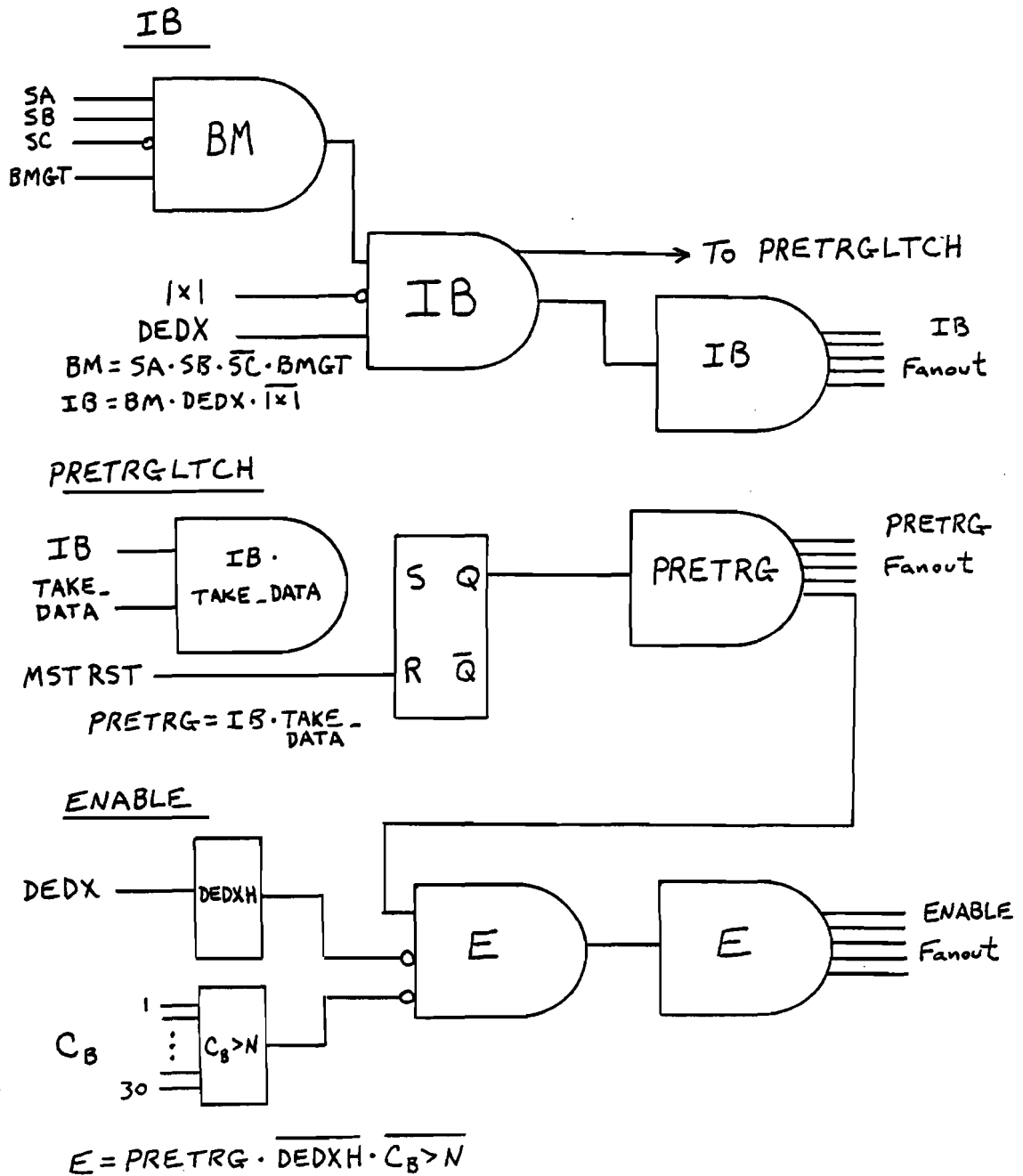


Fig. III.11 - E623 trigger logic diagram.



## OVERVIEW OF LATCHES

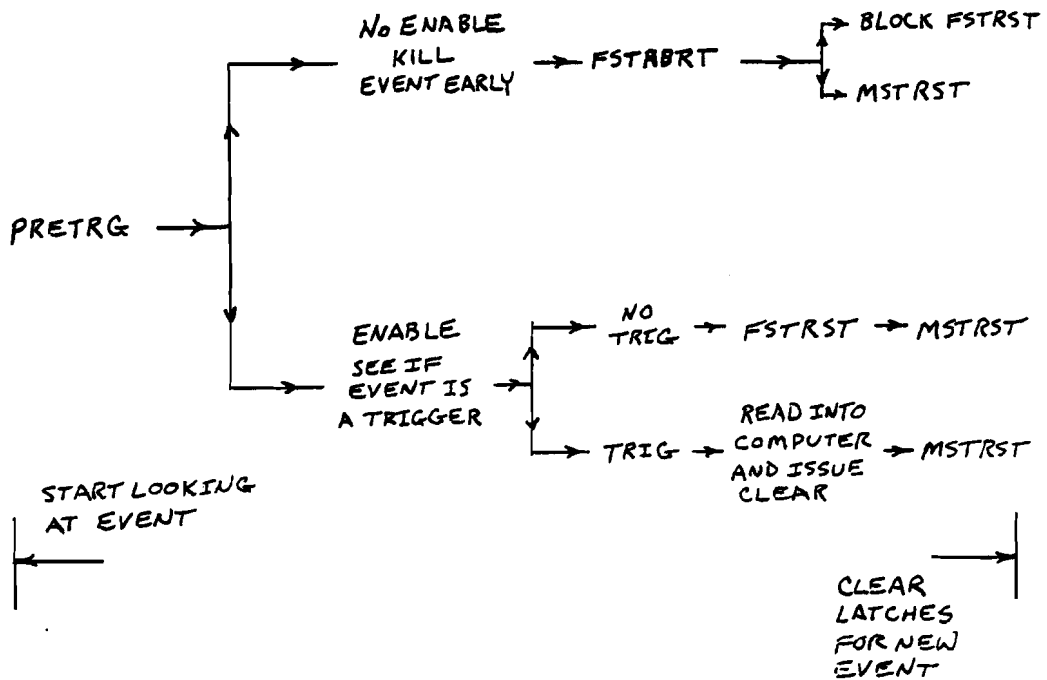
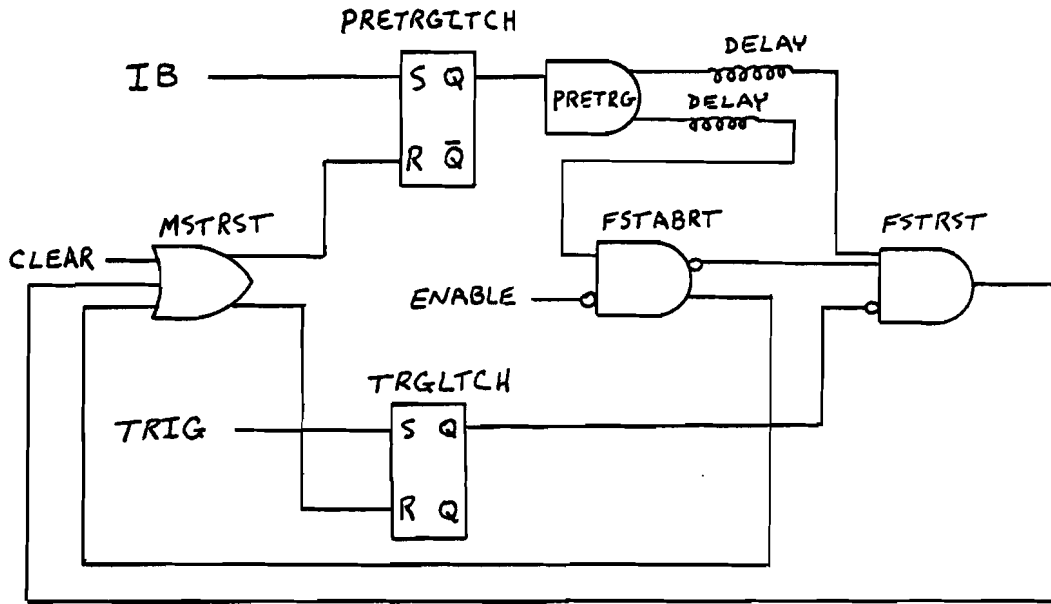


Fig. III.11 (continued)

## WINDOW DISCRIMINATORS

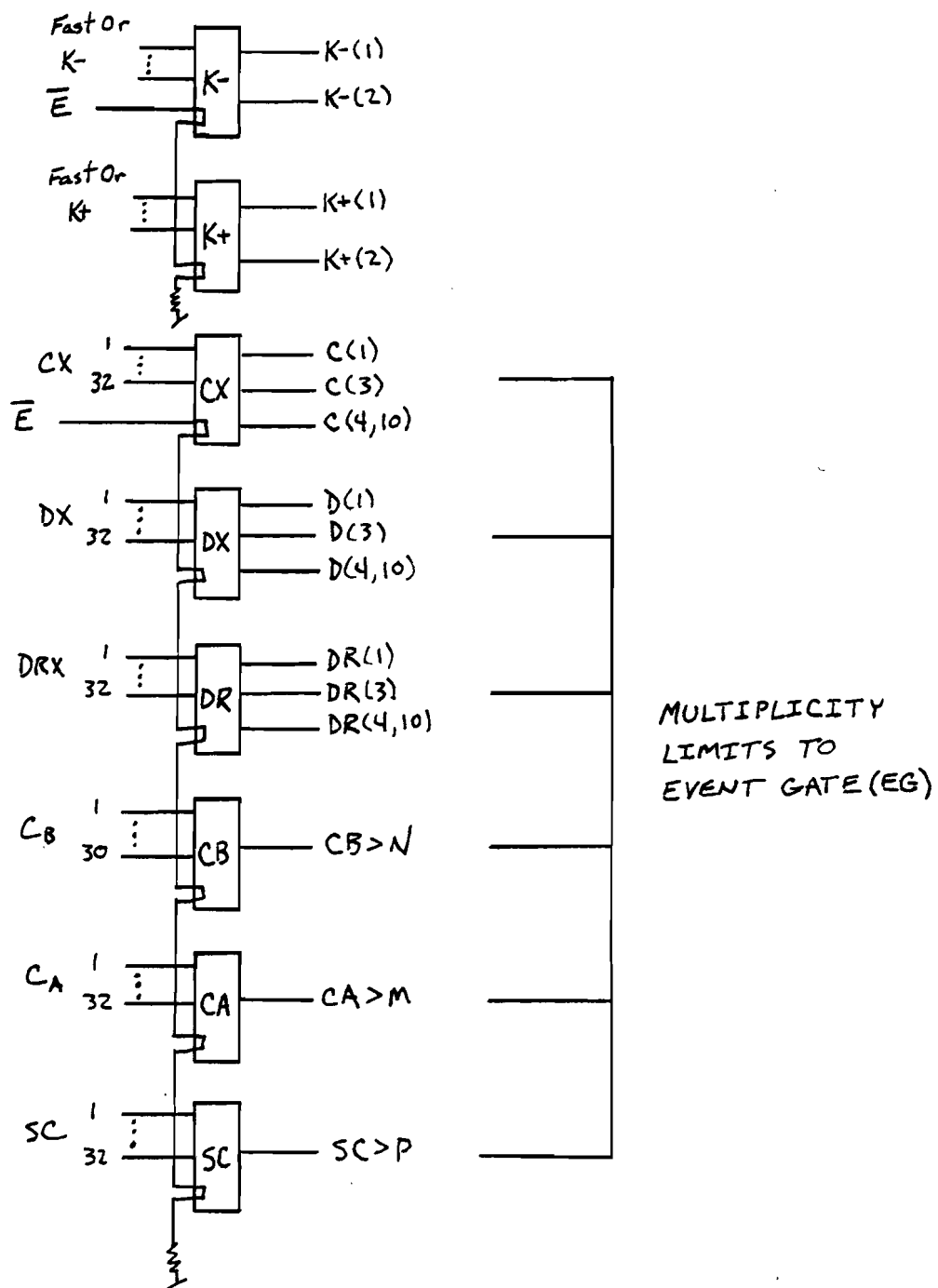


Fig. III.11 (continued)

## EVENT GATE

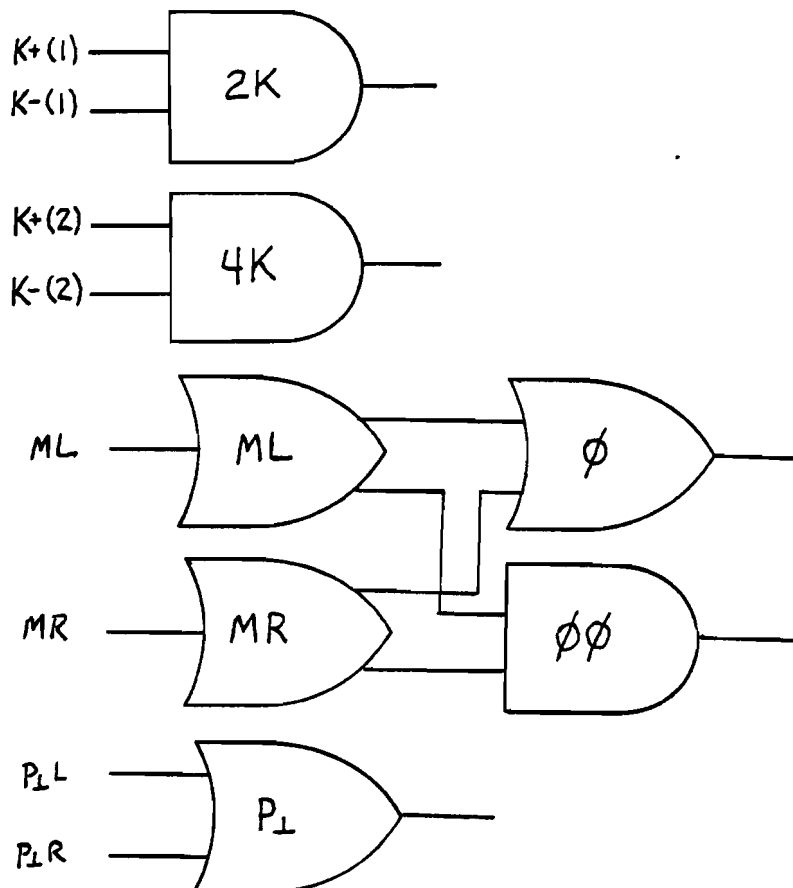
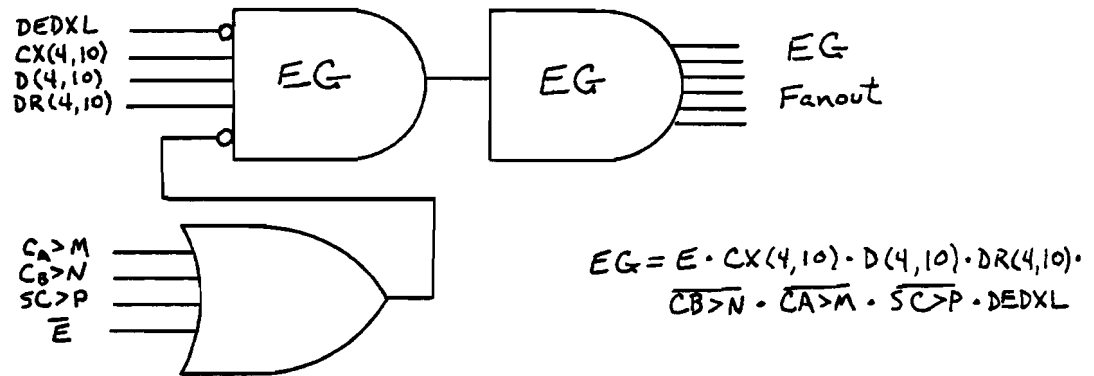


Fig. III.11 (continued)

## E623 TRIGGERS

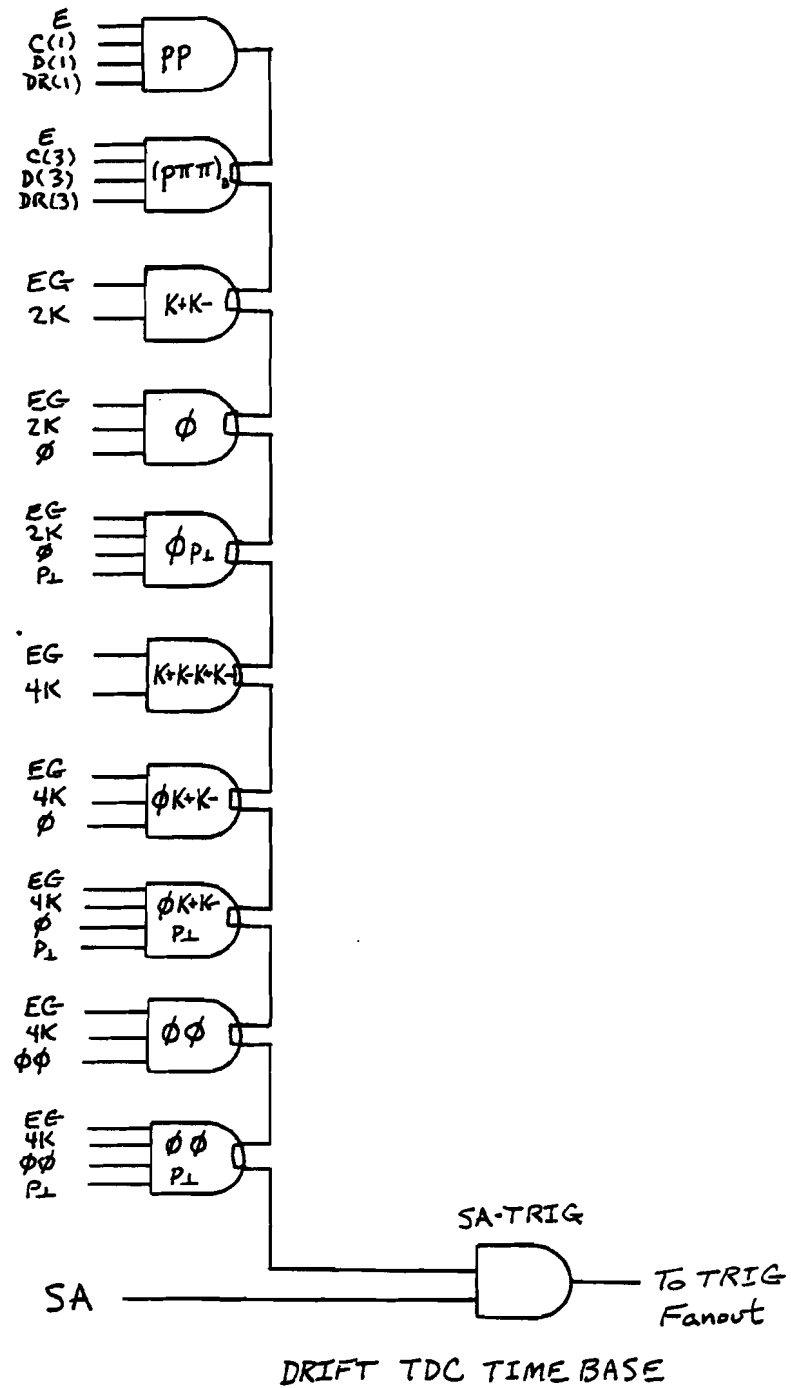


Fig. III.11 (continued)

## Chapter IV

### DATA PROCESSING

This chapter will describe the various processing programs that were used to reduce the raw data tapes from E623.

#### Pattern Recognition

The first stage in processing the data from E623 was pattern recognition, or track finding, and the FORTRAN program to perform the pattern recognition, FLOWERS, was written at FSU by Dr. J.H. Goldman. FLOWERS read physical records from magnetic tape, unpacked the condensed records into separate events, analyzed each event in the record and then read another record from the tape. The time required for pattern recognition processing was approximately seven CPU seconds per event on a VAX 11/780 computer.

In order to find the tracks of the charged particles in the spectrometer system the locations of the hits in the MWPCs and drift chambers had to be converted from relative locations in the wire chambers to physical coordinates in the laboratory. To do this, one needs to know the locations and orientations of the

wire chambers with respect to a fixed coordinate system. Measurement of these distances and angles was performed in a survey.

The coordinate system that was used defined the  $z$ -axis as the nominal beam direction with  $z=0$  at the upstream face of the spectrometer magnet. The  $x$  and  $y$ -axes were centered on the beam direction with the  $x$ -axis being vertical and the  $y$ -axis defining a right-handed system (Figure IV.1). The positions of several wire planes upstream and downstream of the magnet were carefully measured and an alignment of all the other planes in the system was done relative to these planes using low multiplicity events with the magnet off, so that all tracks were straight lines in both the  $x$  and  $y$  projections.

The algorithm for track finding used by FLOWERS started by finding a vertex point in the target by using beam track information, if available, or if not, by simply using the center of the target. Next, the tracks were found downstream of the magnet in the  $x$ - $z$  view since the tracks are more widely separated there. The intercept for each of these tracks was found at the center of the magnet and a "road" was defined from this point to the target vertex point. The road was then searched for hits in the  $x$ - $z$  view upstream of the magnet

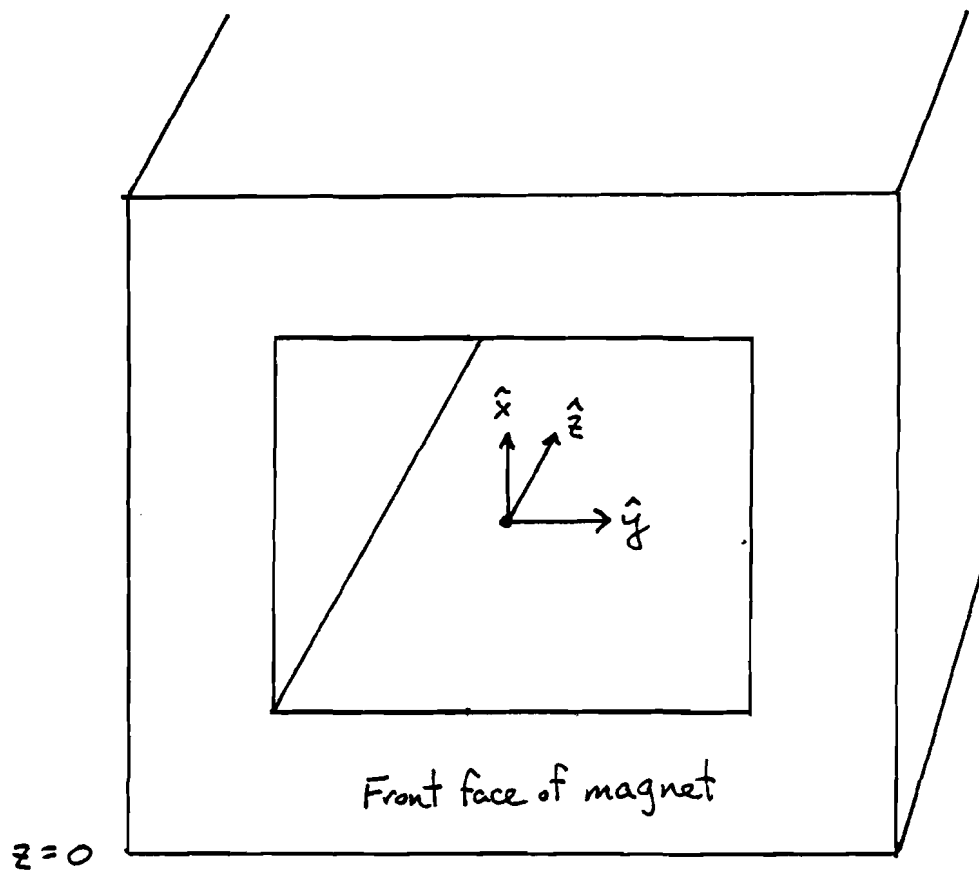


Fig. IV.1 - Orientation of coordinate system used in E623.

that gave the best fit for each track. This gave the complete track in the x-z view. Next, the farthest downstream y and u,v hits were used to define roads directly from the target since there is no bending versus arc length in the y-z view. Since each y-z road with an x-z track totally defines the entire track, the other y and u,v hits were matched by finding the combination that maximized the total number of u,v hits and gave a good fit to the track.

#### Track Fitting

The output from FLOWERS was processed by a track fitting program named TIPTOE. TIPTOE used different sets of alignment data for each section of the experimental run where some change had been made in the positions of the wire chambers, for example, when a chamber had to be taken out to be repaired and then put back in place.

Information from the scintillator wall behind  $C_B$  was first used to flag tracks from pattern recognition that should have hit the wall but failed to give a signal in the appropriate cell. These tracks were given an IVC=5 flag.

A simple particle identification routine used discriminated phototube signals from each cell of  $C_B$ , the  $C_B$  bits, to count the number of charged kaon



candidates in the event. If one or more central ( $5.5 < p < 25$  GeV/c) tracks passed through a  $C_B$  cell and the bit was off, then those tracks were counted as kaon candidates. If the bit was on and more than one central track hit the same cell, then one of the central tracks was counted as a pion and the other central tracks were counted as kaons. If the event contained fewer than one  $K^+$  or fewer than one  $K^-$  candidate it was thrown out.

After passing the particle identification cut, the tracks in each event were then fitted with a six-parameter least-squares algorithm that connected upstream and downstream track segments using a magnetic field map to swim the charged tracks through the magnet. Tracks not passing certain minimum quality cuts such as number of hits in each view, total number of hits, chi-squared for the fit, etc. were given various IVC flags depending of the reason for failure.

Finally, after requiring that the event have at least one  $K^+$  candidate and one  $K^-$  candidate track and a minimum of three total tracks, a vertex fit was done which minimized the distance of each track from a common vertex point by varying the upstream track parameters.

#### Particle Identification

Since we are trying to look for charged kaons coming from the decay of  $\phi$  mesons we must have some

method of distinguishing charged kaons from other types of charged particles such as pions, protons, muons etc.

Wire chambers and scintillators give signals for any type of charged particle that passes through them so that what is required is a device that will distinguish among charged particles according to their mass. One such device, and the one used in E623, is the threshold Cerenkov counter.

As discussed in Chapter 2 and the Appendix, when a charged particle of mass  $m$  travels through a medium having an index of refraction  $n$  at a velocity  $v$  exceeding the speed of light in the medium, radiation will be emitted in a cone of half angle  $\theta$  where  $\cos\theta = 1/\beta n$  and  $\beta = v/c$ . The threshold for emission of radiation will be when  $\theta = 0$  corresponding to a threshold momentum of  $p_{\text{thresh}} = mc/(n^2 - 1)^{0.5}$  GeV/c. Thus, a charged particle of mass  $m$  having momentum greater than  $p_{\text{thresh}}$  will emit radiation.

For E623, the Cerenkov counter  $C_B$  was filled with nitrogen gas at one atmosphere having index of refraction  $n = 1.0003$ . The calculated threshold momenta for pions, kaons and protons were 5.69, 20.15 and 38.30 GeV/c respectively. Thus kaons in the momentum range  $5.69 < p < 20.15$  should not give light in  $C_B$ , while a pion in this range will give light. Protons in this

range will also give no light and will not be able to be distinguished from kaons.

From the Appendix we find that the number of photons (in the visible spectrum) expected to be emitted per centimeter of radiator will be given by

$$N(\text{photons/cm}) = N_{\text{max}}(\text{photons/cm})[1 - (p_{\text{thresh}}/p)^2]$$

where  $N_{\text{max}}$  is the average number expected for a  $\beta=1$  particle.

For  $C_B$ , taking into account the average length of radiator travelled, collection efficiencies, quantum efficiencies of the phototubes, we find experimentally that the average number of photoelectrons detected by a phototube for a  $\beta=1$  particle is approximately six, giving

$$N_{\text{photoelectrons}} \approx 6.0 * [1 - (p_{\text{thresh}}/p)^2].$$

It should be noted that for particles of a given momentum the actual number of photoelectrons detected will be distributed according to a Poisson distribution. Figure IV.2 shows the average number of photoelectrons expected for pions of a given momentum in  $C_B$ . This number rises very sharply just above pion threshold, but since the distribution is Poisson there will be a significant probability of detecting no photoelectrons in this region leading to misidentification of pions as kaons.

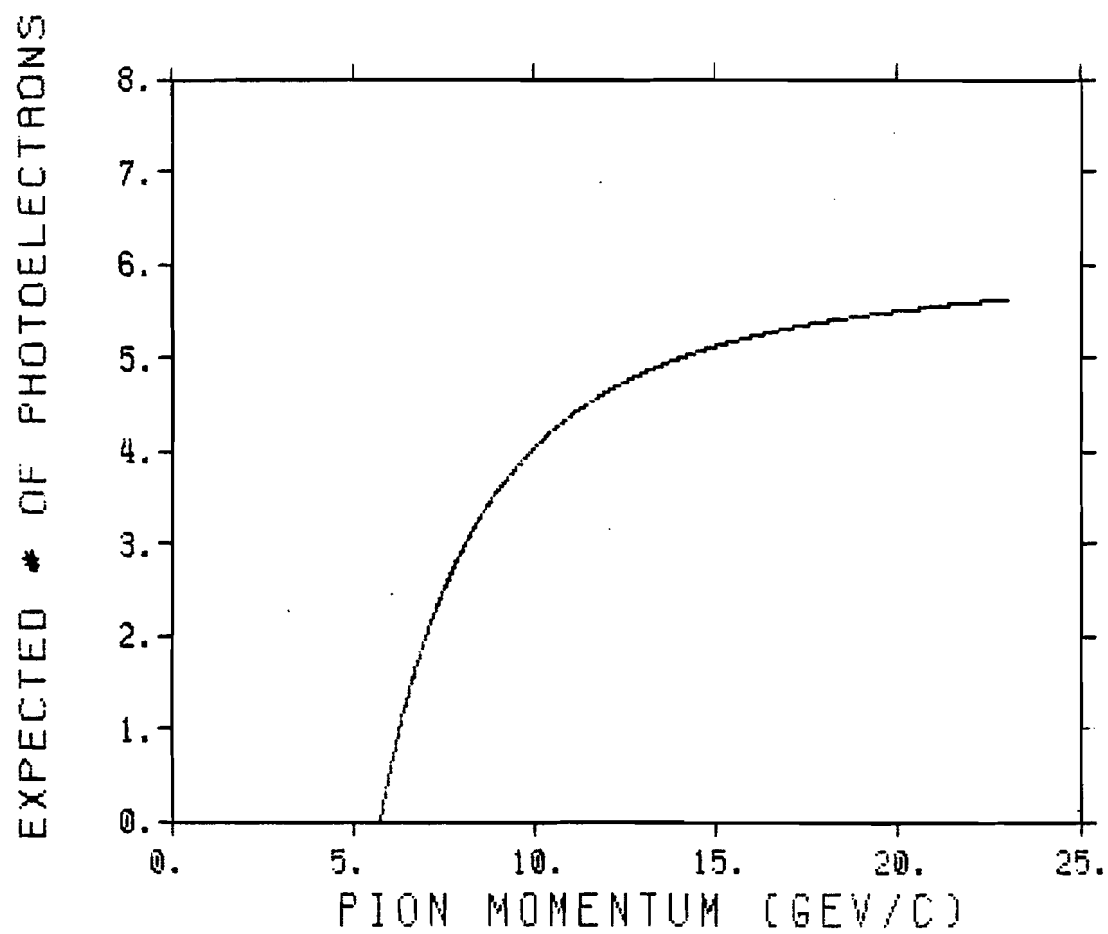


Fig. IV.2 - Expected number of photoelectrons for a pion in counter  $C_B$  versus momentum.

The photoelectrons collected by the phototube create a current at the tube anode which is connected to an ADC (Analog to Digital Converter). The ADC integrates the current pulse, measures the charge found and converts this to a form that can be read into the computer. After subtracting the pedestal or zero-value of the ADC, this number should be proportional to the number of photoelectrons detected by the phototube (See Fig. IV.3). The ADC values used for each mirror in  $C_B$  are listed in Table IV.1.

#### Particle Identification Algorithm

The algorithm used for particle identification in E623 was written by C. Georgiopoulos at Tufts University and will now be described in some detail since it is an essential part of the analysis.

For each track in the event, the Cerenkov cone in  $C_B$  was calculated as if the track were a pion. The intersection of the cone with the  $C_B$  mirrors was weighted to take into account the  $1/r$  dependence of the distribution of photons in the cone (See Appendix).

For each track, the expected number of photoelectrons was calculated assuming the particle was a pion, kaon or a proton using the formula discussed previously. All the weighted numbers of photoelectrons for the tracks were then stored by  $C_B$  mirror number and

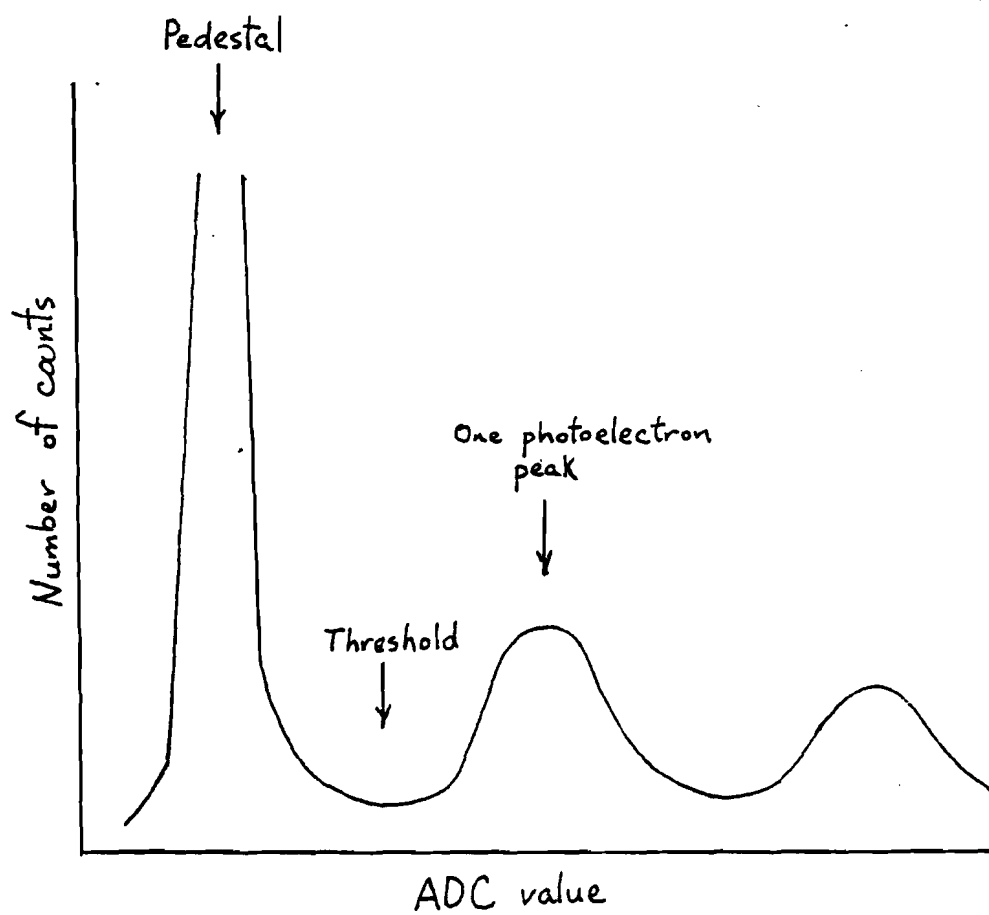


Fig. IV.3 - Typical spectrum for a  $C_B$  ADC channel.

TABLE IV.1

 $C_B$  ADC Values for Particle Identification Algorithm

(ADC dynamic range 0-1024 counts)

$C_B$ Mirror	Pedestal	Threshold (above ped.)	One Photoelectron (above ped.)
1	25	3	0
2	19	5	27
3	25	1	17
4	19	3	12
5	21	5	10
6	20	6	23
7	21	3	24
8	21	3	14
9	21	4	12
10	22	3	18
11	22	3	14
12	22	2	15
13	21	1	14
14	20	3	18
15	32	4	26
16	21	3	20
17	10	10	20
18	10	3	23
19	8	3	17
20	0	4	28
21	9	3	10
22	11	4	10
23	9	4	19
24	12	3	10
25	21	3	17
26	21	3	30
27	21	3	20
28	22	3	14
29	21	3	20
30	20	3	10

an expected pulse height was calculated for each mirror.

For mirrors with an observed pulse height above threshold, the tracks through each mirror were identified according to momentum. For a track to have been identified, it must have had at least 30% of its weighted area inside the mirror in question.

For mirrors with an observed pulse height above threshold, the number of photoelectrons detected by the phototube was calculated. Then the tracks that had all or some of their Cerenkov cone in that mirror were examined. For tracks above proton threshold, the expected number of photoelectrons for that track was subtracted from the observed number in the mirror, assuming the track was either a pion, kaon or proton. The identification was assigned that yielded the result closest to zero. If there were still photoelectrons left over, the same procedure was followed for tracks above kaon threshold. If there were no photoelectrons left over, the tracks were assigned an identification according to their momentum. Otherwise the remaining photoelectrons were compared with the expected value for these tracks and a decision was made accordingly. Note that the decision for each track was based on information obtained from the mirror that the track passed through.



The different ID types for the tracks are seen in Table IV.2. Those events having at least one positive and one negative track with ID=2 and at least one other charged track were kept for later analysis.

#### Data Summary Tape

The DST (data summary tape) contained all events that were used in the final physics analysis for this thesis. The events were required to have a vertex in or very near the smart target and all tracks in the event were checked against each other for duplicate track parameters. If two tracks had the same upstream  $y$ -slope within 0.3 mrad, the track with the lower quality was thrown out of the event. The quality of a track was determined by the total number of chamber hits on the track and by the chi-squared per degree of freedom of the fit to the track.

Since in this analysis we were looking for events with two  $\phi$  mesons, each event was also required to have at least two identified  $K^+$  and two identified  $K^-$  tracks, where identified meant the track had ID=2(kaon), with momentum above 5.8 GeV/c and IVC=0.

TABLE IV.2

Particle ID Types from  $C_B$  Analysis

<u>ID Type</u>	<u>Meaning</u>
0	$\pi/K/p$ ambiguous. Tracks with momenta below pion threshold that gave no light.
1	$\pi$ . Tracks with momenta between pion and kaon thresholds that gave light.
2	$K/p$ ambiguous. Tracks with momenta between pion and kaon thresholds that gave no light.
3	$p$ . Tracks with momenta between kaon and proton thresholds that gave no light.
4	$\pi/K$ ambiguous. Tracks with momenta between kaon and proton thresholds that gave light.
5	$\pi/K/p$ ambiguous. Tracks with momenta above proton threshold that gave light.
6	Unidentified. The algorithm was unable to decide, e.g., track cone split between 4 mirrors, more than 4 tracks in one mirror.
7	Tracks with momenta above proton threshold that gave no light.
8,9	Tracks with momenta below pion threshold that gave light.

## Chapter V

### DATA PRESENTATION AND DISCUSSION

After making all cuts to the data as described in Chapter IV, there were a total of 123,507 events having at least two identified kaons of each charge type. All plots of E623 data in the rest of this thesis were made from this sample.

#### Mass Plots

The  $K+K^-$  invariant mass spectrum from threshold to  $1.08 \text{ GeV}/c^2$  can be seen in Figure V.1. The  $\phi$  resonance is clearly visible around 1.02 GeV. A fit to the spectrum was performed using a function of the form

$$C x^{\alpha} (1-x)^{\beta} ,$$

to represent the background, where  $C$ ,  $\alpha$  and  $\beta$  were parameters to be varied and  $x$  was the rescaled mass defined to be between zero and one. The contribution from the  $\phi$  resonance was fitted to a Gaussian distribution of standard form.

The value for the  $\phi$  mass from the fit was  $1.0197 \pm .0003 \text{ GeV}$ , in good agreement with the accepted value of  $1.0196 \text{ GeV}$ . The fitted value for  $\sigma$  (standard deviation of the Gaussian) was  $4.4 \pm .4 \text{ MeV}$  corresponding to a

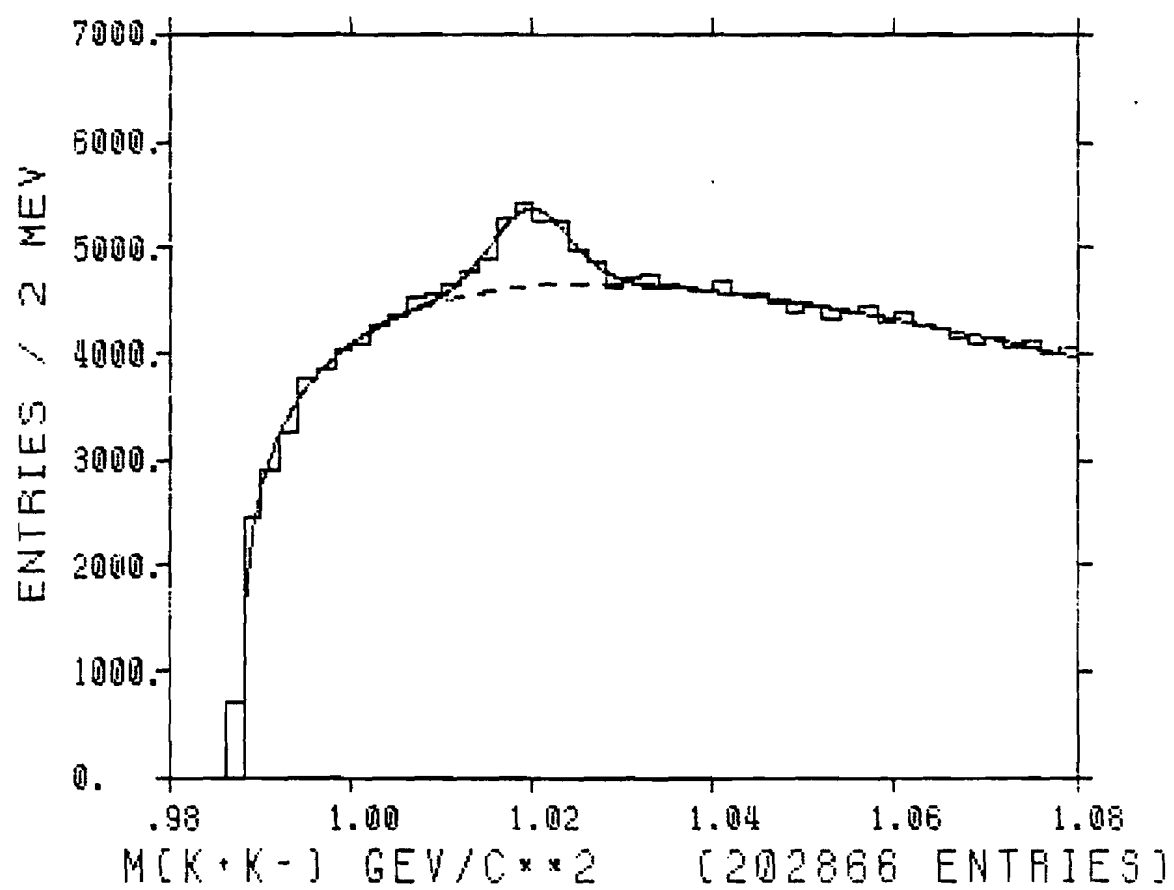


Fig. V.1 -  $K^+K^-$  invariant mass spectrum from E623.

full width at half maximum(FWHM) of  $10.3 \pm 0.9$  MeV. This is much wider than the known natural width of the  $\phi$  of 4 MeV and we assume that the experimental error dominates the natural width. This is why a Gaussian function was used for the fit rather than a Breit-Wigner.

Since each event has at least 2  $K^+$  and 2  $K^-$  tracks we can make a plot of the other  $K^+K^-$  mass combination when the first one lies in the  $\phi$  mass range, that is within  $\pm 6$  MeV of the nominal  $\phi$  mass. This spectrum is shown in Figure V.2. The second  $\phi$  signal is clearly evident above the background.

A fit was done to the spectrum in Fig. V.2 using the same form as before. The fitted value for the  $\phi$  mass was  $1.0199 \pm .0005$  GeV with a value for  $\sigma$  of  $3.6 \pm 0.7$  MeV corresponding to a FWHM of  $8.4 \pm 1.6$  MeV. There were  $538 \pm 92$  entries in the integrated Gaussian peak.

The  $K^+K^-K^+K^-$  and  $\phi K^+K^-$  invariant mass spectra are shown in Figure V.3 and V.4 respectively. The solid curves on both spectra are fits of the form

$$-X^2 + AXY + B^2Y^2 + CX + DY + E = 0 ,$$

where  $X$  is the mass value and  $Y$  is the number of entries in the bin. This form was used because of its relatively few parameters and its simple properties with respect to finding starting values for the fit.

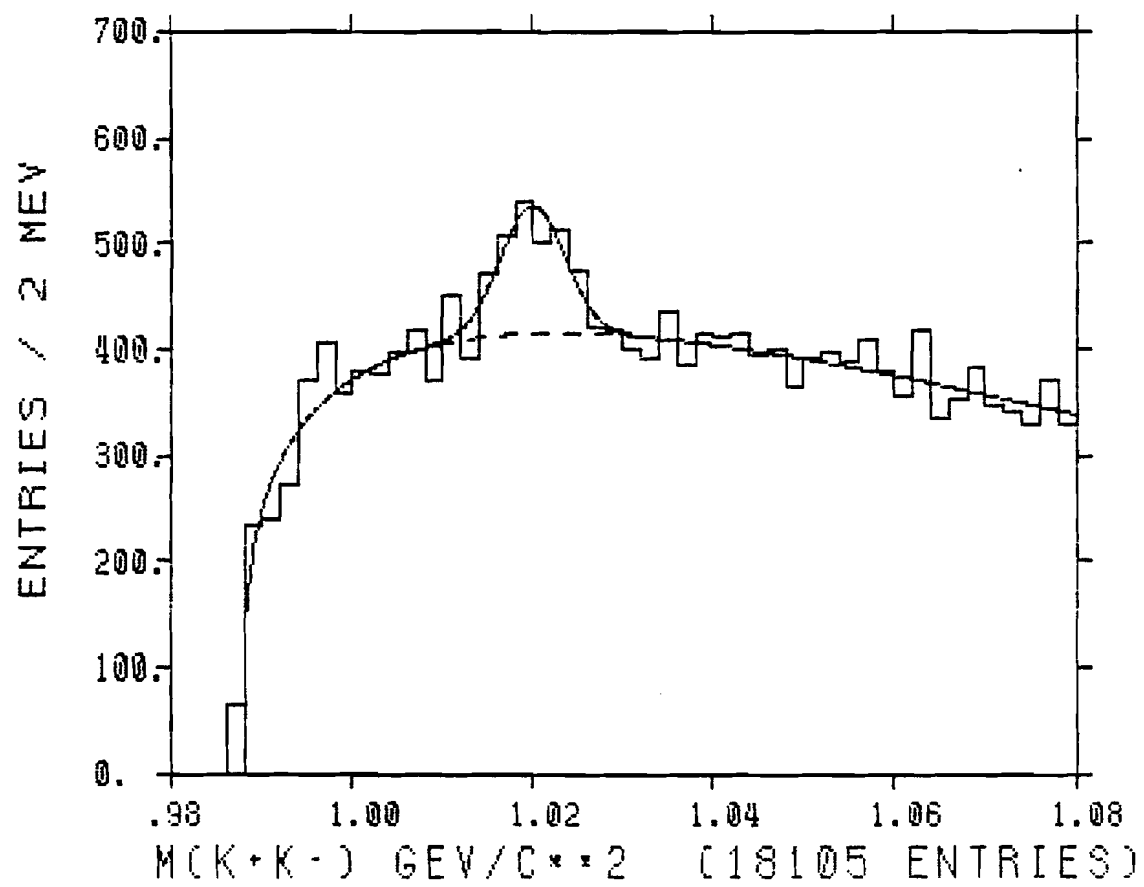


Fig. V.2 - K<sup>+</sup>K<sup>-</sup> invariant mass, cut on other  $\phi$  ( $\pm 6$  MeV wide).

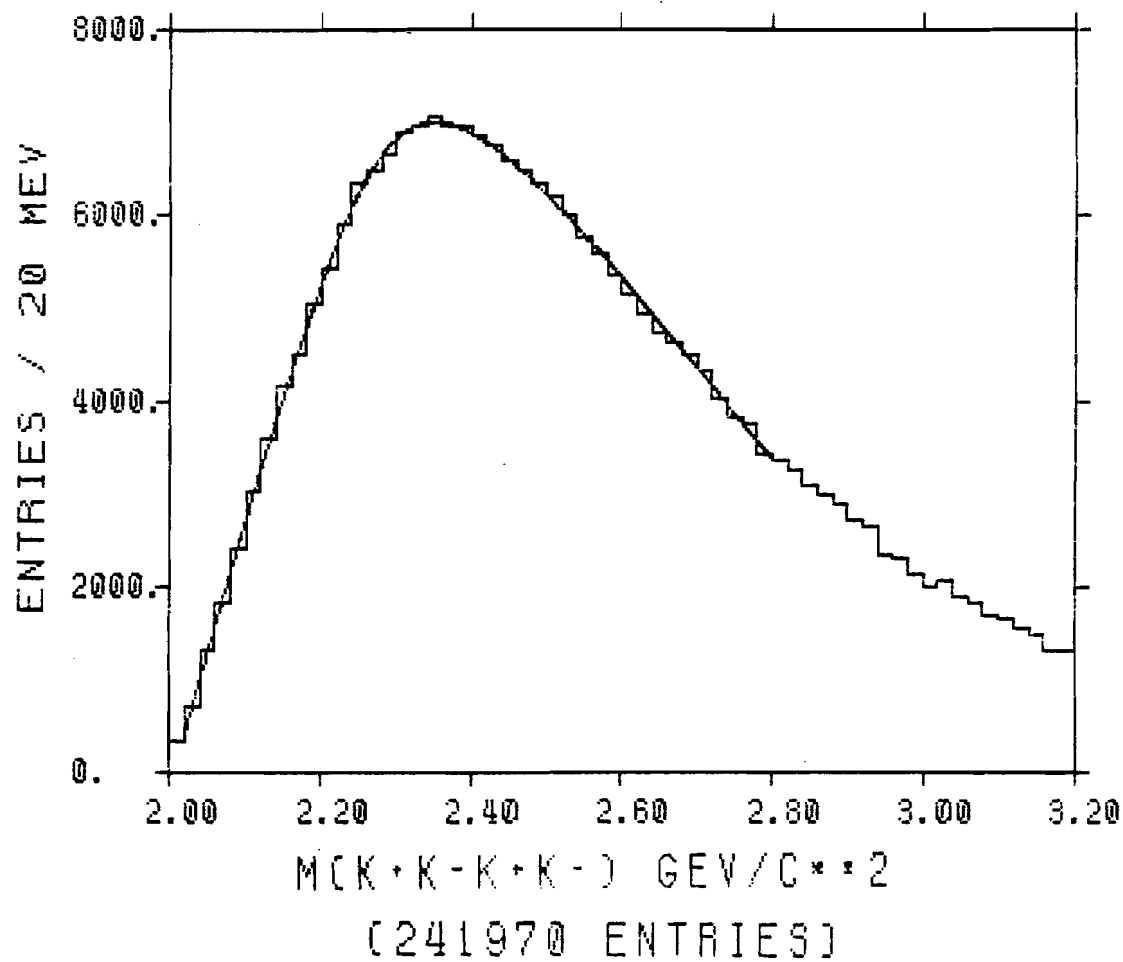


Fig. V.3 -  $K^+K^-K^+K^-$  invariant mass spectrum.

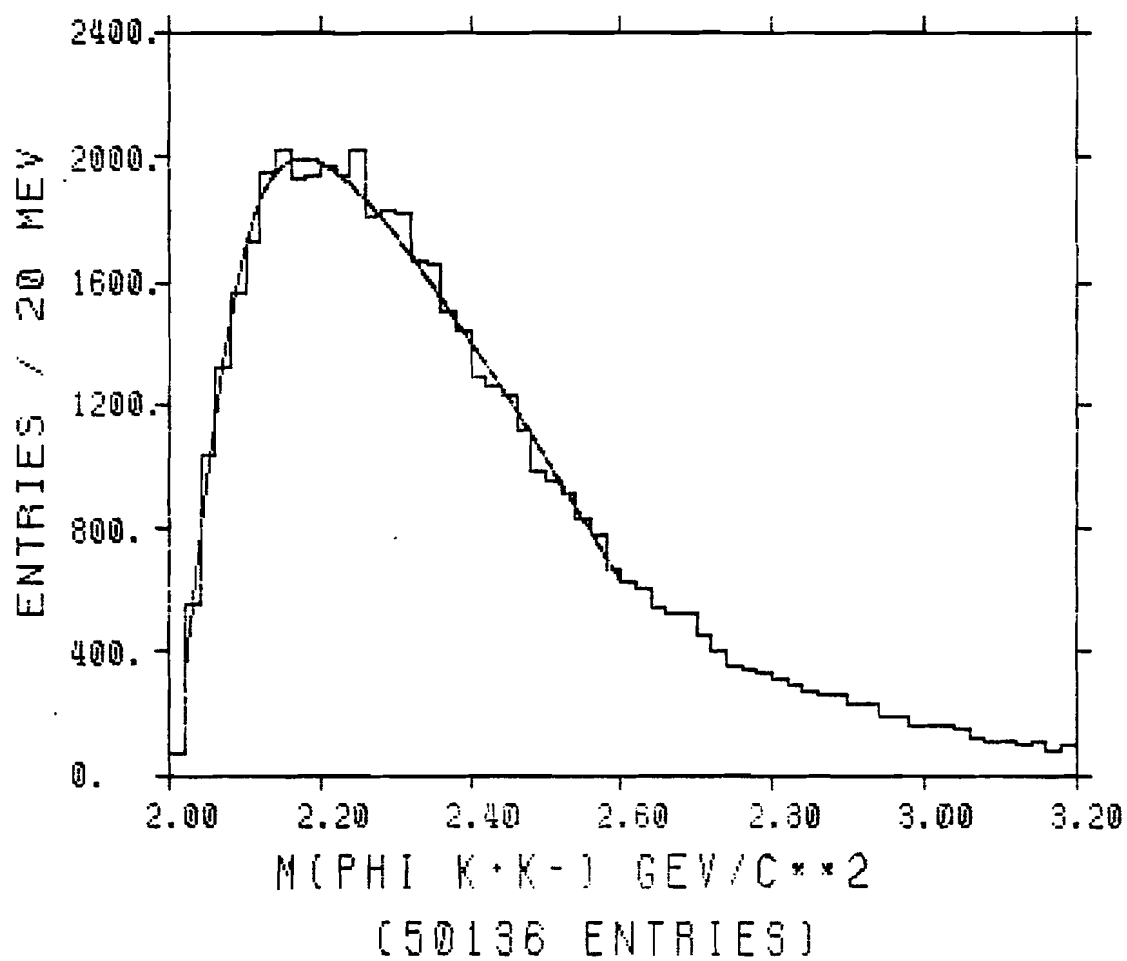


Fig. V.4 -  $\phi K^+ K^-$  invariant mass spectrum.



The fit to the  $K+K-K+K-$  spectrum seems to be an excellent representation of the data in that region. The  $\chi^2/\text{DOF}$  for the fit is approximately 25/34. There does not appear to be any evidence for structure in this spectrum.

The fit to the  $\phi K+K-$  spectrum is not unreasonable but it is clearly not as good as in the  $K+K-K+K-$  spectrum, having a  $\chi^2/\text{DOF}$  of 48/24. The difficulty in fitting the region from around 2.10 to 2.30  $\text{GeV}/c^2$  to a simple form indicates that some structure may be present in the region. The recent report [Hit 84] of a new narrow state at 2.220  $\text{GeV}/c^2$ , the  $\xi(2220)$ , decaying to  $K+K-$ , also indicates that this mass region may have some resonance structure. However, after some analysis, it was decided that no firm conclusions could be drawn from the data in this region.

For the  $\phi\phi$  mass spectrum, the mass of both  $K+K-$  combinations was required to be within  $\pm 6$  MeV of the nominal  $\phi$  mass. This spectrum is shown in Figure V.5. There is a very sharp rise at threshold and the spectrum drops again quickly by 2.20 GeV. The spectrum falls essentially to zero by 2.70 GeV.

In order to estimate how much of this spectrum is true  $\phi\phi$  production, as opposed to the background processes  $K+K-K+K-$  and  $\phi K+K-$ , one must look at the two

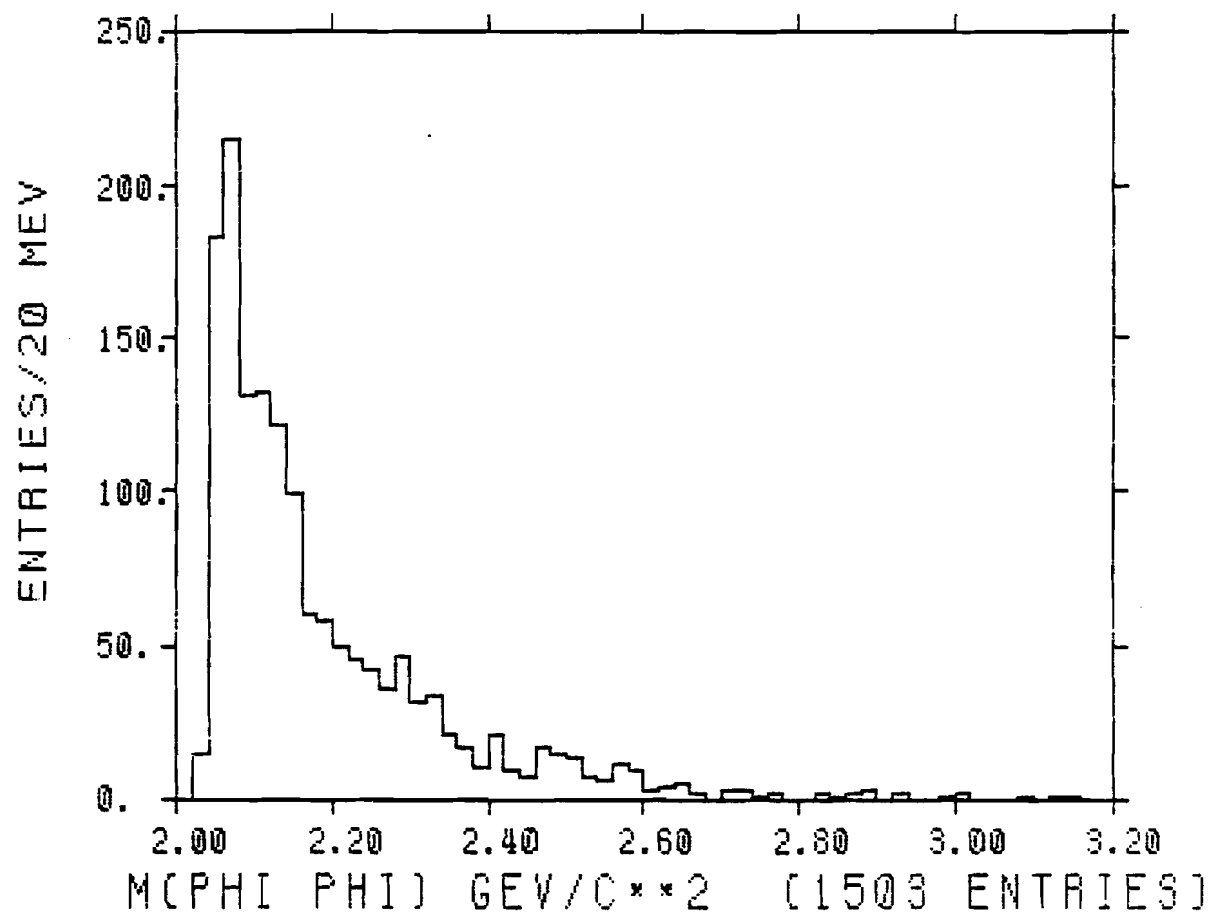


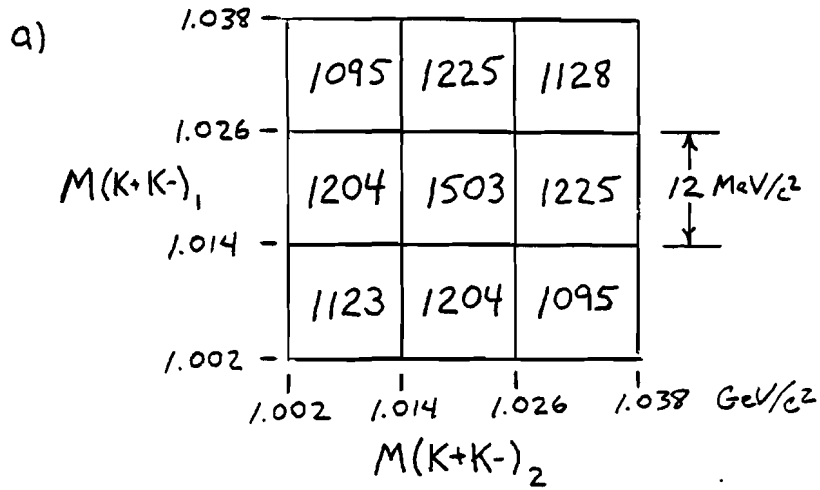
Fig. V.5 -  $\phi\phi$  invariant mass spectrum.

dimensional plot of  $M(K+K^-)_1$  vs.  $M(K+K^-)_2$ . In Figure V.6a one sees the number of entries in the scatter plot summed over 12 MeV by 12 MeV bins in the range 1.002 - 1.038 GeV. The central square is centered on the  $\phi$  mass for each axis.

We can estimate the background in the entire plot due to  $K+K-K+K^-$  production by looking at the four outside corners of the plot. Taking the average of these four squares and subtracting this from every square we have Figure V.6b.

Now we can subtract the contribution to the  $\phi\phi$  region from the two  $\phi K+K^-$  bands. Averaging the four middle squares on the outside and subtracting (the  $\phi\phi$  region has a double contribution) we have Figure V.6c. All the bins in the plot are zero, within errors, except for the  $\phi\phi$  bin which has a residual contribution above background of  $184 \pm 43$  events. This number will be used later in the cross section calculation for  $\phi\phi$  production.

If we take the events in the background regions and normalize them according to the above procedure, we can plot the estimated  $\phi\phi$  background spectrum, as seen in Figure V.7. This is shown as the cross hatched area superimposed on the  $\phi\phi$  spectrum in Figure V.8. We see that the residual events in the spectrum are mainly



b)

-15	115	18
94	393	115
13	94	-15

c)

-15	10	18
-10	184	10
13	-10	-15

Fig. V.6 - a) Scatter plot of  $M(K+K^-)_1$  versus  $M(K+K^-)_2$   
 b) After  $K+K-K+K^-$  background subtraction  
 c) After  $\phi K+K^-$  background subtraction.

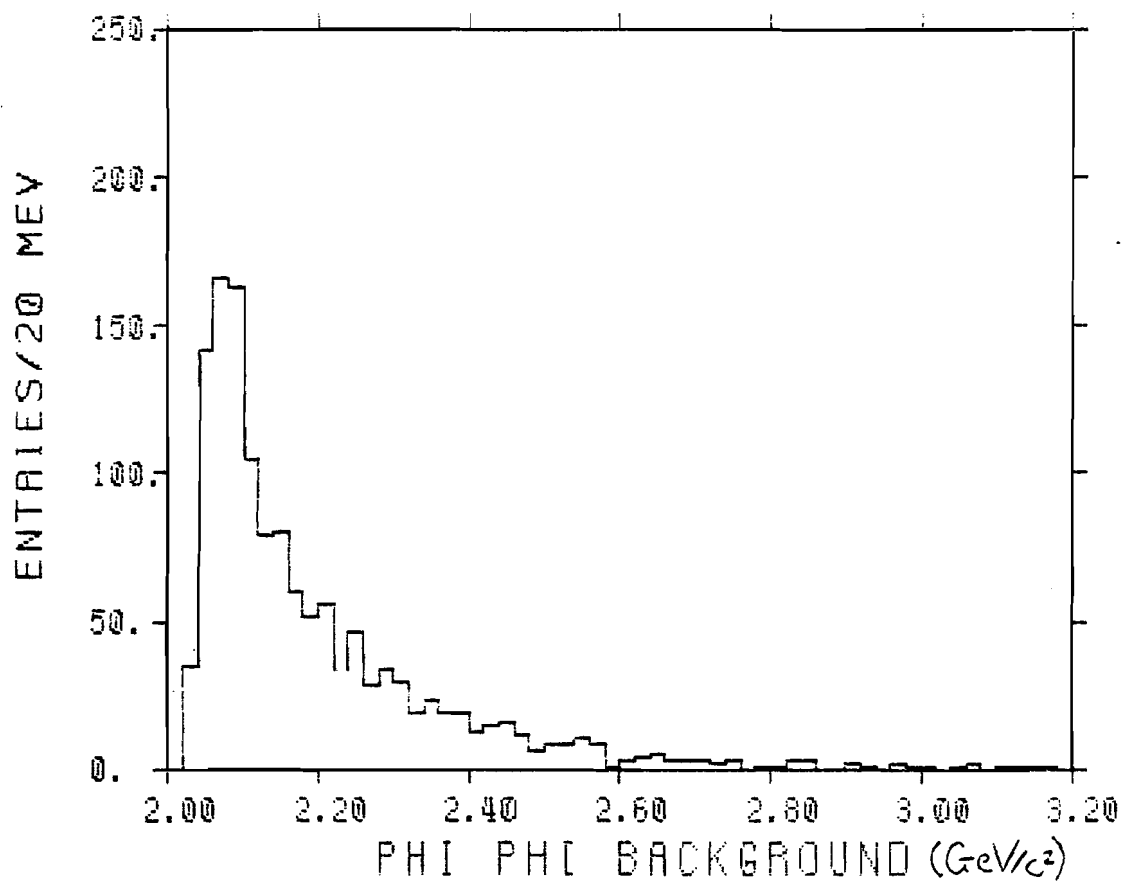


Fig. V.7 -  $\phi\phi$  background spectrum.

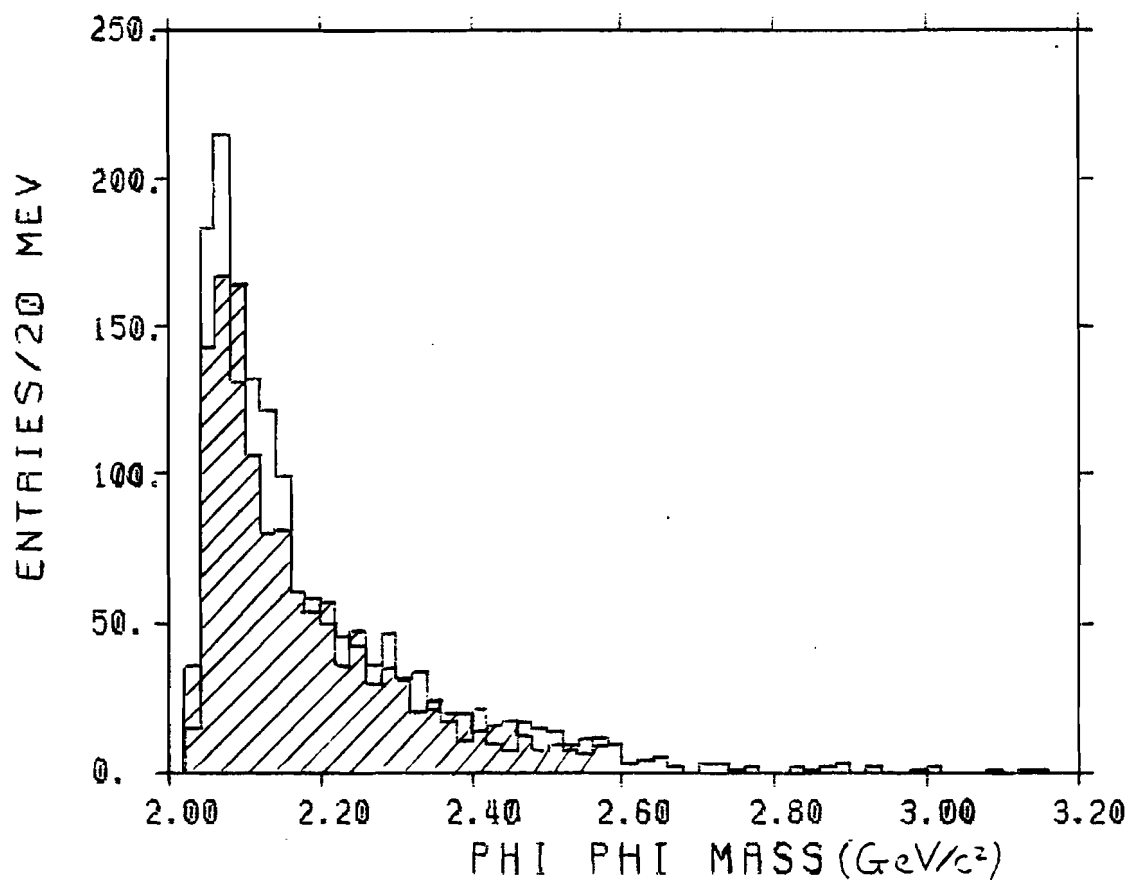


Fig. V.8 -  $\phi\phi$  invariant mass spectrum with background superimposed (cross hatched area).

concentrated in the six bins from 2.02 - 2.14 GeV.

The same basic procedure as outlined above was followed to find the number of  $\phi K+K^-$  events above the background due to  $K+K-K+K^-$  production. The number of background events was estimated by using 12 MeV side-bands on either side of the  $\phi K+K^-$  region over the entire scatter plot and normalizing to the same area. The number of  $\phi K+K^-$  events above background is found to be  $5448 \pm 251$ .

#### Acceptance and Cross Sections

For any scattering process the cross section for that process is simply a way to express the probability for that process to occur. The total cross section per nucleon,  $\sigma$ , can be defined as

$$\sigma = \frac{N_{\text{obs}}}{N_b N_t} \frac{W}{A}$$

where  $N_{\text{obs}}$  = the number of observed events,

$N_b$  = the number of incident beam particles,

$N_t$  = the number of nucleons/square cm,

$A$  = the acceptance (probability of detection),

$W$  = correction factors not included in  $A$ .

The relevant information about the beam and target is shown in Table V.1. The acceptance and correction factors will now be discussed in more detail.

#### Acceptance

TABLE V.1

Beam and Target Information

$$N_b = \text{Total live beam} = 8.70 \times 10^{10}$$

$$\begin{aligned} N_t &= \text{Number of target particles/cm}^2 \\ &= 6.02 \times 10^{23}/\text{g} \times 15.25\text{g/cm}^2 \\ &= 9.18 \times 10^{24}\text{cm}^{-2} \end{aligned}$$

$$\frac{1}{N_b N_t} = 1.252 \times 10^{-36}\text{cm}^2 = (800 \text{ events/nb})^{-1}$$



Since the detectors for E623 did not cover the entire  $4\pi$  solid angle, the first factor to be taken into account is the geometrical acceptance, which is a function of the positions, sizes and shapes of the detectors in the spectrometer system. It will also be a function of the kinematical variables of the system of interest. For example, if a  $\phi$  is produced with a large transverse momentum its decay products may not pass through the spectrometer magnet. Also, if a  $\phi$  is produced at high  $x_F$  ( $x_F = p_{\parallel}^*/p_{\parallel\text{max}}^*$ ) the kaons from the decay may have momenta above the  $C_B$  threshold and be unable to be identified as kaons.

The experimental apparatus for E623 was configured so that the region of acceptance for  $\phi\phi$  production as a function of  $x_F$  was confined to a rather narrow region ( $x_F < 0.1$ ) centered about  $x_F = 0$ . This was done because, for nucleon-nucleon interactions, the production of glueballs, the  $\eta_c$  and massive  $s\bar{s}$  states is expected to take place primarily in the central region,  $x_F \approx 0$  ([Afe 80a], [Ein 75], [Sha 84]). The experimental  $x_F$  distribution for all  $K^+K^-K^+K^-$  combinations is shown in Figure V.9.

The most important factors in determining the limited range of  $x_F$  are the geometrical factors imposed by the spectrometer system and the momentum window for

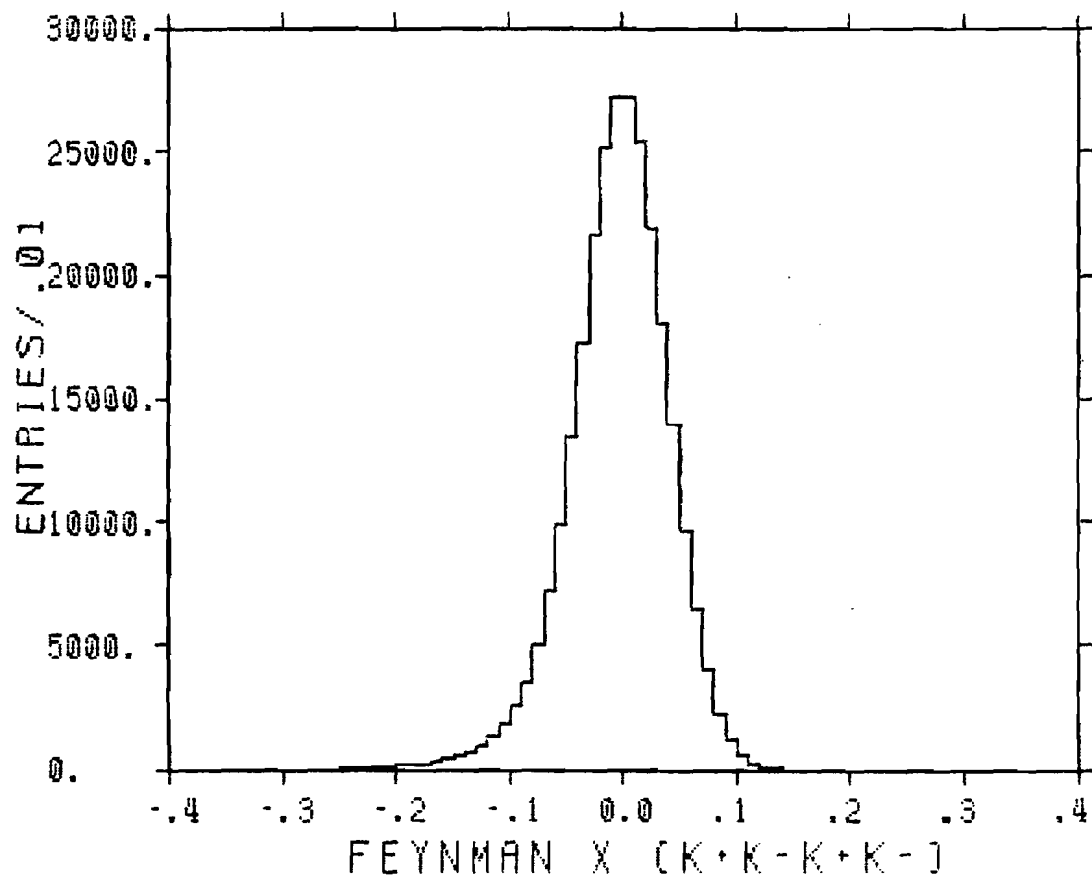


Fig. V.9 - Feynman x ( $x_F$ ) distribution for all  $K^+K^-K^+K^-$  combinations.

kaon identification imposed by the Cerenkov counter  $C_B$ . This information was used in a Monte Carlo program to calculate the E623 relative acceptance.

The program generated particles of mass  $M$  and a given  $x_F$  in the nucleon-nucleon center of momentum and allowed them to decay to  $\phi\phi$  and then each  $\phi$  to  $K+K^-$ . The massive state was also given a small transverse momentum according to an exponential distribution with  $\langle p_T \rangle \approx 300 \text{ MeV}/c$ . The angular distributions for all decays were assumed to be isotropic. The kaons were transformed back to the lab frame and then tracked through the spectrometer system. The ratio of the number of Monte Carlo events with all four kaons in the  $C_B$  momentum range and passing through the spectrometer, divided by the number of generated events was defined as the relative acceptance.

For  $M(\phi\phi) = M(\eta_c)$ , the relative acceptance as a function of  $x_F$  is shown in Figure V.10. The relative acceptance as a function of  $\phi\phi$  invariant mass for three values of  $x_F$  is shown in Figure V.11. It is evident that, for  $x_F \approx 0$ , the acceptance is reasonably flat over a wide range of  $\phi\phi$  invariant masses.

The same Monte Carlo program was also used to determine the experimental resolution for observing a narrow state decaying to  $\phi\phi$  as a function of mass.

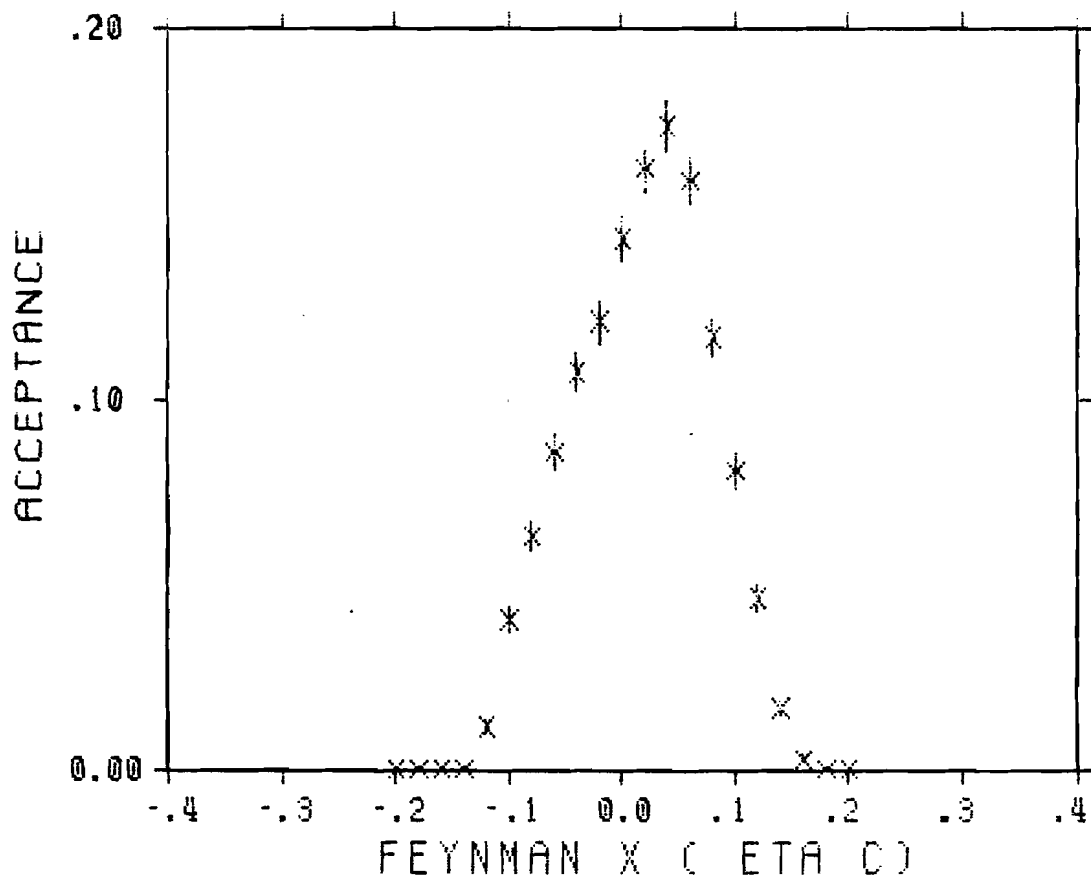


Fig. V.10 - Monte Carlo generated acceptance versus  $x_F$  for  $M(\phi\phi) = M(\eta_c)$ .

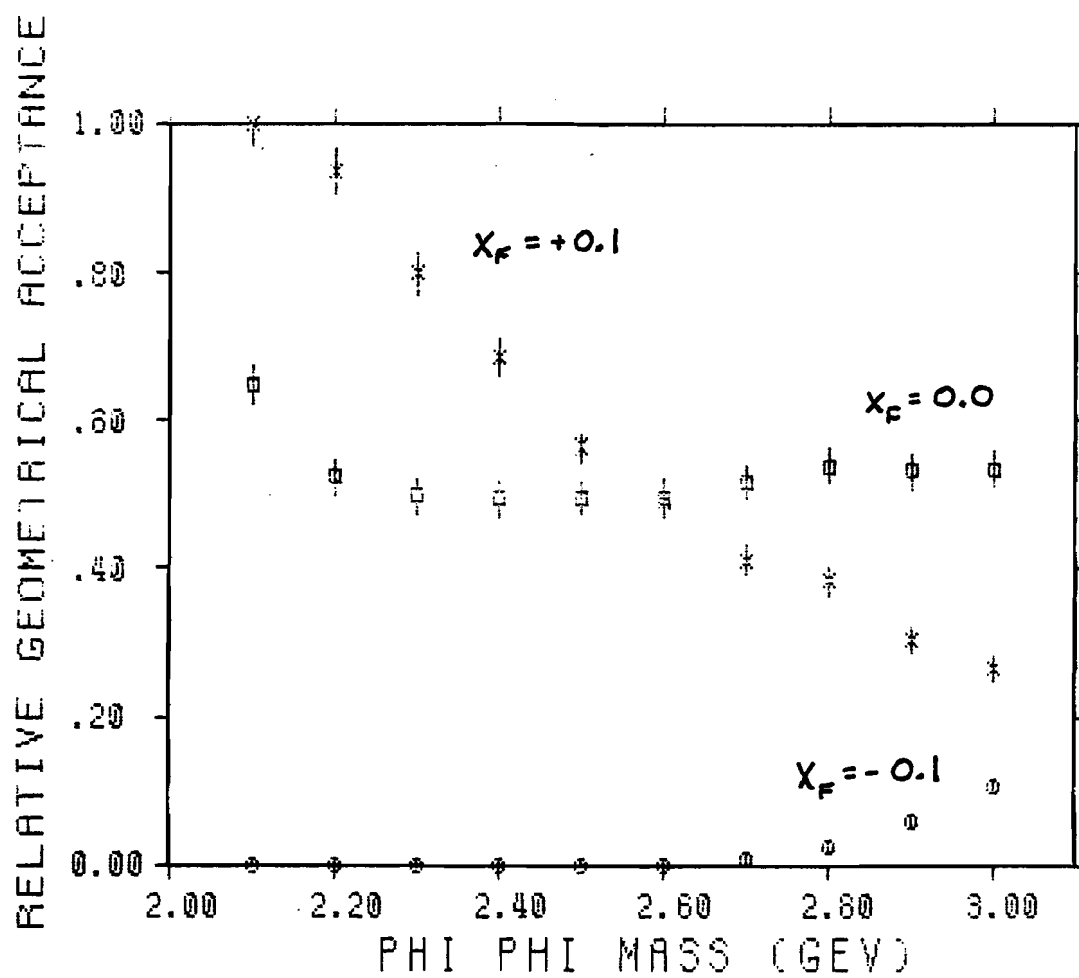


Fig. V.11 - Monte Carlo generated acceptance versus  $\phi\phi$  invariant mass for  $x_F = -.1, 0., .1$ .

Using Monte Carlo generated  $\phi\phi$  events having a natural  $\phi$  width of 4 MeV, the momenta of the decay tracks were changed slightly to simulate measurement errors. The amount of change in the momentum was given a Gaussian distribution about zero and the variance of the distribution was adjusted to reproduce the fitted  $\phi$  width (FWHM) of approximately 9 MeV. The estimated  $K+K^-$  mass resolution as a function of mass is shown in Figure V.12. The two sets of points correspond to variances giving reconstructed  $\phi$  widths of 8 and 10 MeV.

If the tracks from an event pass through the spectrometer we must also consider detector inefficiencies and finite detector resolution. The wire chambers and detectors are not 100% efficient so that some particles that pass through the detectors will not give signals. Also, since the wire chambers have a finite wire spacing, hodoscope elements have a finite width and mirrors in  $C_B$  have a finite size, there will occasionally be overlapping tracks that may be unable to be identified.

Another factor in the acceptance will be trigger efficiency. Even if all the particles pass through the system and are detected by the trigger chambers and counters, they may be in such a configuration that the trigger processor does not recognize it as valid.

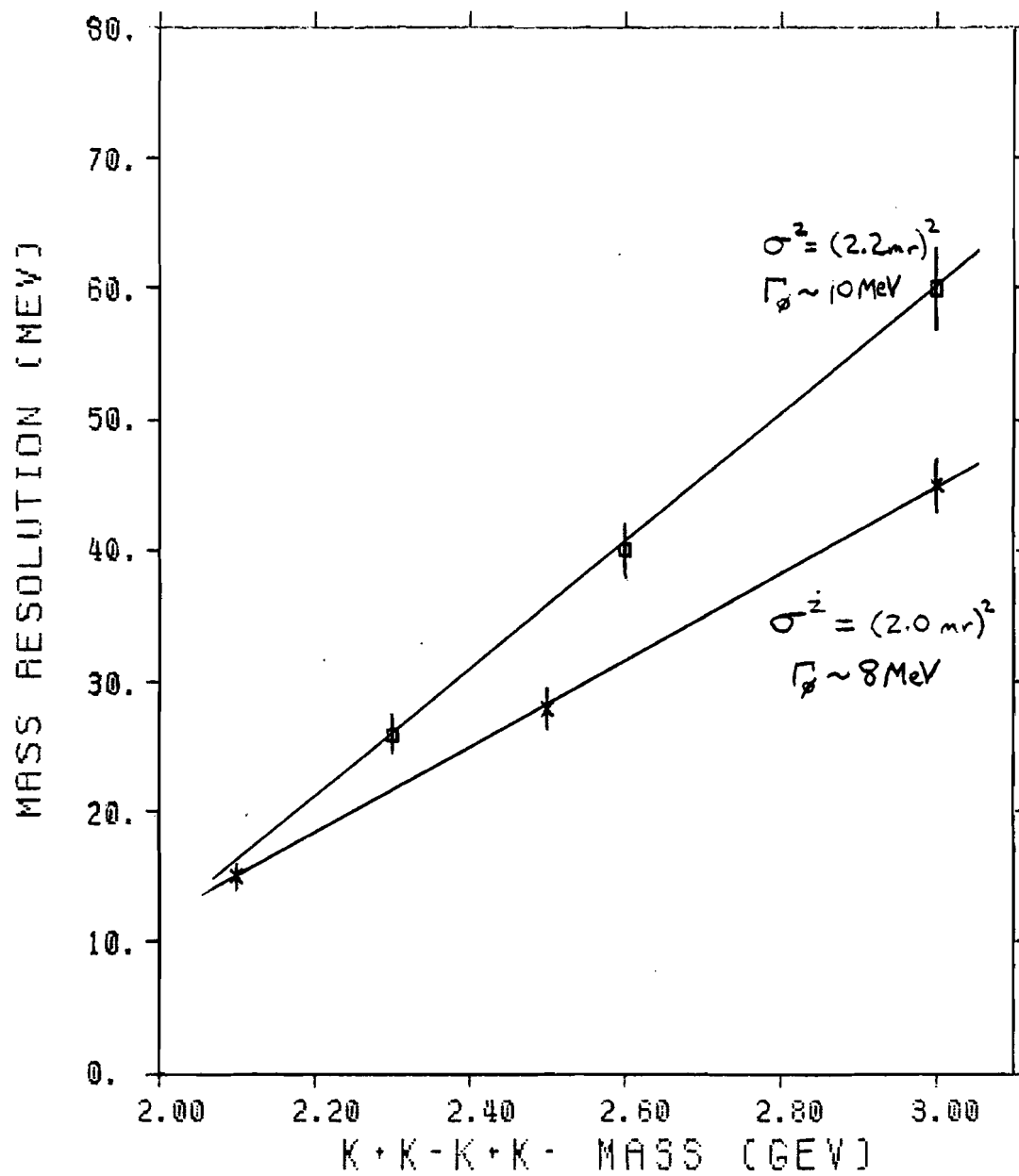


Fig. V.12 - E623 estimated mass resolution versus K+K-K+K- invariant mass.

Finally, assuming we have actually triggered on a good event and stored it on tape, we must consider the pattern recognition and particle identification efficiency. This includes the efficiency for reconstructing the actual tracks from the wire chamber and detector information for that event and the efficiency for identifying the different types of particles from the Cerenkov counter information.

Other factors that will contribute to the acceptance and the correction factor,  $W$ , will be multiple scattering caused by the detectors, probability of kaons decaying in flight before being detected, and the branching ratio for a  $\phi$  to decay into  $K^+K^-$  (.493).

#### Acceptance Calculation

Since the actual production distributions for  $\phi\phi$  are unknown, some type of model must be used to calculate the acceptance. For E623 the Lund Monte Carlo model [Sjo 83] was used to generate typical, unbiased hadronic events.

In the Lund model for low- $p_T$  inelastic hadronic interactions the incoming hadrons in the scattering process are viewed as color bags, each containing two or three color blobs (mesons or baryons respectively). These color blobs correspond to the smeared out valence quark wavefunctions in the hadrons. There will then be



some probability for two of the blobs to make a connection so that the two hadron bags do not separate after the collision but instead stretch out a color string between them and the other valence quarks. When the string becomes sufficiently elongated it will break giving rise to a  $q\bar{q}'$  pair. This may happen at several points along the string and these will combine with other quarks and antiquarks to produce the final state hadrons.

The FORTRAN program corresponding to the Lund model was used to generate a sample of events and a count was kept of the number of events generated as  $1\phi$ ,  $2\phi$ ,  $\phi K+K^-$  and so on. From this sample, only those events having at least one  $\phi$  decaying to  $K+K^-$  with both kaons in the Cerenkov momentum range ( $5.7 < p_K < 23.0$ ) were kept for the rest of the analysis.

The four-vectors from the generated events were then used as input to another Monte Carlo program that simulated the Fermilab MPS. The MPS simulation program propagated the particles through the spectrometer system, creating hits in the wire chambers and pulse heights in the ADCs from the scintillators and Cerenkovs. Realistic efficiencies and resolutions, estimated from E623 data, were used to describe all detectors. Multiple scattering effects from material in

the apparatus were also included. The generated information from the detectors was then used by a trigger processor simulation program and those events that satisfied the trigger criteria were flagged. The output of the MPS simulation program was written to tape in the same format as the raw data tapes from the experimental run.

The Monte Carlo raw data tapes were then processed by the same programs that were used for the actual data analysis and described in Chapter IV.

For the  $\phi\phi$  and  $\phi K+K^-$  total cross sections respectively, the acceptance was defined as the number of  $\phi\phi$  and  $\phi K+K^-$  events found by the processing programs divided by the total number of generated Monte Carlo events of that type. A correction factor,  $W$ , of 1.61 was also required for both the  $\phi\phi$  and  $\phi K+K^-$  cross sections to account for the probability of any of the four charged kaons decaying in flight before reaching the Cerenkov counter  $C_B$ . Table V.2 shows the numbers used for the acceptance and cross section calculations.

The calculated value for the total inclusive  $\phi\phi$  cross section at 400 GeV/c is  $0.87 \pm 0.27 \mu\text{b}$  and the total inclusive  $\phi K+K^-$  cross section is  $23.6 \pm 2.7 \mu\text{b}$ .

At the  $\eta_c$  mass we can estimate that it would have required approximately six events over a background of

TABLE V.2

Numbers Used for Acceptance and Cross Section Calculation

	<u><math>\phi\phi</math></u>	<u><math>\phi K+K-</math></u>
Total number of generated Monte Carlo events	56433	193969
Total number of Monte Carlo events passing all cuts	$24 \pm 4.9$	$90 \pm 9.5$
Acceptance (%)	$0.042 \pm 0.009$	$0.046 \pm 0.005$
Correction factor for kaon decay (W)	1.61	1.61
$N_b N_t$ (events/nb)	800	800
Total number of observed events above background	$184 \pm 43$	$5448 \pm 251$
Cross section ( $\mu b$ )	$0.87 \pm 0.27$	$23.6 \pm 2.7$

three events in three 20 MeV bins to observe the  $\eta_c$  at the 99.7% confidence level. Assuming that the acceptance for detecting the  $\eta_c$  is the same as for  $\phi\phi$  and using the calculated sensitivity of approximately 5 nb per observed event, we arrive at an upper limit for

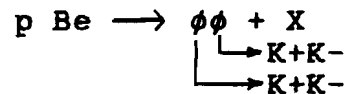
$$\sigma_T(pN \rightarrow \eta_c + X) \cdot BR(\eta_c \rightarrow \phi\phi) \leq 30 \text{ nb.}$$

Using the measured  $\eta_c$  branching ratio [Bal 84] into  $\phi\phi$  of  $(8.0 \pm 2.5 \pm 2.0) \times 10^{-3}$  we have

$$\sigma_T(pN \rightarrow \eta_c + X) \leq 3.75 \text{ } \mu\text{b.}$$

#### Other Experimental Results on $\phi\phi$ Production

The first data on inclusive  $\phi\phi$  production came from Fermilab in 1981 [Yam 81]. A double-arm spectrometer system was used to look at the reaction



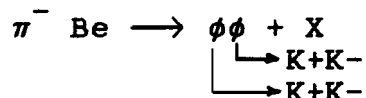
at 350 GeV/c incident momentum. A total of 3  $\phi\phi$  events were observed and at the 90% confidence level an upper limit of 330 nb/nucleon was set on

$$\left. \frac{d\sigma}{dy} (p \text{ Be} \rightarrow \eta_c + X) \right|_{y=0} \times BR(\eta_c \rightarrow \phi\phi)$$

If a  $(1-x_F)^2$  distribution is assumed this corresponds to an upper limit of 880 nb/nucleon on the total cross section times branching ratio into  $\phi\phi$  for  $\eta_c$  production [Jon 82].

The ACCMOR collaboration [Dau 81] using

experimental set-up NAl1 at the CERN-SPS studied the reaction



at 100 and 175 GeV/c incident momentum. The  $\phi\phi$  mass spectrum and acceptance for the 100 GeV/c data is shown in Figure V.13. After background subtraction they observed  $25 \pm 8$   $\phi\phi$  events and from this calculated a total cross section times branching ratio

$$\sigma_X^{\text{tot}} \times \text{BR}(X \rightarrow \phi\phi) = 0.34 \pm 0.12 \mu\text{b}.$$

The 175 GeV/c ACCMOR data is shown in Figure V.14. There were  $112 \pm 17$   $\phi\phi$  events above background. No evidence for the  $\eta_c$  was found and the upper limit for the  $\eta_c$  cross section times branching ratio was established to be

$$\sigma_T(\pi^- \text{ Be} \rightarrow \eta_c + X) \times \text{BR}(\eta_c \rightarrow \phi\phi) \leq 72 \text{ nb/nucleon}$$

at the 90% confidence level.

The ACCMOR collaboration also took more data at 100 GeV/c in 1982 using the same apparatus but with a slightly modified trigger and with  $\pi^-$ ,  $K^-$  and  $\bar{p}$  beams [Bai 83]. The  $\phi\phi$  invariant mass spectrum for the different beams is shown in Figure V.15. They reported no evidence for narrow enhancements in the  $\phi\phi$  channel and no cross sections were given due to normalization problems.

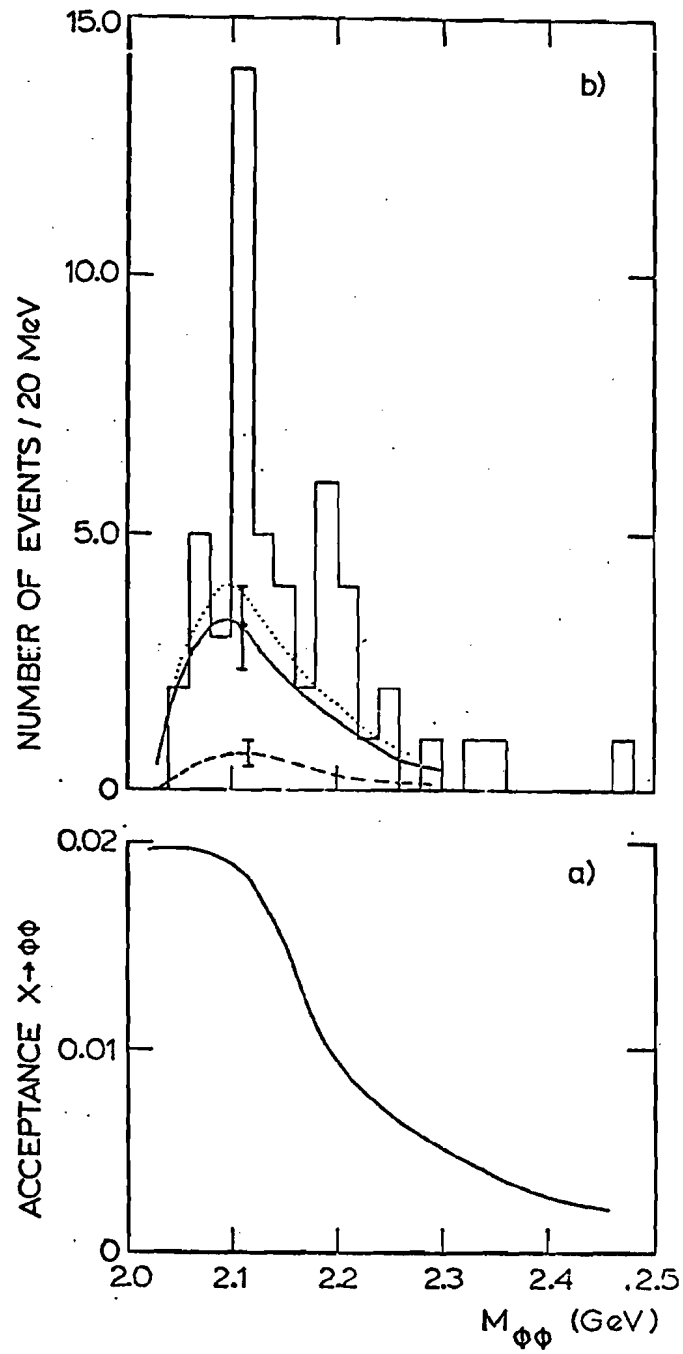


Fig. V.13 -  $\phi\phi$  invariant mass spectrum and acceptance for 100 GeV/c data [Dau 81].

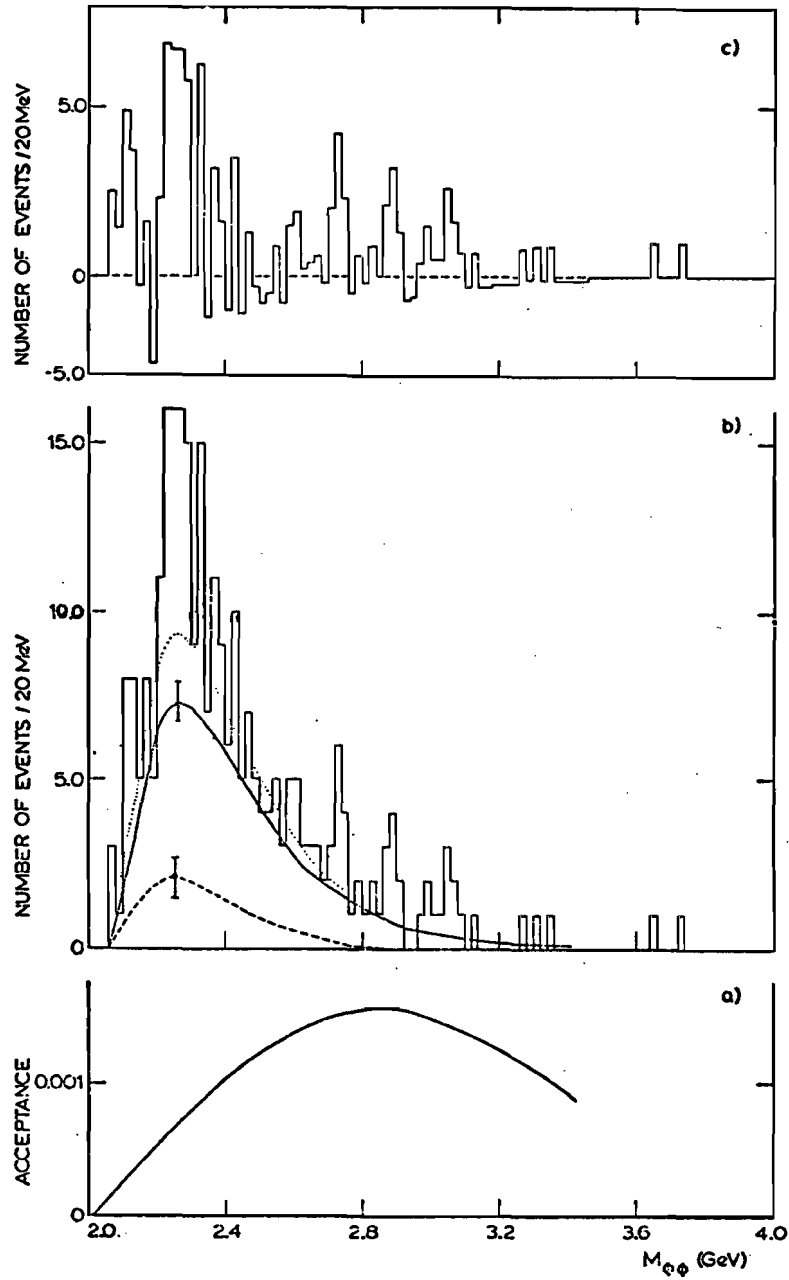


Fig. V.14 -  $\phi\phi$  invariant mass spectrum, background subtracted spectrum and acceptance for 175 GeV/c data [Dau 81].

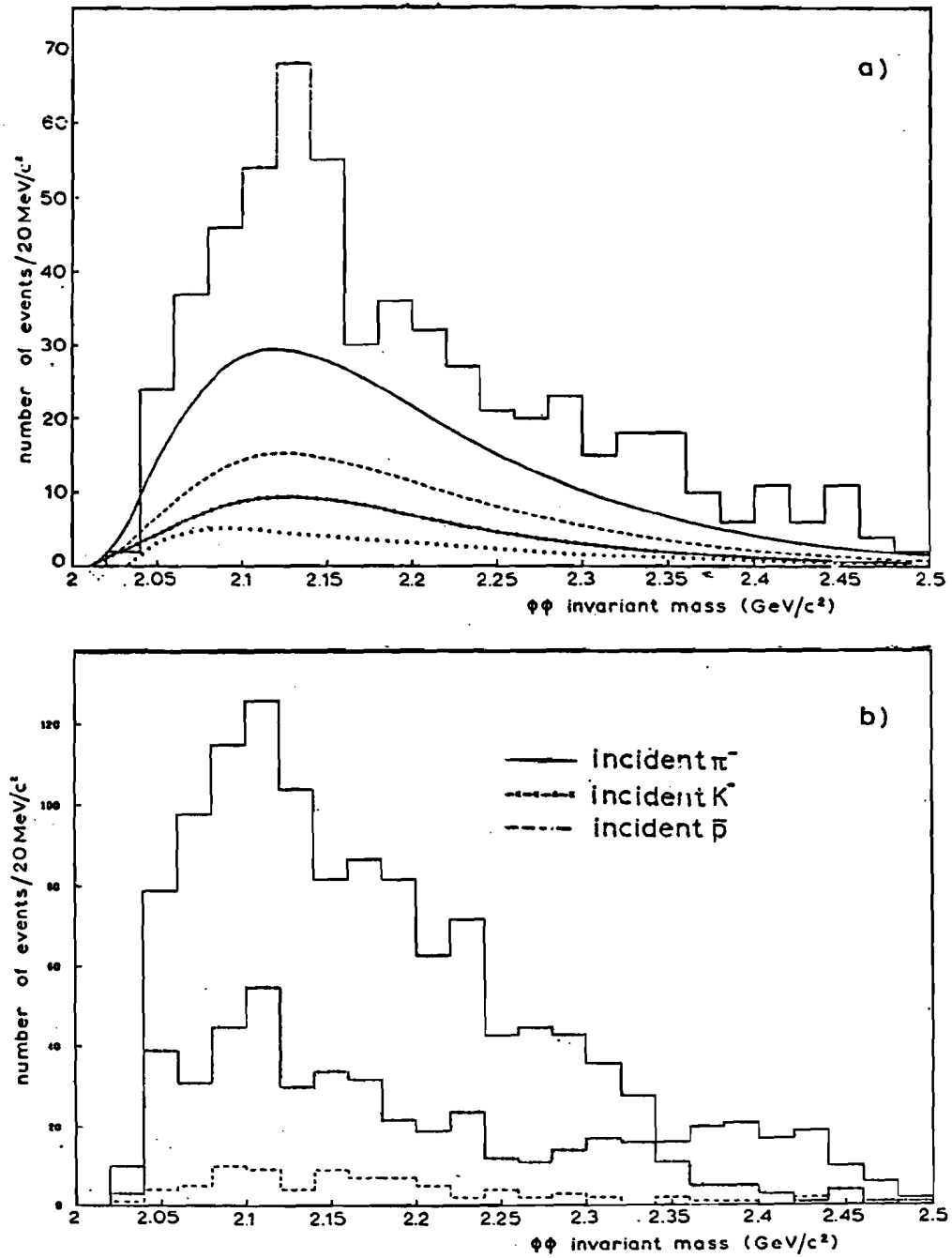
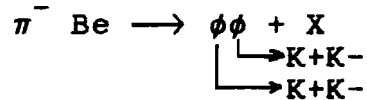


Fig. V.15 -  $\phi\phi$  invariant mass spectrum a) 1981  
 100 GeV/c data b) 1982 100 GeV/c data  
 [Bai 83].



The most recent data on inclusive  $\phi\phi$  production from other experiments has been reported by Booth et al. [Boo 84] using the  $\Omega'$  spectrometer in experiment WA67 at the CERN-SPS. The reaction studied was



at 85 GeV/c. The  $\phi\phi$  invariant mass spectrum and background subtracted  $\phi\phi$  spectrum are shown in Figure V.16. They reported no evidence nor narrow enhancements. Using their sample of  $4327 \pm 100$   $\phi\phi$  events they place upper limits at the 99.7% confidence level of

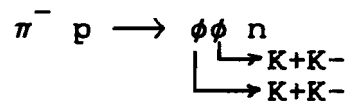
$$\sigma_T(X) \cdot \text{BR}(X \rightarrow \phi\phi) \leq 62 \text{ nb/nucleon at } M_X = 2.1 \text{ GeV}$$

and

$$\sigma_T(X) \cdot \text{BR}(X \rightarrow \phi\phi) \leq 26 \text{ nb/nucleon at } M_X = 3.0 \text{ GeV.}$$

A summary of some of the cross sections and upper limits from this and other inclusive  $\phi\phi$  experiments is shown in Table V.3.

The only experiment to date that has reported evidence for resonances in the  $\phi\phi$  channel has been the BNL/CCNY experiment at the Brookhaven MPS ([Etk 82], [Lin 83]). They have studied the exclusive reaction



at 22.6 GeV/c, and report evidence for three wide  $\phi\phi$

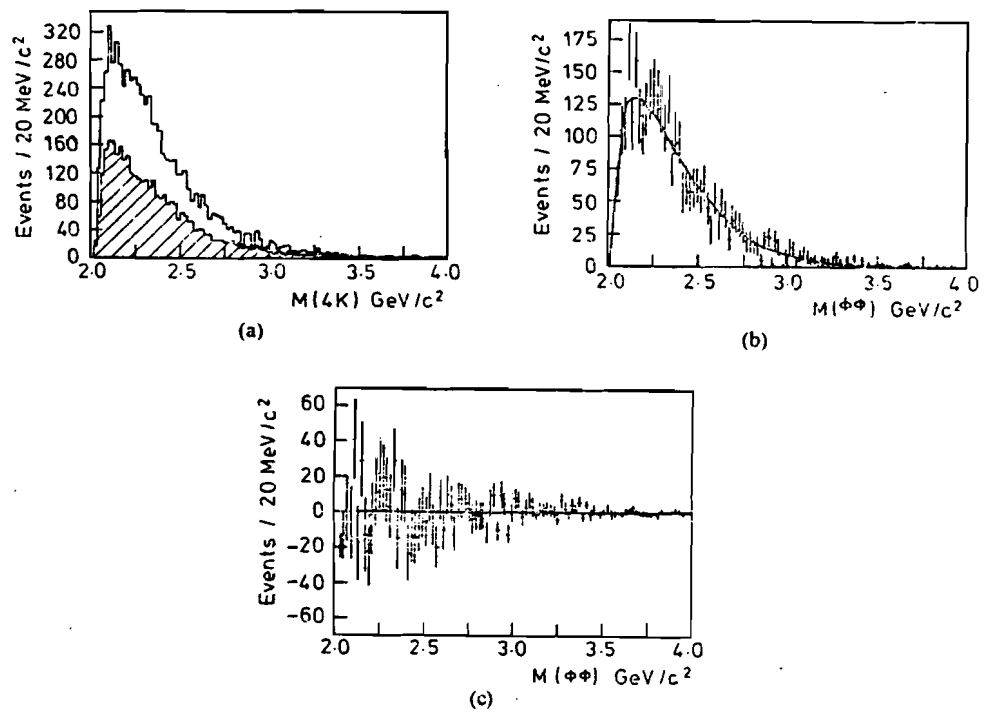


Fig. V.16 - a)  $\phi\phi$  invariant mass spectrum  
 b) Background subtracted spectrum  
 c) Residuals from fit to background subtracted spectrum [Boo 84].

TABLE V.3

Summary of Cross Sections and Upper Limits  
for Inclusive  $\phi\phi$  Production

Experiment	Result
[Yam 81]	
p Be $\rightarrow \eta_c + X$	$\frac{d\sigma}{dy} \Big _{y=0} \cdot \text{BR}(\eta_c \rightarrow \phi\phi) \leq 330 \text{ nb}$
350 GeV/c	90% C.L.
[Dau 81]	
$\pi^-$ Be $\rightarrow \phi\phi + X$	
100 GeV/c	$\sigma_T(\phi\phi + X) = 0.34 \pm 0.12 \mu\text{b}$
175 GeV/c	$\sigma_T(\eta_c + X) \cdot \text{BR} \leq 72 \text{ nb}$
	90% C.L.
[Boo 82]	
$\pi^-$ Be $\rightarrow \phi\phi + X$	$\sigma_T(X) \cdot \text{BR}(X \rightarrow \phi\phi) \leq 62 \text{ nb}$
85 GeV/c	$M_X = 2.1 \text{ GeV}/c^2 \quad 99.7\% \text{ C.L.}$
	$\sigma_T(X) \cdot \text{BR}(X \rightarrow \phi\phi) \leq 26 \text{ nb}$
	$M_X = 3.0 \text{ GeV}/c^2 \quad 99.7\% \text{ C.L.}$
E623	
p N $\rightarrow \phi\phi + X$	$\sigma_T(\phi\phi + X) = 0.87 \pm 0.27 \mu\text{b}$
400 GeV/c	$\sigma_T(\eta_c + X) \cdot \text{BR} \leq 30 \text{ nb}$
	99.7% C.L.

resonances from a partial wave analysis of their data. The  $\phi\phi$  mass spectrum, corrected for acceptance, is shown in Figure V.17. The partial wave decomposition of this spectrum is shown in Figure V.18 and the masses and widths of the three reported states are seen in Table V.4. Lindenbaum [Lin 83] has claimed that these states constitute the first observation of glueballs but this conclusion has been criticized by others ([Lip 83], [Gom 84]). This criticism is based on Lindenbaum's assertion that the reaction  $\pi^- p \rightarrow \phi\phi n$ , should be strongly suppressed by the OZI rule. Lipkin and Gomm both argue that this interpretation is incorrect and that  $\phi\phi$  production in this reaction is not necessarily suppressed nor indicative of glueball production.

#### Comparison with Theory

The measured inclusive  $\phi\phi$  total cross section can be compared with a recent theoretical prediction given by Li and Liu [Li 83]. They use a Drell-Yan type mechanism with gluon fusion to produce a  $2^{++} s\bar{s}s\bar{s}$  state having a mass of  $2.16 \text{ GeV}/c^2$  and a width of approximately 315 MeV. A  $2^{++} s\bar{s}s\bar{s}$  state at  $2.25 \text{ GeV}/c^2$  with a width of 360 MeV decaying predominantly to  $\phi\phi$  has been predicted according to the bag model calculation of Jaffe [Jaf 77]. Li and Liu assume that the  $2^{++}$  state at  $2.16 \text{ GeV}/c^2$  observed by Etkin et al. [Etk 82] is the

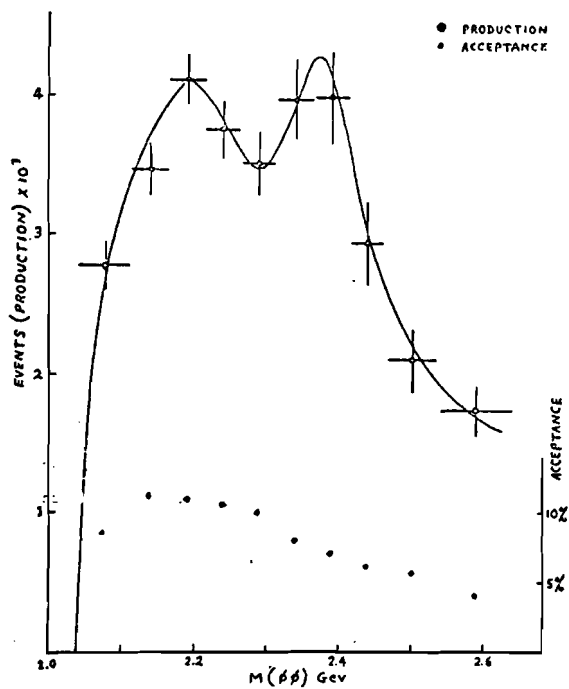


Fig. V.17 -  $\phi\phi$  invariant mass spectrum corrected for acceptance [Lin 83].

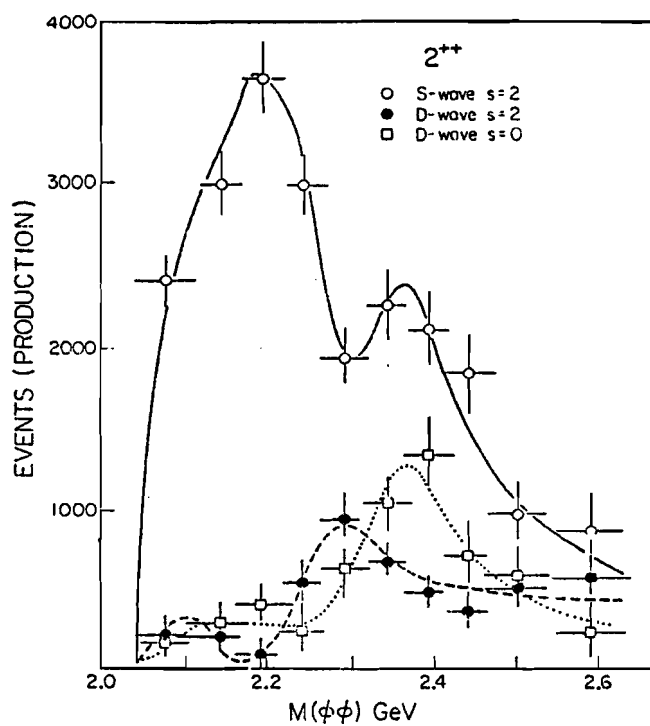


Fig. V.18 - Partial wave decomposition of  $\phi\phi$  spectrum [Lin 83].

TABLE V.4

BNL/CCNY  $g_T$  States (from [Hit 84])

<u>State</u>	<u><math>I^G</math></u>	<u><math>J^{PC}</math></u>	<u>Mass (MeV)</u>	<u><math>\Gamma</math> (MeV)</u>
$g_T(2120)$	$0^+$	$2^{++}$	2120	300
$g_T(2220)$	$0^+$	$2^{++}$	2220	200
$g_T(2360)$	$0^+$	$2^{++}$	2360	200

state predicted by Jaffe and use the measured mass and width in their calculation.

Their predictions for the  $\phi\phi$  total cross section in  $\pi p$  and  $pp$  interactions versus  $s$ , are shown in Figure V.19 along with the data from E623 and ACCMOR [Dau 81]. Both experimental points are above the theoretical curves by a factor of about 1.5 to 2.0, but given the uncertainties of the model the agreement is reasonable.

The various upper limits for  $\eta_c$  production given previously can be compared with the theoretical predictions for the  $\eta_c$  cross section using the gluon fusion model of Einhorn and Ellis [Ein 76] discussed in Chapter II. The gluon distribution functions used in this case are those given by Duke and Owens ([Duk 84],[Owe 84]) for pions and nucleons.

Figure V.20 shows the experimental upper limits corrected for the  $\eta_c$  branching ratio into  $\phi\phi$ , along with the theoretical curves for  $\pi p$  and  $pp$  interactions. The upper limit for E623 at  $3.75 \mu b$  is still about a factor of four above the predicted value.

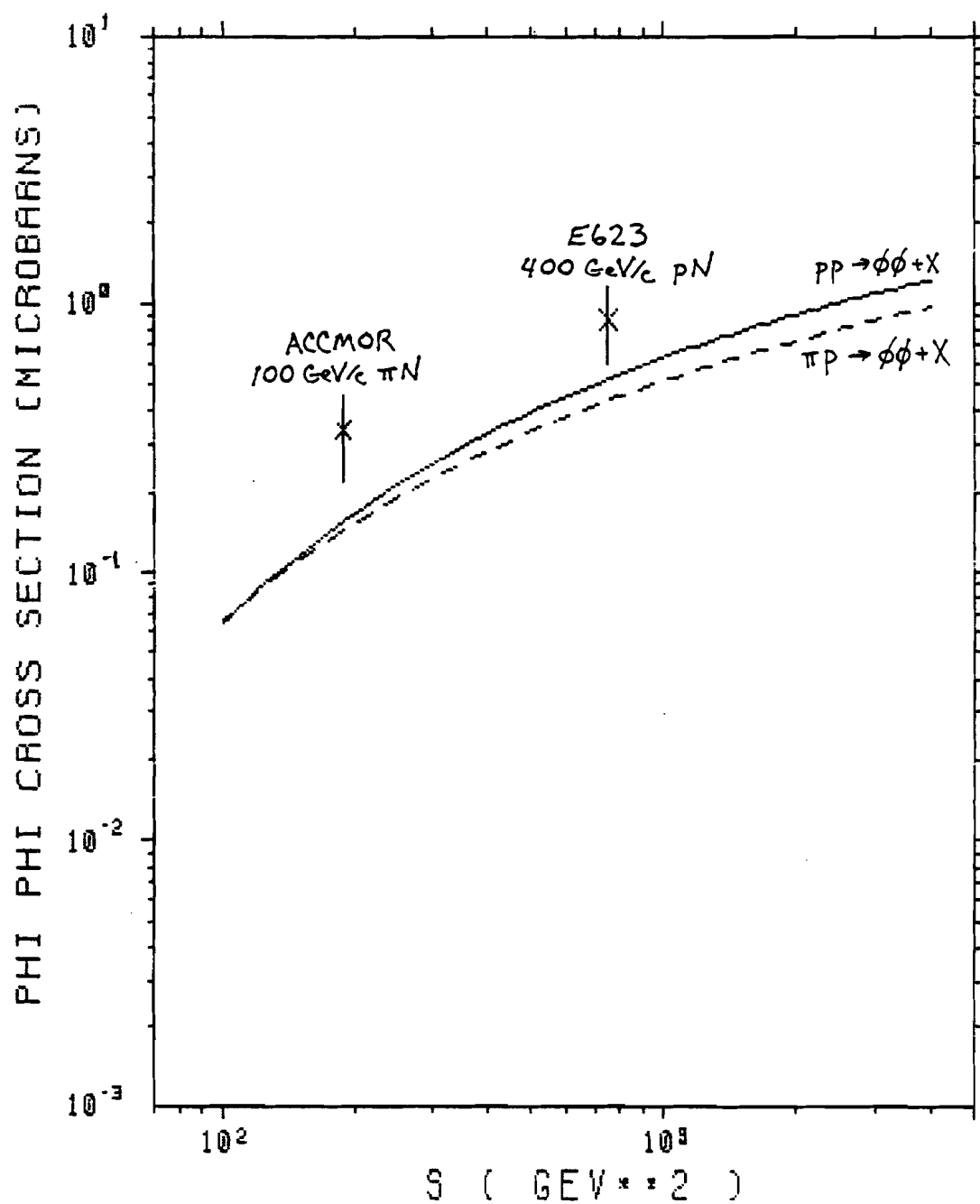


Fig. V.19 -  $\phi\phi$  total cross section versus  $s$ , using model of Li and Liu. Data points from E623 and ACCMOR are shown.



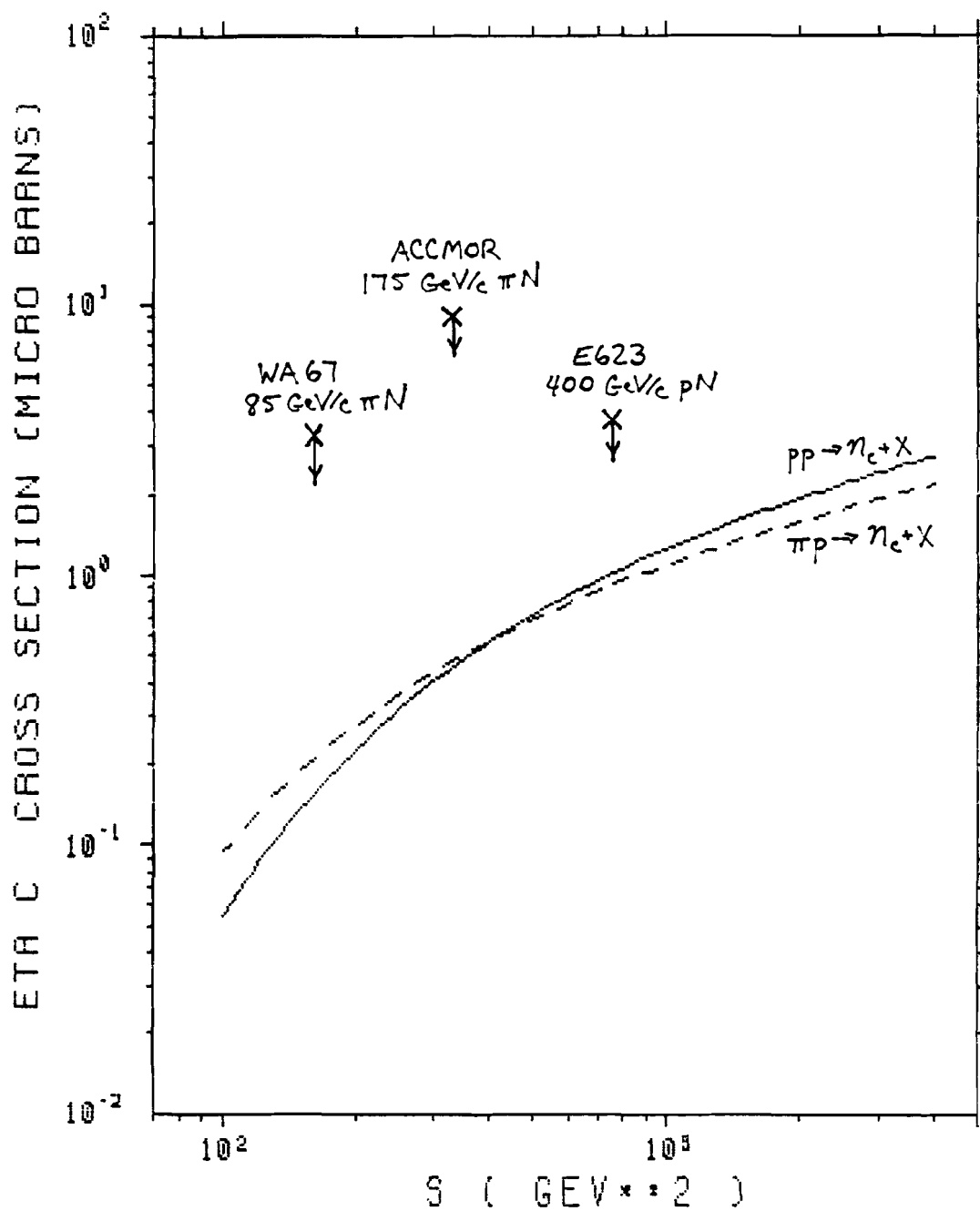


Fig. V.20 - Experimental upper limits for  $\eta_c$  cross section and theoretical predictions using model of Einhorn and Ellis with gluon distribution functions of Duke and Owens.

## Chapter VI

### SUMMARY AND CONCLUSIONS

In this thesis, results have been presented from Fermilab Experiment 623, a particle search using the Fermilab MPS with a 400 GeV/c proton beam incident on a segmented scintillator target to study the reaction

$$p N \longrightarrow \phi\phi + X$$

where each  $\phi$  decayed into a  $K^+K^-$  pair.

The apparatus was triggered using a sophisticated trigger processor that used pre-defined roads through wire chamber hodoscopes and a multicell threshold Cerenkov counter to identify candidate kaon tracks. The processor selected events having at least two  $K^+$  and two  $K^-$  candidates and further required that each  $K^+K^-$  pair have low invariant mass in order to preferentially select events consistent with production of  $\phi$  meson pairs. The time required for the processor to reach a decision was approximately 200 ns after latching the input signals.

A total of  $3.0 \times 10^6$  triggers were recorded for analysis and after pattern recognition, track fitting and particle identification, there were 123,507 events

having at least two identified  $K^+$  and two identified  $K^-$  tracks in the momentum range,  $5.8 < p < 23.0$  GeV/c.

The invariant mass distributions for  $K^+K^-K^+K^-$ ,  $\phi K^+K^-$  and  $\phi\phi$  combinations were examined but no evidence was seen for production of new, narrow resonances. A background subtraction was performed for the  $\phi K^+K^-$  and  $\phi\phi$  spectra; giving  $5448 \pm 251$  and  $184 \pm 43$  events above background respectively.

Using the Lund Monte Carlo model to simulate production of uncorrelated  $\phi K^+K^-$  and  $\phi\phi$  events, and another Monte Carlo program to simulate the MPS and trigger processor, we have calculated our acceptance and calculated total cross sections for inclusive  $\phi K^+K^-$  and  $\phi\phi$  production at 400 GeV/c. We find that

$$\sigma_T(pN \rightarrow \phi K^+K^- + X) = 23.6 \pm 2.7 \text{ } \mu\text{b/nucleon}$$

and

$$\sigma_T(pN \rightarrow \phi\phi + X) = 0.87 \pm 0.27 \text{ } \mu\text{b/nucleon}.$$

We also have set an upper limit on inclusive  $\eta_c$  production at 400 GeV/c and, after correcting for the branching ratio into  $\phi\phi$ , find that

$$\sigma_T(pN \rightarrow \eta_c + X) < 3.75 \text{ } \mu\text{b/nucleon}$$

at the 99.7% confidence level.

#### Final Comments and Suggestions

During the test run of 1981, we took about 20,000 triggers and 32 events consistent with  $\phi\phi$  production

were found [Gre 81]. From this, it was concluded that in a 500 hour data run we would expect about 16,000  $\phi\phi$  events. Since we only observed approximately 1500  $\phi\phi$  events, it is reasonable to ask why E623 did not achieve all that had been expected.

One significant factor is that we actually received only about one fourth of the amount of running time that we had requested. This changes the number of expected  $\phi\phi$  events to about 4000, but still leaves a discrepancy of about a factor of three in the number of observed events. Whether this discrepancy is due to a slightly over-optimistic prediction from the test data or due to some unforeseen flaw in the design of the experiment is rather difficult to say. However, some problems noted in analyzing the data can be presented along with suggestions on how the experiment could have been improved.

During the pattern recognition phase of the analysis, it was noted that more y-chambers downstream of the magnet would have helped in matching the chamber hits with the tracks. Due to the replacement of the spark chambers, used in the test run, by the new drift chambers constructed for E623, some amount of redundancy in the y-view was lost. However, the replacement of the spark chambers was necessary in order to take data at a

higher rate.

Obviously, particle identification was a very important part of E623 and the Cerenkov counter  $C_B$  was the main element of that analysis. It appears that  $C_B$  worked about as well as could be expected, giving on the average about six photoelectrons for a  $\beta=1$  particle. One simple improvement though, would have been to put scintillator behind every mirror of  $C_B$  in order to give a positive signal for every charged particle, pion or kaon, that passed through the cell. This would also have helped to veto tracks generated by pattern recognition errors in the off-line analysis.

However, the scintillator would not have helped remove the background due to the many pions with momenta just above the  $C_B$  threshold that gave no light because of the statistical nature of the process. One possible solution to this problem, and that used by some other experiments, would have been to have two separate Cerenkov counters downstream of the magnet, with different thresholds, in order to give some range of momenta in which kaons could be identified unambiguously.

One other problem might have been that we should have limited the charged multiplicity more stringently, in order to give the trigger processor a greater chance

of finding the tracks correctly on-line, and the pattern recognition a better chance off-line. Also, it may have been that when the trigger processor was designed, not enough extra pion tracks were included in the Monte Carlo tests. This would have tended to make the processor trigger on uninteresting events more often than it should have, due to being overwhelmed by too many tracks.

Finally, however, it should be noted that we were able to successfully use a fast, high-level trigger processor to search for events containing two  $\phi$  mesons. This type of processor system is becoming very common in new high-energy physics experiments, and some type of system similar to this will become more and more necessary in order to search for new particles with extremely small cross sections.

## APPENDIX

### CERENKOV RADIATION

Since the Cerenkov counter  $C_B$  was so important to the E623 analysis, the purpose of this appendix is to summarize some of the properties of Cerenkov radiation and threshold Cerenkov counters and to give the derivation of the weighting formula used by the particle identification algorithm.

Cerenkov radiation will be emitted when a particle of mass  $m$  travels through a transparent medium having index of refraction  $n$ , with a velocity  $v$ , greater than the speed of light in that medium, that is when  $v > c/n$ . The radiation will be emitted at an angle  $\theta_c$  relative to the particle direction, where  $\cos\theta_c = 1/\beta n$  and  $\beta = v/c$ . Figure A.1 shows the Huygens construction for determining the angle of the emitted radiation [Sem 72].

In a threshold Cerenkov counter, any particle of mass  $m$  having a momentum greater than the threshold momentum for that mass will emit radiation and that radiation is usually detected by means of mirrors and photomultiplier tubes. The threshold for emission of radiation will occur when  $\theta_c = 0$  which means that

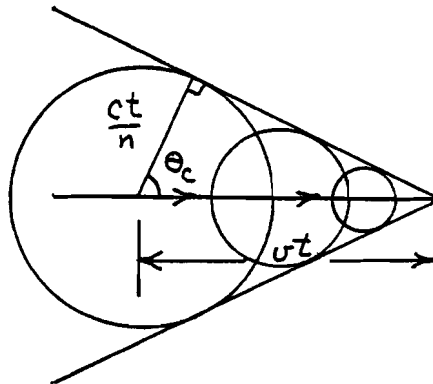


Fig. A.1 - Huygens construction of angle of Cerenkov radiation  $\theta_c$ .

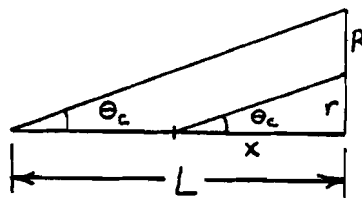


Fig. A.2 - Construction for determining distribution of photons in Cerenkov cone.

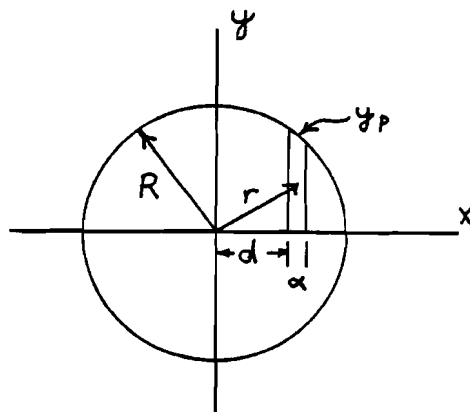


Fig. A.3 - Construction for determining the weight of a strip of width,  $a$ , in a Cerenkov cone.



$$\cos\theta_c = 1$$

and

$$\beta_t = 1/n.$$

Since

$$p = mc\beta\gamma$$

and

$$\gamma = 1/(1 - \beta^2)^{0.5}$$

we have

$$p_{\text{thresh}} = mc\beta_t\gamma_t$$

so that

$$p_{\text{thresh}} = mc/(n^2 - 1)^{0.5}.$$

The number of photons emitted by a particle in a Cerenkov counter is also a function of the particle velocity. From the LBL Particle Properties Data Booklet [Woh 84] we find that

$$N = \# \text{ of photons/cm of radiator} \approx 500\sin^2\theta_c$$

where

$$\sin^2\theta_c = 1 - \cos^2\theta_c = 1 - 1/(\beta n)^2.$$

The maximum number,  $N_{\text{max}}$ , will be given by

$$N_{\text{max}} = 500(n^2 - 1)/n^2$$

and we can then express

$$N = N_{\text{max}}[1 - (1/(n^2-1)\beta^2\gamma^2)]$$

and using the expressions for  $p$  and  $p_{\text{thresh}}$  we have

$$N = N_{\text{max}}[1 - (p_{\text{thresh}}/p)^2].$$

If the Cerenkov counter has a finite length  $L$ ,

then the photons emitted by the particle will be contained inside a cone having a base of radius  $R$ , where  $R/L = \tan\theta_c$  (Figure A.2). The base of this cone usually corresponds to a mirror surface for a multicell threshold Cerenkov counter and we are interested in the distribution of photons on this surface.

If we let  $f(x)dx$  be the probability of emitting a photon between  $x$  and  $x+dx$  at angle  $\theta_c$  with respect to the  $x$ -axis and assume that this probability is uniform along the axis then

$$f(x)dx = \frac{\langle N_{\text{phot}} \rangle}{L} dx$$

so that

$$\int_0^L f(x)dx = \langle N_{\text{phot}} \rangle .$$

From Figure A.2 we see that  $x=r/\tan\theta_c$  and the probability of finding a photon at a distance between  $r$  and  $r+dr$  from the axis (assuming azimuthal symmetry) is given by

$$2\pi r g(r) dr = f(x) dx$$

so that

$$g(r) = \frac{\langle N_{\text{phot}} \rangle}{2\pi r L \tan\theta_c}$$

and the distribution goes as  $1/r$ .

Now that we have the  $1/r$  distribution for the photons in the circle, we can calculate the weight for a small strip inside the circle. This weight is required

by the particle identification algorithm in order to associate the photons in a particular mirror with the corresponding track or tracks, since there may be circles overlapping adjacent mirrors or more than one track through a mirror.

Figure A.3 shows the construction used to calculate the weight for a small strip of width  $a$ . For  $a$  sufficiently small,  $y$  will be approximately constant and equal to  $y_p$  so that

$$W = \int_d^{d+a} dx \int_0^y \frac{1}{\sqrt{x^2+y^2}} dy \approx \int_d^{d+a} \sinh^{-1}(y_p/x) dx .$$

Using the substitution  $u=y_p/x$

$$W = -y_p \int_{u(d)}^{u(d+a)} \frac{\sinh^{-1}(u)}{u^2} du \approx F(y_p, x) \Big|_d^{d+a}$$

where

$$F(y, x) = [x \ln(y/x + \sqrt{(y/x)^2 + 1}) + x \ln(1 + \sqrt{y/x + x/y})] .$$

Then we find that any narrow strip of width  $a$  and height  $y_p - y_m$  will have a weight

$$W = [F(y_p, d+a) - F(y_p, d)] - [F(y_m, d+a) - F(y_m, d)] .$$

## REFERENCES

- [Afe 80a] Y. Afek et al., Nucl. Phys. B165, 339 (1980).
- [Afe 80b] Y. Afek et al., Phys. Rev. D22, 86 (1980).
- [Aub 74] J. J. Aubert et al., Phys. Rev. Lett. 33, 1404 (1974).
- [Aug 74] J. E. Augustin et al., Phys. Rev. Lett. 33, 1406 (1974).
- [Bai 83] R. Bailey et al., NIKHEF preprint-H/83-14, Amsterdam, 1983.
- [Bal 84] R. M. Baltrusaitis et al., Phys. Rev. Lett. 52, 2126 (1984).
- [Bar 64] V. E. Barnes et al., Phys. Rev. Lett. 12, 204 (1964).
- [Boo 84] P. S. L. Booth et al., Nucl. Phys. B242, 51 (1984).
- [Bou 76] M. Bourquin and J. M. Gaillard, Nucl. Phys. B114, 334 (1976).
- [Bjo 64] J. D. Bjorken and S. L. Glashow, Phys. Lett. 11, 255 (1964).
- [Bro 73] S. Brodsky and G. Farrar, Phys. Rev. Lett. 31, 1153 (1973).
- [Cha 78] N. P. Chang and C. T. Nelson, Phys. Rev. Lett. 40, 1617 (1978).
- [Dau 81] C. Daum et al., Phys. Lett. 104B, 246 (1981).
- [Duk 84] D. W. Duke and J. F. Owens, Phys. Rev. D30, 49 (1984).
- [Ein 75] M. E. Einhorn and S. D. Ellis, Phys. Rev. D12, 2007 (1975).
- [Etk 82] A. Etkin et al., Phys. Rev. Lett. 49, 1620 (1982).

- [Fen 82] H. Fenker et al., Fermilab-Pub-82/62-Exp, 1982 (unpublished).
- [Fri 73] H. Fritzsch, M. Gell-Mann and H. Leutwyler, Phys. Lett. 47B, 365 (1973).
- [Gai 75] M. K. Gaillard, B. W. Lee and J. L. Rosner, Rev. Mod. Phys. 47, 277 (1975).
- [Gel 61] M. Gell-Mann, Cal. Tech. Report CTSL-20 (1961).
- [Gel 64a] M. Gell-Mann and Y. Ne'eman, The Eightfold Way, Benjamin, N.Y. (1964).
- [Gel 64b] M. Gell-Mann, Phys. Lett. 8, 214 (1964).
- [Gla 70] S. L. Glashow, J. Iliopoulos and L. Maiani, Phys. Rev. D2, 1285 (1970).
- [Gom 84] H. Gomm, Phys. Rev. D30, 1120 (1984).
- [Gre 81] D. R. Green, Fermilab-Pub-81/81-Exp, 1981 (unpublished).
- [Gre 64] O. W. Greenberg, Phys. Rev. Lett. 13, 1343 (1964).
- [Her 77] S. W. Herb et al., Phys. Rev. Lett. 39, 252 (1977).
- [Iiz 66] J. Iizuka, Prog. Theoret. Phys. Suppl. 37-38, 21 (1966).
- [Jaf 76] R. L. Jaffe and K. Johnson, Phys. Lett. 60B, 201 (1976).
- [Jaf 77] R. L. Jaffe, Phys. Rev. D15, 281 (1977).
- [Jon 82] R. T. Jongerius, Ph.D. thesis, Univ. of Amsterdam, 1982 (unpublished).
- [Li 83] B. Li and K. Liu, Phys. Rev. D28, 1636 (1983).
- [Lin 83] S. J. Lindenbaum, BNL report 34592, 1983.
- [Lip 77a] H. Lipkin, Proceedings of the Fifth International Conference on Experimental Spectroscopy, Northeastern University, Boston (1977).

- [Lip 77b] H. Lipkin, Fermilab-Conf-77/93-THY (1977).
- [Lip 83] H. Lipkin, Phys. Lett. 124B, 509 (1983).
- [May 49] M. G. Mayer, Phys. Rev. 75, 1969 (1949).
- [Nam 66] Y. Nambu, in Preludes in Theoretical Physics in Honor of V. F. Weisskopf, Wiley, N.Y. 1966, p. 133.
- [Nee 61] Y. Ne'eman, Nucl. Phys. 26, 222 (1961).
- [Oku 63] S. Okubo, Phys. Lett. 5, 165 (1963).
- [Owe 84] J. F. Owens, Phys. Rev. D30, 943 (1984).
- [Qui 83] C. Quigg, Gauge Theories of the Strong, Weak and Electromagnetic Interactions, Benjamin, N.Y. (1983).
- [Rob 77] D. Robson, Nucl. Phys. B130, 328 (1977).
- [Sha 84] S. R. Sharpe, Harvard Univ. preprint HUTP-84/A029, 1984.
- [Sjo 83] T. Sjostrand, Computer Phys. Comm. 27, 243 (1983).
- [Yam 81] T. Yamanouchi et al., Phys. Rev. D23, 1514 (1981).
- [Yan 54] C. N. Yang and R. L. Mills, Phys. Rev. 96, 191 (1954).
- [Zwe 64] G. Zweig, CERN preprint 8409/Th. 412, 1964 (unpublished).